THE UNIVERSITY OF QUEENSLAND
AUSTRALIA

A Computational Approach to Evaluation of Nanoporous Zeolitic Membranes for Reverse Osmosis Desalination

Kuk Nam Han
BE, MSc

A thesis submitted for the degree of Doctor of Philosophy at

The University of Queensland in 2016

School of Chemical Engineering

Abstract

Water scarcity has become one of the major global concerns. Research has shown that more than one-third of the population throughout the world resides in water-stressed regions now. Reverse osmosis (RO) desalination has recently been highlighted as a clean technology that is less energy intensive using membranes rather than directly consuming fossil fuels.

Advances in nanomaterials have opened new possibilities for RO membrane materials. Zeolites are one of the candidate materials due to their crystalline structures and durability. However, the performance of zeolite membranes has not been successful for practical use due to poor water flux. Thus, we used molecular dynamics simulations to investigate, at the molecular level, a series of potential zeolite types which have been rarely studied for application in desalination. We determine diffusion coefficients and the structure of water when it passes through pores of these zeolites. In addition, we examine the potential of mean force for water or ions as they move into and through a zeolite membrane in order to evaluate how favourable the passage of the molecule of interest through each membrane is. This provided us with some criteria (i.e. water permeability and ion selectivity) to judge if the membrane is likely to have suitable desalination performance. Without this molecular-level understanding, selection of zeolite materials for desalination membranes is difficult.

Some widely-studied types and potential types of zeolites were selected for our study. The common types have all 3-dimensional (3-D) pore structures, while the potential zeolites have 1-dimensional (1-D) cylindrical pores. To investigate the water dynamics and structure in these different pores, we employed molecular (MD) dynamics simulations. The MD results showed the water self-diffusivity, which indicates a molecular mobility, in the 1-D pores is up to 18-time higher than that of the 3-D pores. As it was found that water molecules formed clusters, water droplets, and moved collectively at low water density in the zeolite pores, the water collective diffusivity, which is directly related to water flux, was also measured for the all the case of zeolites. This collective diffusivity through the 1-D pore zeolites was around one order of magnitude higher than that of the 3-D pore zeolites, suggesting our 1-D zeolites selected are promising as high flux membranes.

To evaluate the thermodynamic stability for water or ion of interest when they pass across the zeolite membranes, the potential of mean force calculations were carried out using MD simulations. We selected one of the 3-D pore zeolites (LTA) and another of the 1-D pore zeolites (VET) for the membrane. In general, these membranes had a moderate energy barrier to water transport, but a very high barrier to sodium or chloride ion transport except the VET membrane. The chloride ion had a minimum in the potential of mean force at the pore entrance and a preference for the chloride ion to enter the pore than to enter the bulk solution for the system considered. However, VET has a lower energy barrier to water passage and a comparable high energy barrier to sodium ion transport compared to the LTA membrane. The VET membrane may be feasible as a desalination membrane if there is some chemical modification done on the pore to effectively reject the chloride ion. This issue will be more studied and addressed in our future work.

Declaration by author

This thesis ***is composed of my original work, and contains*** no material previously published or written by another person except where due reference has been made in the text. I have clearly stated the contribution by others to jointly-authored works that I have included in my thesis.

I have clearly stated the contribution of others to my thesis as a whole, including statistical assistance, survey design, data analysis, significant technical procedures, professional editorial advice, and any other original research work used or reported in my thesis. The content of my thesis is the result of work I have carried out since the commencement of my research higher degree candidature and does not include a substantial part of work that has been submitted ***to qualify for the award of any*** other degree or diploma in any university or other tertiary institution. I have clearly stated which parts of my thesis, if any, have been submitted to qualify for another award.

I acknowledge that an electronic copy of my thesis must be lodged with the University Library and, subject to the policy and procedures of The University of Queensland, the thesis be made available for research and study in accordance with the Copyright Act 1968 unless a period of embargo has been approved by the Dean of the Graduate School.

I acknowledge that copyright of all material contained in my thesis resides with the copyright holder(s) of that material. Where appropriate I have obtained copyright permission from the copyright holder to reproduce material in this thesis.

Publications during candidature

- Peer-reviewed papers

Han, K. N., Bernardi, S., Wang, L. and Searles, D. J., *Water diffusion in zeolite membranes: Molecular dynamics studies on effects of water loading and thermostat*. J. Membr. Sci., 2015. 495: p.322-333.

Han, K. N., Bernardi, S., Wang, L. and Searles, D. J., *Water structure and transport in zeolites with pores in one or three dimensions from molecular dynamics simulations*. J. Phys. Chem. C, 2017. 121: p.381-391.

- Conference abstracts

Han, K. N., *A computational approach to new zeolitic materials for use as reverse osmosis membranes*. 2013 The University of Queensland Engineering Postgraduate Conference, 2013.

Han, K. N., Bernardi, S., Wang, L. and Searles, D. J., *Molecular dynamics approaches to zeolitic membranes for use as a RO desalination*. ACMM23 & ICONN2014, 2014.

Han, K. N., Bernardi, S., Wang, L. and Searles, D. J., *Water diffusion in zeolites with 1-D and 3-D pores for application as desalination membranes*. 2nd International Conference on Desalination using Membrane Technology, 2015.

Han, K. N., Bernardi, S., Wang, L. and Searles, D. J., *Water diffusion in zeolites with 1-D and 3-D pores for application as desalination membranes*. International Conference for Young Chemists 2015, 2015.

Publications included in this thesis

Han, K. N., Bernardi, S., WANG, L. and Searles, D. J., *Water diffusion in zeolite membranes: Molecular dynamics studies on effects of water loading and thermostat*. J. Membr. Sci., 2015. 495: p.322-333 – incorporated as Chapter 4.

Contributor	Statement of contribution
Author **Kuk Nam Han (Candidate)**	Designed simulations (30%) Analysed data (40%) Prepared figures (100%) Wrote the paper (100%) Edited the paper (50%)
Author **Stefano Bernardi**	Designed simulations (30%) Analysed data (20%) Reviewed the paper (20%)
Author **Lianzhou Wang**	Designed simulations (20%) Analysed data (10%) Reviewed the paper (40%) Edited the paper (25%)
Author **Debra J. Bernhardt (Searles)**	Designed simulations (20%) Analysed data (30%) Reviewed the paper (40%) Edited the paper (25%)

Han, K. N., Bernardi, S., Wang, L. and Searles, D. J., *Water structure and transport in zeolites with pores in one or three dimensions from molecular dynamics simulations*. J. Phys. Chem. C, 2017. 121: p.381-391 – incorporated as Chapter 5.

Contributor	Statement of contribution
Author **Kuk Nam Han (Candidate)**	Designed simulations (30%) Analysed data (40%) Prepared figures (100%) Wrote the paper (100%) Edited the paper (50%)
Author **Stefano Bernardi**	Designed simulations (30%) Analysed data (20%) Reviewed the paper (20%)
Author **Lianzhou Wang**	Designed simulations (20%) Analysed data (10%) Reviewed the paper (40%) Edited the paper (25%)
Author **Debra J. Bernhardt (Searles)**	Designed simulations (20%) Analysed data (30%) Reviewed the paper (40%) Edited the paper (25%)

Contributions by others to the thesis

No contributions by others, except as stated in “Publications included in this thesis” on page v.

Statement of parts of the thesis submitted to qualify for the award of another degree

None.

Acknowledgements

Prima facea, I am grateful to the heavenly Father for the good health and wellbeing that were necessary to complete this thesis. I wish to express my sincere thanks to my supervisors, Prof. Debra Bernhardt of Centre for Theoretical and Computational Molecular Science in Australian Institute for Bioengineering and Nanotechnology and Prof. Lianzhou Wang of School of Chemical Engineering for their continuous support of my PhD study, and for their patience, motivation, immense knowledge as well as financial support.

I am very thankful to the UQ and National Centre of Excellence in Desalination Australia for my UQI tuition & living allowance and Top-up scholarships which enabled me to survive in this harsh PhD life.

Beside my advisors, I would like to thank Stefano and James for their insightful comments and encouragement, but also for the hard questions which stimulated me to widen my research from various perspectives. I also express my warm and sincere thanks to my fellow co-workers, Meli, Marsel and Tanveer for the warm greetings every morning, and thank Stephanie for the wonderful admin support. And Marlies, the computing time dictator, I would like to express my genuine thanks to her for the unconditional support without asking reasons.

I am also grateful to my hilarious mate, Kukso (Guozhao) for sharing never-ending episodes and entertaining materials. I am thankful for Inhi's aspiring guidance, invaluably constructive criticism and friendly advice during my PhD.

It would be never enough to say thank you to my true friends, Taegyu, Jongmin and Woncheol, who have been an emotional support through the coffee time. I am sincerely thankful to them for walking together beside me in the PhD journey.

Last but not the least, I must express my very profound gratitude to my parents, the in-laws and to my dear wife for providing me with unfailing support and continuous encouragement throughout my years of study and through the process of researching and writing this thesis. Also, my lovely Kai for the smiles and the joy you have brought me during this tough period. This accomplishment would not have been possible without them.

I also place on record, my sense of gratitude to one and all, who directly or indirectly, have lent me their hand in this venture.

Keywords

zeolite, desalination membrane, molecular dynamics simulation, water transport, ion transport, nanopore, water behaviour.

Australian and New Zealand Standard Research Classifications (ANZSRC)

ANZSRC code: 090404, Membrane and Separation Technologies, 40%

ANZSRC code: 100708, Nanomaterials, 30%

ANZSRC code: 030704, Statistical Mechanics in Chemistry, 30%

Fields of Research (FoR) Classification

FoR code: 0904, Chemical Engineering, 40%

FoR code: 1007, Nanotechnology, 30%

FoR code: 0307, Theoretical and Computational Chemistry, 30%

Table of Contents

List of Figures

List of Tables

List of Abbreviations

1-D	One dimensional
2-D	Two dimensional
3-D	Three dimensional
AFI	AFI-type zeolite
CA	Cellulose acetate
CFI	CFI-type zeolite
CNT	Carbon nanotube
Com	centre-of-mass
DPD	Dissipative particle dynamics
ED	Electrodialysis
FAU	FAU-type zeolite
FEP	Free energy perturbation
FO	Forward osmosis
GCMC	Grand canonical Monte Carlo
GON	GON-type zeolite
LB	Lorentz-Berthelot
LGV	Langevin
LJ	Lennard-Jones
LTA	LTA-type zeolite
MD	Molecular dynamics
MED	Multi-effect distillation
MFI	MFI-type zeolite
MPD	*m*-phenylenediamine
MSD	Mean square displacement
MSF	Multi-stage flash
MTF	MTF-type zeolite
NH	Nosé-Hoover
NPH	Constant pressure and enthalpy ensemble
NPT	Constant pressure and temperature ensemble

NVE	Microcanonical ensemble
NVT	Constant volume and temperature ensemble
PA	Polyamide
PBC	Periodic boundary conditions
PFG NMR	Pulsed field gradient nuclear magnetic resonance
PMF	Potential of mean force
PPPM	Particle-Particle-Particle mesh
QENS	Quasi-elastic neutron scattering
RDF	Radical distribution function
RO	Reverse osmosis
SAXS	Small-angle x-ray scattering
SFF	SFF-type zeolite
TFC	Thin film composite
TI	Thermodynamic integration
TMC	Trimesoyl chloride
TON	TON-type zeolite
VET	VET-type zeolite
XRD	X-ray diffraction

Chapter 1 Introduction

1.1 Background

With intensive industrialisation and climate change, water scarcity has become one of the major global concerns. Research has shown that more than one-third of the population throughout the world resides in water-stressed regions and this is expected to increase to two-thirds by 2025 (Li et al., 2013, Elimelech and Phillip, 2011). Supplying drinking water in a clean and safe way is currently a primary challenge to address. The desalination process has substantial potential to provide new fresh water from non-conventional resources such as seawater, which accounts for over 97% of the total water. Although desalination by thermal process, such as distillation, is still popular in areas with plentiful energy sources, reverse osmosis (RO) desalination has now been highlighted as a clean technology by using membranes rather than consuming fossil fuels directly (Charcosset, 2009, Eshoul et al., 2015, Shenvi et al., 2015).

RO techniques require a membrane that water permeates into and passes through at high pressure, but the salt ions of seawater are not allowed to enter due mainly to size exclusion effects. Ideally, the best membrane for desalination has a combination of high salt ion rejection and high water flow rate. But it is rare for high rejection performance and rapid water flow to both be achieved on membranes, since the reduced molecular sieving effect of a larger pore membrane normally leads to lower rejection, despite the higher water flux. For example, a polyamide composite membrane that is widely used for desalination exhibits distinct trade-off correlations between permeability and rejection characters (Geise et al., 2011, Raval et al., 2015). Thus, the most significant challenge in this field is to develop higher flux membranes while retaining their rejection properties.

Recently, advances in nanomaterial synthesis have opened new possibilities for membrane materials. Nano-crystalline materials, particularly carbon nanotubes (CNTs), demonstrate exceptional water transport due to its well-defined one-dimensional channels which give rise to almost ‘frictionless’ flow (Cohen-Tanugi and Grossman, 2012, Thomas and Corry, 2016). This 1-D path allows the water to be driven with low friction as the water molecules are surrounded by hydrophobic channel walls (Majumder et al., 2005, Holt et al., 2006). However, use of CNT membranes has problems such as low salt rejection due to the challenges of creating well-packed and well-aligned channels with suitable desalting pores. Nanoporous graphenes have also been investigated computationally for desalination purposes, showing a high potential for greatly improved water permeability that could arise from the ultrathin graphene layer, while keeping high mechanical strength (Cohen-Tanugi and Grossman, 2012, Surwade et al., 2015). Despite these promising properties, there are key technical challenges to make a high density of uniform nanopores on the ultrathin layer for application to a desalination membrane.

Other nanoporous materials, zeolites, have attracted great interest as alternative materials for desalination membranes (Li and Wang, 2010, Drobek et al., 2012, Rodríguez-Calvo et al., 2014). They have crystalline structures that can be relatively simply fabricated in many different ways. Also, these materials can be applied in many practically useful forms such as substrates, nanoparticles, or thin-films (Gascon et al., 2012, Rodríguez-Calvo et al., 2014). Since zeolites have a lot of different framework types which describe the network of tetrahedrally-coordinated atoms of a zeolite molecule, they are classified as three-capital-letter codes. This is so-called Framework Type Code that is derived from the common name of the zeolite materials. The widely-used types of zeolites for membranes are ZSM-5 zeolite (ZS**Mfi**ve, MFI-type) and zeolite A (**L**inde **T**ype **A**, LTA-type) which have been intensively studied for desalination (Murad et al., 1993, Li et al., 2004b, Li et al., 2008, Li et al., 2004a, Li et al., 2007, Lin and Murad, 2001, Liu et al., 2008, Malekpour et al., 2008, Kumakiri et al., 2000, Duke et al., 2009, Gopalakrishnan et al., 2006, Drobek et al., 2012, Cho et al., 2011, Liu and Chen, 2013). Their desalinating capability and well-defined channels have attracted considerable interest in industrial applications. To date, however, only partial success has been achieved for practical use due to poor water permeability. Therefore, zeolites which have cylindrical sub-nanometre 1-D pore channels are proposed to be useful as high flux desalination membranes along with advantages of their simple fabrication and natural abundance.

To evaluate the suitability of potential zeolite types as desalination membranes, a systematic study for the zeolites must be performed by scrutinising water behaviour depending on their pore sizes and structures. Furthermore, the performance of the zeolite membranes also have to be assessed by measuring how favourable water or ion transport through the membrane is since a desalination membrane allows water to pass through, but effectively block salt ions. To achieve these molecular-level studies, molecular dynamics (MD) simulation are a very appropriate method because this approach enables us to achieve the quantification of water movement and structure through the zeolites and their thermodynamic characterisation.

The aim of this thesis is to investigate water transport in zeolite frameworks that have been widely studied, as well as in unexplored types of zeolite frameworks which have high potential for desalination, using MD simulations. This molecular-level approach will enable us to gain a deep understanding of the water behaviour occurring in both the widely-used and potential zeolites, then allow us to compare and understand the water behaviour in different zeolite types with an aim of assessing whether those are promising or not as membrane materials. In addition, free energy studies will be carried out to examine the thermodynamic stability of water or ion passing through those zeolite membranes. The results of the free energy calculations will give insight into the membrane selectivity by showing how thermodynamically favourable the particle permeation into or through the membranes is. The findings of this thesis is expected to open new possibilities of zeolites as membranes for future desalination.

1.2 Scope and Research Contributions

The study area of this thesis will cover diffusional and structural properties of water in zeolites with potential use for desalination membranes at the molecular scale via MD simulations. The selected zeolites are all siliceous (pure silica) types with different pore structures. The pure silica membranes are expected to have a hydrophobic property of inner pores which may provide frictionless pathway for water transport. The zeolites with three-dimensional (3-D) pore channels are MFI-, LTA-, and FAU-type which have been extensively studied as desalination membrane materials in recent decades. One-dimensional (1-D) pore channel holders are VET-, TON-, and CFI-type zeolites that are potential materials for desalination membranes. For the 1-D zeolites as membranes, there are some issues that have to be achieved such as crystal growth direction since it should be more beneficial when the 1-D channels grow in the direction perpendicular to membrane surfaces. Few studies have recently attempted tuneable zeolite structures such as crystal direction, thickness, and morphology, then they have partly succeeded and continue to develop. It is thus worthwhile to conduct fundamental studies on those unexplored 1-D zeolites as well as the widely-studied 3-D zeolites for future references to desalination membranes.

We employ molecular dynamics simulations for our molecular-level studies. Some important points to be considered in these MD studies are that there are a number of ensemble algorithms being used to integrate equations of motion of particles in a molecular system. Previous studies have reported that different algorithms may result in different dynamical properties of particles (Krishnan et al., 2013, Bernardi et al., 2010, Yong and Zhang, 2013, Thomas and Corry, 2014), thus validation work on the selected ensemble has to be done to produce reliable results for water transport. The first work of this thesis will deal with studies of different thermostatting (temperature controller) ensembles on diffusional and structural behaviour of the water in zeolites. The second work is to study the widely-used 3-D pore zeolites and the potential 1-D pore zeolites for evaluating their water fluxes to be when these zeolites are built as membranes. The third work gives an intuitive idea of the stability of water or ion transport across the zeolite membranes using the PMF calculations.

The follows are the major tasks to be undertaken in this thesis.

- Discover the effects of various MD ensembles on dynamical and structural behaviour of water in zeolites; when NVE (microcanonical), NVT (canonical), NVT to zeolite framework only, NVT to water only, NPT, or NPH ensemble is applied individually to a system, it will be studied how they vary the diffusivity and the distribution pattern of water.
- Investigate the clustering of water in zeolite pores and its effect on diffusion rates and structures of the confined water.
- Explore water behaviour depending on the shape and diameter of 1-D pores of zeolites (i.e. VET, TON, CFI); the relation of the pore shape (circular: VET and CFI, elliptical: TON) and diameter (TON < VET < CFI) to water diffusivity and distributional structure will be evaluated.
- Understand effects of the pore shape, size, and dimensionality on water behaviour in 3-D pore zeolites; it will be explored how the pore shape (cage-like: LTA and FAU, cylindrical: MFI), diameter (MFI < LTA < FAU), and how pore alignment make varied outcomes.
- Generate the free energy profiles of water or ion transport across the zeolite membranes; the difference of the energy barrier between water, sodium and chloride ion permeation into a membrane will be demonstrated.

1.3 Sections of Thesis

The thesis consists of seven chapters.

Chapter 1 covers the motivation and introduction of my PhD project, scope of the study and the contributions made to the research area.

Chapter 2 shows a literature review on a variety of reverse osmosis (RO) desalination membrane materials, and more focuses on the previous work on zeolite desalination membranes.

Chapter 3 introduces a brief principle of molecular dynamics simulation and how it works for the membrane science, also the previous MD studies on zeolites as RO membranes.

Chapter 4 presents a comprehensive study on transport properties and structures of water in zeolites.

Chapter 5 is a comparison study of water behaviour in the widely-studied 3-D zeolites and the potential 1-D zeolites. This chapter evaluates potentials of the zeolites as desalination membranes in terms of water flux.

Chapter 6 ranges over the free energy changes of water, sodium and chloride transport across the zeolite membranes by measuring the potential of mean force (PMF). The outcomes will give a guidance to judge those zeolite membranes for desalination.

Chapter 7 is a summary section for this thesis and suggests future research directions in zeolite RO desalination membranes.

References

BERNARDI, S., TODD, B. D. & SEARLES, D. J. 2010. Thermostating highly confined fluids. *The Journal of Chemical Physics,* 132**,** 244706.

CHARCOSSET, C. 2009. A review of membrane processes and renewable energies for desalination. *Desalination,* 245**,** 214-231.

CHO, C. H., OH, K. Y., KIM, S. K., YEO, J. G. & SHARMA, P. 2011. Pervaporative seawater desalination using NaA zeolite membrane: Mechanisms of high water flux and high salt rejection. *Journal of Membrane Science,* 371**,** 226-238.

COHEN-TANUGI, D. & GROSSMAN, J. C. 2012. Water Desalination across Nanoporous Graphene. *Nano Letters,* 12**,** 3602-3608.

DROBEK, M., YACOU, C., MOTUZAS, J., JULBE, A., DING, L. & DINIZ DA COSTA, J. C. 2012. Long term pervaporation desalination of tubular MFI zeolite membranes. *Journal of Membrane Science,* 415–416**,** 816-823.

DUKE, M. C., O'BRIEN-ABRAHAM, J., MILNE, N., ZHU, B., LIN, J. Y. S. & DA COSTA, J. C. D. 2009. Seawater desalination performance of MFI type membranes made by secondary growth. *Separation and Purification Technology,* 68**,** 343-350.

ELIMELECH, M. & PHILLIP, W. A. 2011. The Future of Seawater Desalination: Energy, Technology, and the Environment. *Science,* 333**,** 712-717.

ESHOUL, N. M., AGNEW, B., AL-WESHAHI, M. A. & ATAB, M. S. 2015. Exergy Analysis of a Two-Pass Reverse Osmosis (RO) Desalination Unit with and without an Energy Recovery Turbine (ERT) and Pressure Exchanger (PX). *Energies,* 8**,** 6910-6925.

GASCON, J., KAPTEIJN, F., ZORNOZA, B., SEBASTIAN, V., CASADO, C. & CORONAS, J. 2012. Practical Approach to Zeolitic Membranes and Coatings: State of the Art, Opportunities, Barriers, and Future Perspectives. *Chemistry of Materials,* 24**,** 2829-2844.

GEISE, G. M., PARK, H. B., SAGLE, A. C., FREEMAN, B. D. & MCGRATH, J. E. 2011. Water permeability and water/salt selectivity tradeoff in polymers for desalination. *Journal of Membrane Science,* 369**,** 130-138.

GOPALAKRISHNAN, S., YAMAGUCHI, T. & NAKAO, S. I. 2006. Permeation properties of templated and template-free ZSM-5 membranes. *Journal of Membrane Science,* 274**,** 102-107.

HOLT, J. K., PARK, H. G., WANG, Y. M., STADERMANN, M., ARTYUKHIN, A. B., GRIGOROPOULOS, C. P., NOY, A. & BAKAJIN, O. 2006. Fast mass transport through sub-2-nanometer carbon nanotubes. *Science,* 312**,** 1034-1037.

KRISHNAN, T. V. S., BABU, J. S. & SATHIAN, S. P. 2013. A molecular dynamics study on the effect of thermostat selection on the physical behavior of water molecules inside single walled carbon nanotubes. *Journal of Molecular Liquids,* 188**,** 42-48.

KUMAKIRI, I., YAMAGUCHI, T. & NAKAO, S. 2000. Application of a zeolite a membrane to reverse osmosis process. *Journal of Chemical Engineering of Japan,* 33**,** 333-336.

LI, C., GOSWAMI, Y. & STEFANAKOS, E. 2013. Solar assisted sea water desalination: A review. *Renewable & Sustainable Energy Reviews,* 19**,** 136-163.

LI, D. & WANG, H. T. 2010. Recent developments in reverse osmosis desalination membranes. *Journal of Materials Chemistry,* 20**,** 4551-4566.

LI, L. X., DONG, J. H. & NENOFF, T. M. 2007. Transport of water and alkali metal ions through MFI zeolite membranes during reverse osmosis. *Separation and Purification Technology,* 53**,** 42-48.

LI, L. X., DONG, J. H., NENOFF, T. M. & LEE, R. 2004a. Desalination by reverse osmosis using MFI zeolite membranes. *Journal of Membrane Science,* 243**,** 401-404.

LI, L. X., DONG, J. H., NENOFF, T. M. & LEE, R. 2004b. Reverse osmosis of ionic aqueous solutions on a MFI zeolite membrane. *Desalination,* 170**,** 309-316.

LI, L. X., LIU, N., MCPHERSON, B. & LEE, R. 2008. Influence of counter ions on the reverse osmosis through MFI zeolite membranes: implications for produced water desalination. *Desalination,* 228**,** 217-225.

LIN, J. & MURAD, S. 2001. A computer simulation study of the separation of aqueous solutions using thin zeolite membranes. *Molecular Physics,* 99**,** 1175-1181.

LIU, N., LI, L. X., MCPHERSON, B. & LEE, R. 2008. Removal of organics from produced water by reverse osmosis using MFI-type zeolite membranes. *Journal of Membrane Science,* 325**,** 357-361.

LIU, Y. & CHEN, X. 2013. High permeability and salt rejection reverse osmosis by a zeolite nano-membrane. *Physical Chemistry Chemical Physics,* 15**,** 6817-6824.

MAJUMDER, M., CHOPRA, N., ANDREWS, R. & HINDS, B. J. 2005. Nanoscale hydrodynamics: Enhanced flow in carbon nanotubes (vol 438, pg 44, 2005). *Nature,* 438**,** 930-930.

MALEKPOUR, A., MILLANI, M. R. & KHEIRKHAH, M. 2008. Synthesis and characterization of a NaA zeolite membrane and its applications for desalination of radioactive solutions. *Desalination,* 225**,** 199-208.

MURAD, S., RAVI, P. & POWLES, J. G. 1993. A computer-simulation study of fluids in model slit, tubular, and cubic micropores. *Journal of Chemical Physics,* 98**,** 9771-9781.

RAVAL, H. D., RANA, P. S. & MAITI, S. 2015. A novel high-flux, thin-film composite reverse osmosis membrane modified by chitosan for advanced water treatment. *RSC Advances,* 5**,** 6687-6694.

RODRÍGUEZ-CALVO, A., SILVA-CASTRO, G. A., OSORIO, F., GONZÁLEZ-LÓPEZ, J. & CALVO, C. 2014. Novel Membrane Materials for Reverse Osmosis Desalination. *Hydrology: Current Research,* 5.

SHENVI, S. S., ISLOOR, A. M. & ISMAIL, A. F. 2015. A review on RO membrane technology: Developments and challenges. *Desalination,* 368**,** 10-26.

SURWADE, S. P., SMIRNOV, S. N., VLASSIOUK, I. V., UNOCIC, R. R., VEITH, G. M., DAI, S. & MAHURIN, S. M. 2015. Water desalination using nanoporous single-layer graphene. *Nat Nano,* 10**,** 459-464.

THOMAS, M. & CORRY, B. 2014. Thermostat choice significantly influences water flow rates in molecular dynamics studies of carbon nanotubes. *Microfluidics and Nanofluidics***,** 1-7.

THOMAS, M. & CORRY, B. 2016. A computational assessment of the permeability and salt rejection of carbon nanotube membranes and their application to water desalination. *Philosophical Transactions of the Royal Society A: Mathematical, Physical and Engineering Sciences,* 374.

YONG, X. & ZHANG, L. T. 2013. Thermostats and thermostat strategies for molecular dynamics simulations of nanofluidics. *The Journal of Chemical Physics,* 138**,** 084503.

Chapter 2 Zeolites as Porous Membranes

This chapter briefly outlines the background, current knowledge, and recent research on reverse osmosis desalination membranes which motivated and initiated the research of this thesis. We discuss the knowledge, limitations, and potentials for membrane materials, focusing on zeolites which are the materials studied in this thesis.

More specific relevant theories, methodologies, and recent studies will be thoroughly reviewed in the next chapter to provide a background to our research on zeolite membranes using molecular dynamics simulations.

2.1 Introduction to reverse osmosis desalination

Desalination is important for the production of clean water from seawater or brackish water, which is required to meet the water demand for food, agricultural, human activities. This process can be carried out in many different ways. Conventional methods include thermal technologies such as multi-stage flash (MSF) and multi-effect distillation (MED) which have been most widely used worldwide, especially in oil-producing countries (Khawaji et al., 2008, Darwish and El-Dessouky, 1996, Humplik et al., 2011, Kesieme et al., 2013). Membrane-based technologies have also been proposed and used recently, including electrodialysis (ED), reverse osmosis (RO), and forward osmosis (FO) (Sadrzadeh and Mohammadi, 2008, McGinnis and Elimelech, 2007, Lee et al., 2011, Li and Wang, 2010, Shenvi et al., 2015). These membrane-based processes are deemed environmentally-friendly due to the less energy intensive operation compared to the thermal processes. Of the membrane processes, RO is regarded as the most promising and leading technology in desalination (Eshoul et al., 2015, Inukai et al., 2015, Shenvi et al., 2015). In osmosis, osmotic pressure is generated by concentration differences between solutions, which draws the solvent from the less concentrated solution (e.g. pure water) through a semi-permeable membrane into the more concentrated solution (e.g. seawater) until both concentrations reach the same level (Figure 2-1). Conversely, in reverse osmosis (RO), external pressure greater than the osmotic pressure is applied to the higher concentration solution so that water goes through a semi-permeable membrane to the fresh water, but salts are rejected by the membrane (Figure 2-1).

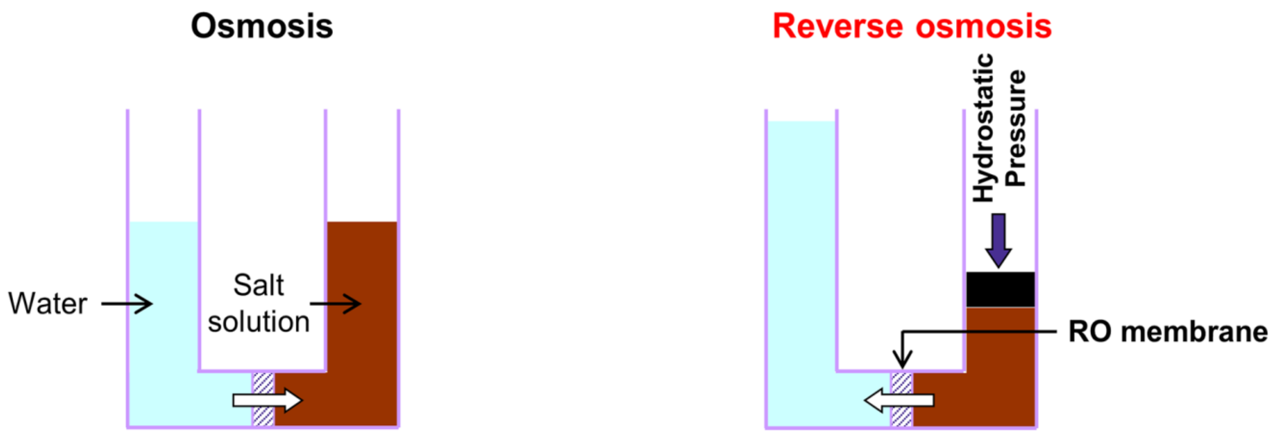

Figure 2-1 Schematic illustrations of osmosis process and reverse osmosis (RO) desalination process.

In the RO process, there are two major features that are required, that is, high water flux and high salt rejection. In general, these two parameters are a trade-off in that an increase in the flux may bring about low salt rejection and vice versa. However, substantial efforts have recently been made to satisfy the commercially-applicable high flux together with high enough salt rejection for drinking-quality water (Humplik et al., 2011, Lee et al., 2011, Giwa et al., 2016, Shenvi et al., 2015). To fulfil this aim, developments in membrane materials should be in the forefront. The membrane used in RO desalination is called a RO desalination membrane or RO membrane.

The first RO membrane was a cellulose acetate (CA)-based membrane. CA monomer is the basic repeating unit that can be linked and crosslinked, resulting in fabric matrices that are porous. These cellulosic polymer membranes and their blends with other materials lead to an effective separation performance that can be tuned for the particular application (Basta et al., 2003, El-Saied et al., 2003, Ferjani and Roudesli, 2000, Ferjani et al., 2000, Ferjani et al., 2002). For example, blending with a small fraction of poly(methylhydrosiloxane) was shown to greatly improve salt rejection since it played as a crosslinking agent for CA, but decreased the water transport rate due to the enhanced hydrophobicity (Ferjani et al., 2002, Ferjani et al., 2000, Li and Wang, 2010). However, excessive polymer additives in CA was found to result in deterioration of polymer compatibility, causing poor performance (El-Saied et al., 2003).

One of the most successful membranes for desalination is a polyamide (PA)-derived membrane. Many studies have intensively focused on PA thin film composite (TFC) membranes (Figure 2-2) which consist of; (1) a non-woven fabric, (2) a polysulfone substrate, and (3) a cross-linked PA working layer; due to their high salt rejection and cost effective fabrication. For this membrane, two bottom layers, the fabric and substrate, give mechanical strength to one another as well as the top layer, and the very dense top layer absorbs water and retains salts on application of a pressure gradient (Raval et al., 2015). Most studies of this membrane focus on trying to improve water permeation while keeping the same level of rejection (Ghosh et al., 2008, Ghosh and Hoek, 2009, Freger et al., 2002, Belfer et al., 1998b, Belfer et al., 1998a, Jin and Su, 2009, Kang et al., 2007b, Kim et al., 2000, Kim et al., 2009, Il Kim and Kim, 2006, Li et al., 2008a, Li et al., 2007a, Roh et al., 2006, Saha and Joshi, 2009, Kim et al., 2003). For instance, optimising the PA polymerisation (the key parameter for controlling desalination properties), by tuning of the monomer concentration, changing of the solvent used for the casting solution, and changing the reaction conditions, leads to different surface morphologies and pore densities (Petersen, 1993, Ghosh and Hoek, 2009, Madaeni et al., 2009, Roh et al., 2006, Ghosh et al., 2008). Furthermore, a variety of monomer (amines and acid chlorides) combinations have been studied (Li et al., 2007a, Li et al., 2008a, Kim et al., 2000, Saha and Joshi, 2009, Kim et al., 2003). Thanks to this great deal of effort on membranes, it has been possible to impressively enhance the PA TFCs' water flux while maintaining salt retention. Nevertheless, there are still drawbacks that restrict its practical use. Very dense PA surface layers cause fouling on the surface, which gradually deteriorates membrane performance. Also, chlorine attack on the amide bond in PA membranes breaks the surface PA linkage, which degrades the working layer. Above all, despite the enhanced water permeability, TFC membranes are still limited by poor water flux ($6.6 \times 10^{-6}\ \mathrm{m^3\ m^{-2}\ s^{-1}}$) (Raval et al., 2015).

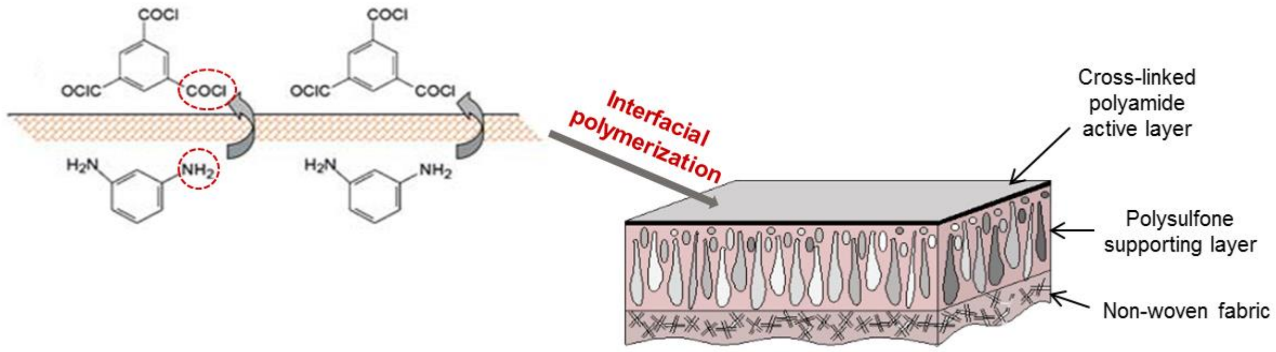

Figure 2-2 A schematic of the interfacially polymerised polyamide (PA) thin film composite membrane. Acid chloride groups from trimesoyl chloride (TMC) monomers and amine groups from m-phenylenediamine (MPD) monomers are highly reactive to one another, generating a dense polyamide polymer. Since TMC tends to be in organic solvent and MPD in water, they can be polymerised at the interface between organic and water phases [Adopted and modified from Ref (Kim et al., 2005)].

2.2 Recent trends in RO desalination membrane materials

Due to the disadvantages mentioned earlier for the commercial TFC membranes, coupled with results of rapid development in crystalline nanomaterials, nanostructured membranes are now also being considered. Recently, ultra-flux nanomaterial membranes have received intensive attention as potential replacements for the TFC membranes. Since it is generally accepted that higher water permeability membranes demand lower pressure for water transport, the desalination energy consumption is consequently reduced. Of the promising candidates, so far carbon nanotube (CNT) membranes have exhibited the greatest promise for future use.

Well-aligned CNT membranes have demonstrated 4 or 5 orders of magnitude higher water flux than the values expected based on hydrodynamic theories (Holt et al., 2006, Majumder et al., 2005, Elimelech and Phillip, 2011, Alexiadis and Kassinos, 2008, Shenvi et al., 2015). This exceptional feature may be attributed to the molecular smoothness of inner tubes where water passes as if the internal walls are lubricated (Corry, 2008, Falk et al., 2010). To prevent salt ions from permeating pores, the entrance of CNTs must be chemically modified to have functional groups that reject ions, or the pore size of nanotubes must be smaller than the ion diameter. However, to date, no successful practical outcomes on CNT have shown comparable salt rejection for desalination to that of conventional TFC membrane (Trivedi and Alameh, 2016, Shenvi et al., 2015). The possible explanation is that it is very challenging to produce well-defined CNTs without defects or to make adequate desalting diameters of the nanotubes. Furthermore, the CNT fabrication cost is much higher than that for the current polymeric membrane.

Another carbonaceous membrane being recently highlighted is nanoporous graphene. Graphene is an atomistic-thick single layer of hexagonally-arranged carbon atoms. This material gained much interest due to its unique electronic characteristics which may be applied for electronic devices (Rodríguez-Calvo et al., 2014, Humplik et al., 2011). It also has a high mechanical strength (Lee et al., 2008) and impermeability to even very small molecules like helium in its pristine form (Bunch et al., 2008). However it has been considered as a high flux membrane if pores are generated in the sheet. Recently, large area graphene layers have been successfully fabricated and transferred in roll-to-roll production (Bae et al., 2010), which opens the possibility of large-scale graphene membrane production. Some molecular dynamics (MD) simulations (Sint et al., 2008, Suk and Aluru, 2010) have been carried out to study water and ion transport through graphene with nanopores. The nanoporous graphene with diameters of ~5 Å studied by Sint *et al.* (Sint et al., 2008) behaved as an ionic sieve with high selectivity and transparency. Suk and Aluru (Suk and Aluru, 2010) examined water transport across a porous graphene membrane and compared it with that of a carbon nanotube

(CNT) membrane of short-length (<10 nm). For the pore size of ca. 7.5 Å in diameter, water flux was higher for the CNT membrane than the single-layer nanoporous graphene, but for the bigger pores (ca. 27.5 Å), the graphene membrane showed the higher flux. These theoretical results indicate the feasibility of high flux desalination membranes using nanoporous graphene. Very recently, nanoporous single-layer graphene has been experimentally developed as a desalination membrane by Surwade *et al.* (Surwade et al., 2015), showing exceptional results of nearly 100% salt rejection and high water volume flux of up to 1 m^3 m^{-2} s^{-1} that is five orders of magnitude higher than the commercial polymeric membrane. However, it is very challenging to create sub-nanometer pores uniformly on the sheet. Also, a high density of pores can deteriorate the mechanical strength of the membrane (Surwade et al., 2015) and the cost of porous graphene fabrication is very high owing to the need to use expensive perforating methods such as oxygen plasma etching (Surwade et al., 2015), electron beam irradiation (Fischbein and Drndić, 2008), and ion bombardment (Lucchese et al., 2010, Ahlberg et al., 2016). Therefore, the commercialisation of this thin-layer membrane is still far from realisation.

Another material that has been extensively considered as a membrane over the last decade is zeolite. Zeolites are three-dimensional nanostructures with a great variety of classes in terms of structure and elemental composition. According to the compositional elements, zeolites can be categorised, and common categories include silicas, aluminosilicates, and aluminophosphates (Kitao et al., 1999, Humplik et al., 2011, Filippov et al., 2012). In addition, to specify the structure of zeolites, three-letter codes have been widely used for identification of zeolites. Around 200 different structures have been identified to date (First et al., 2011, Baerlocher and McCusker, 2015). The identifying codes will be often referred to in the rest of the thesis.

Due to their chemical and physical varieties, zeolites have been extensively studied for use as pervaporation and gas separation membranes. Also, their well-defined crystallinity and different chemical functionalities provide great potential for use in areas that range from biophysics to materials science (Ceyhan et al., 2007, Jiang et al., 2011, Gascon et al., 2012). Moreover, they can be chemically, thermally, and mechanically stronger than some polymeric membranes used for desalination. Murad et al. were first to report on potential use of zeolite membranes for ion removal from water using a computational approach (Murad and Powles, 1993, Lin and Murad, 2001, Murad et al., 1993, Murad, 1996). According to their simulations, the membranes made of ZK-4 (LTA-type) or pure silica LTA (Leiggener et al., 2008, Rigo et al., 2013) exhibited a perfect sodium rejection in RO process. However, very few experimental attempts on zeolitic RO membranes were done until 2004, and only a few types of zeolite (Figure 2-3) have received attention. This has been due to the higher fluxes and selectivity that have been obtained compared to those in commercial TFC membranes (Drobek et al., 2012, Lee et al., 2011).

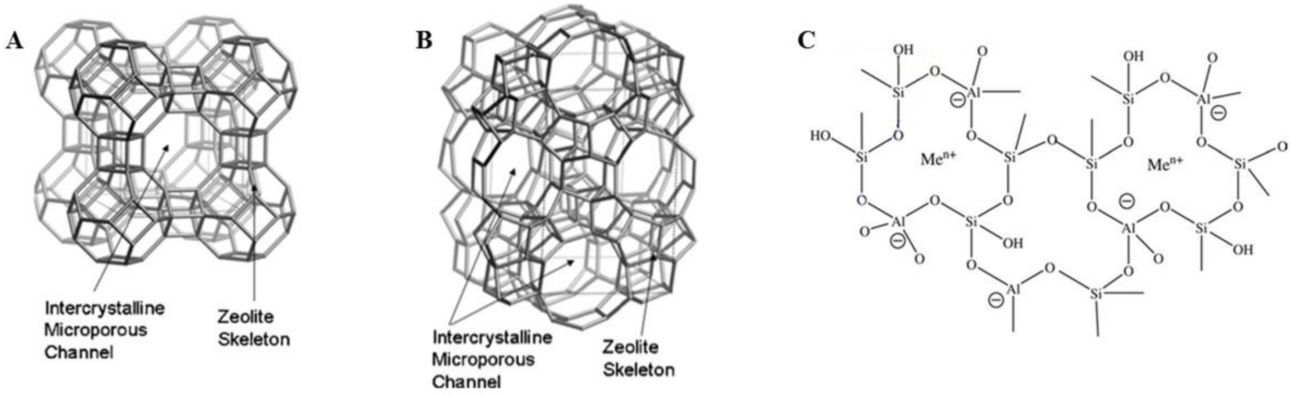

Figure 2-3 Three-dimensional representations of (A) LTA zeolite with pores of 0.4 nm diameter and (B) MFI zeolite with 0.56 nm pores [Reproduced from Ref (Lee et al., 2011)]. (C) Two-dimensional drawing of aluminosilicate zeolite [Reproduced from Ref (Granda-Valdés et al., 2006)].

2.3 Zeolites as desalination membrane materials

Zeolite membranes (Figure 2-4) are typically fabricated by the hydrothermal method and deposited onto porous steel or ceramic substrates (Li et al., 2004a, Malekpour et al., 2008, Liu et al., 2008, Li et al., 2004b, Li et al., 2007b, Li et al., 2008b). The thickness of membranes needs to be in the micro-meter scale to maintain high selectivity and enough permeance for practical use. The reports on zeolite A (Si:Al = 1:1, LTA-type) application for desalination suggested a good resistance of the zeolite layer to high pressure and solution concentration (Kumakiri et al., 2000). MFI-type zeolites have attracted even more attention for desalination purposes (Li et al., 2004a, Duke et al., 2009, Li et al., 2007b, Li et al., 2004b, Li et al., 2008b, Liu et al., 2008).

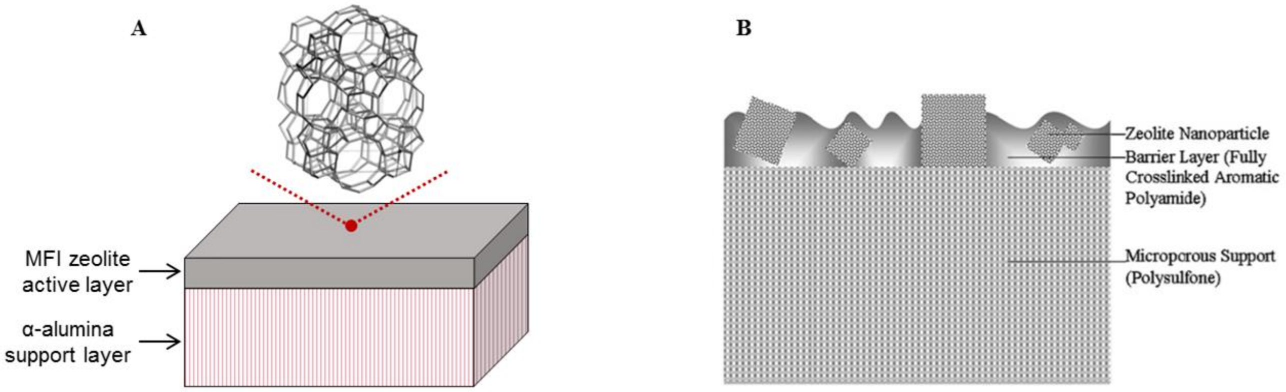

Figure 2-4 Schematic drawings of (A) MFI zeolite membrane (B) Type A zeolite-embedded membrane [Adopted and modified from Ref (Jeong et al., 2007, Lee et al., 2011)].

MFI zeolites possess straight channels and zigzag channels linked to one another, producing 3-D channels with 0.55 nm-sized pores suitable for hydrated ion removal (Kazemimoghadam, 2010). Some studies into MFI membranes proved that enhancing ion selectivity reduces water permeability with increasing RO operation time. It is generally believed that some sodium ions permeate the pores and hinder water molecules from entering, thereby reducing the water flux. Thus, overlapping of the crystalline zeolitic layers has been used to prevent ion permeation. Such membranes operated under RO system for hours showed that the Na^+ rejection varies from 76.7% to 99.4% (Li et al., 2004a, Liu et al., 2008). Compared to the conventional PA membrane which has >98% sodium rejection (Kang et al., 2007a, Li and Wang, 2010), the zeolite desalination membrane still has not reached the commercial standard. The lower rejection than the theoretical prediction of 100% may be attributed to non-selective inter-crystal pores where a small quantity of ions could pass through during RO process.

As in the case of the polymeric membranes, RO desalination properties of zeolite membranes are dependent on the applied pressure, temperature, feed concentration as well as pore size (Li et al., 2008b, Li et al., 2007b). The variation in such conditions influences the ion flux more than the water flux which mainly depends on its diffusion rate inside channels. For example, at higher temperature, the ion flux increases more than the water flux, leading to a decrease in selectivity. With increasing feed (NaCl solution) concentration, for the zeolites with a negatively charged surface (e.g. ZSM-5), ion flux is significantly increased because the higher concentration increases both the driving force and effective pore size (Li et al., 2008b, Li and Wang, 2010). The possible reason is that with an increase in ion concentration, the electrically charged double layer formed at the membrane surface may shrink due to the screening effect of cations on the surface (Labbez et al., 2003), resulting in an increase of the effective pore size for ion passage (Huisman et al., 1998).

Also, the presence of other cations (e.g. Ca^{2+}, Al^{3+}) has an effect on the water flux and NaCl rejection decreases since the cations influence effective pore sizes and ion-water interactions. The strong screening effect of the high valence cations on the zeolite surface potential gives rise to the opening of inter-crystal pores for ion flow (Li et al., 2008b).

An experimental study on comparison of RO performances between silicalite (all-Si MFI-type) and ZSM-5 (Al-containing MFI) was carried out (Duke et al., 2009). Silicalite was expected to be a better RO performer than the Al-containing type due to its monopolar surface charge. Additionally, same experimental and simulation works have been carried out on the water dynamics in MFI-type zeolites with different chemistries at varying temperature and the loading number of water molecules (Zhang et al., 2012, Arı et al., 2009, Ahunbay, 2011). The results indicated that water diffusivities in pores are improved with increasing temperature and hydrophobicity of inner channels (e.g. silicalites) as expected, whereas water adsorption by MFI zeolites is higher for hydrophilic ZSM-5 (Al-containing MFI) than that of its counterparts since Al in zeolite frameworks provides hydrophilicity and hydrophilic surface functionalities (e.g. OH^{-}) contribute to water adsorption enhancement.

Although, apart from the applied pressure, the driving factors of water transport have not been clearly explained in RO process to date, it could be inferred from the previous studies that hydrophilic zeolites could absorb water more significantly than non-hydrophilic zeolites, while hydrophobic inner pores could have a lubricating effect so that water passes through quicker than in hydrophilic pores. In addition, zeolite pore size and shape is another key factor that influences water movement. Thus, a deeper molecular-level understanding of water transport through porous zeolites will be of importance for development of future RO membrane materials. In addition, other types of zeolites which have yet to be studied for their potential as membrane materials should be investigated in detail since only a few types of zeolite have been examined.

2.4 Summary

There are a broad range of membrane materials including organic, inorganic and hybrid materials. (e.g. polymeric, polymer composites, inorganic, and organic-inorganic composite membranes)

Nanoporous materials (e.g. CNTs, graphenes, zeolites) have attracted massive research interest as RO desalination membranes due to their high thermal, chemical, and mechanical stabilities compared to conventional polymeric membranes. Among these candidates for the membrane, zeolites are promising materials because of their variety of crystalline structures and chemistries which could be suitable for RO desalination. Experimental studies have examined several types of zeolite for their suitability as RO membranes, then show some potentials, but have found that they are not practical due to low water permeability.

To date, only a few types of zeolite have been intensively studied, which are LTA-types (e.g. zeolite A) and MFI-types (e.g. ZSM-5). It is therefore necessary to investigate some other forms of potential zeolite, and to obtain a deep understanding to such materials for future use of desalination membranes. In this chapter, we discussed some of the features of membranes that determine their suitability as RO membranes.

This thesis will focus on zeolites, and two of the key questions: the dependence of diffusion of water through zeolites on the pore structure; and the influence of the structure of the pore opening on the entry of water and ions into a zeolite pore.

References

AHLBERG, P., JOHANSSON, F. O. L., ZHANG, Z.-B., JANSSON, U., ZHANG, S.-L., LINDBLAD, A. & NYBERG, T. 2016. Defect formation in graphene during low-energy ion bombardment. *APL Mater.,* 4**,** 046104.

AHUNBAY, M. G. 2011. Monte Carlo Simulation of Water Adsorption in Hydrophobic MFI Zeolites with Hydrophilic Sites. *Langmuir,* 27**,** 4986-4993.

ALEXIADIS, A. & KASSINOS, S. 2008. Molecular Simulation of Water in Carbon Nanotubes. *Chemical Reviews,* 108**,** 5014-5034.

Arı, M. U., AHUNBAY, M. G., YURTSEVER, M. & ERDEM-ŞENATALAR, A. 2009. Molecular Dynamics Simulation of Water Diffusion in MFI-Type Zeolites. *Journal of Physical Chemistry B,* 113**,** 8073-8079.

BAE, S., KIM, H., LEE, Y., XU, X., PARK, J.-S., ZHENG, Y., BALAKRISHNAN, J., LEI, T., RI KIM, H., SONG, Y. I., KIM, Y.-J., KIM, K. S., OZYILMAZ, B., AHN, J.-H., HONG, B. H. & IIJIMA, S. 2010. Roll-to-roll production of 30-inch graphene films for transparent electrodes. *Nat Nano,* 5**,** 574-578.

BAERLOCHER, Ch. & MCCUSKER, L. B. 2015. *Database of Zeolite Structures* [Online]. http://www.iza-structure.org/databases/, IZA-SC. Available: http://www.iza-structure.org/databases/ [Accessed 15 Sep 2016].

BASTA, A. H., EL-SAIED, H. & ELBERRY, M. 2003. Cellulose membranes for reverse osmosis Part II. Improving RO membranes prepared from non-woody cellulose. *Desalination,* 159**,** 183-196.

BELFER, S., PURINSON, Y., FAINSHTEIN, R., RADCHENKO, Y. & KEDEM, O. 1998a. Surface modification of commercial composite polyamide reverse osmosis membranes. *Journal of Membrane Science,* 139**,** 175-181.

BELFER, S., PURINSON, Y. & KEDEM, O. 1998b. Surface modification of commercial polyamide reverse osmosis membranes by radical grafting: An ATR-FTIR study. *Acta Polymerica,* 49**,** 574-582.

BUNCH, J. S., VERBRIDGE, S. S., ALDEN, J. S., VAN DER ZANDE, A. M., PARPIA, J. M., CRAIGHEAD, H. G. & MCEUEN, P. L. 2008. Impermeable Atomic Membranes from Graphene Sheets. *Nano Letters,* 8**,** 2458-2462.

CEYHAN, T., TATLIER, M. & AKÇAKAYA, H. 2007. In vitro evaluation of the use of zeolites as biomaterials: effects on simulated body fluid and two types of cells. *Journal of Materials Science: Materials in Medicine,* 18**,** 1557-1562.

CORRY, B. 2008. Designing carbon nanotube membranes for efficient water desalination. *Journal of Physical Chemistry B,* 112**,** 1427-1434.

DARWISH, M. A. & EL-DESSOUKY, H. 1996. The heat recovery thermal vapour-compression desalting system: A comparison with other thermal desalination processes. *Applied Thermal Engineering,* 16**,** 523-537.

DROBEK, M., YACOU, C., MOTUZAS, J., JULBE, A., DING, L. & DINIZ DA COSTA, J. C. 2012. Long term pervaporation desalination of tubular MFI zeolite membranes. *Journal of Membrane Science,* 415–416**,** 816-823.

DUKE, M. C., O'BRIEN-ABRAHAM, J., MILNE, N., ZHU, B., LIN, J. Y. S. & DA COSTA, J. C. D. 2009. Seawater desalination performance of MFI type membranes made by secondary growth. *Separation and Purification Technology,* 68**,** 343-350.

EL-SAIED, H., BASTA, A. H., BARSOUM, B. N. & ELBERRY, M. M. 2003. Cellulose membranes for reverse osmosis Part I. RO cellulose acetate membranes including a composite with polypropylene. *Desalination,* 159**,** 171-181.

ELIMELECH, M. & PHILLIP, W. A. 2011. The Future of Seawater Desalination: Energy, Technology, and the Environment. *Science,* 333**,** 712-717.

ESHOUL, N. M., AGNEW, B., AL-WESHAHI, M. A. & ATAB, M. S. 2015. Exergy Analysis of a Two-Pass Reverse Osmosis (RO) Desalination Unit with and without an Energy Recovery Turbine (ERT) and Pressure Exchanger (PX). *Energies,* 8**,** 6910-6925.

FALK, K., SEDLMEIER, F., JOLY, L., NETZ, R. R. & BOCQUET, L. 2010. Molecular Origin of Fast Water Transport in Carbon Nanotube Membranes: Superlubricity versus Curvature Dependent Friction. *Nano Letters,* 10**,** 4067-4073.

FERJANI, E., LAJIMI, R. H., DERATANI, A. & ROUDESLI, M. S. 2002. Bulk and surface modification of cellulose diacetate based RO/NF membranes by polymethylhydrosiloxane - Preparation and characterization. *Desalination,* 146**,** 325-330.

FERJANI, E., MEJDOUB, M., ROUDESLI, M. S., CHEHIMI, M. M., PICARD, D. & DELAMAR, M. 2000. XPS characterization of poly(methylhydrosiloxane)-modified cellulose diacetate membranes. *Journal of Membrane Science,* 165**,** 125-133.

FERJANI, E. & ROUDESLI, M. S. 2000. Modification by polymethylhydrosiloxane and characterization of reverse-osmosis cellulose acetate membranes. *European Polymer Journal,* 36**,** 35-49.

FILIPPOV, A., DVINSKIKH, S. V., KHAKIMOV, A., GRAHN, M., ZHOU, H., FURO, I., ANTZUTKIN, O. N. & HEDLUND, J. 2012. Dynamic properties of water in silicalite-1 powder. *Magnetic Resonance Imaging,* 30**,** 1022-1031.

FIRST, E. L., GOUNARIS, C. E., WEI, J. & FLOUDAS, C. A. 2011. Computational characterization of zeolite porous networks: an automated approach. *Physical Chemistry Chemical Physics,* 13**,** 17339-17358.

FISCHBEIN, M. D. & DRNDIĆ, M. 2008. Electron beam nanosculpting of suspended graphene sheets. *Applied Physics Letters,* 93**,** 113107.

FREGER, V., GILRON, J. & BELFER, S. 2002. TFC polyamide membranes modified by grafting of hydrophilic polymers: an FT-IR/AFM/TEM study. *Journal of Membrane Science,* 209**,** 283-292.

GASCON, J., KAPTEIJN, F., ZORNOZA, B., SEBASTIAN, V., CASADO, C. & CORONAS, J. 2012. Practical Approach to Zeolitic Membranes and Coatings: State of the Art, Opportunities, Barriers, and Future Perspectives. *Chemistry of Materials,* 24**,** 2829-2844.

GHOSH, A. K. & HOEK, E. M. V. 2009. Impacts of support membrane structure and chemistry on polyamide-polysulfone interfacial composite membranes. *Journal of Membrane Science,* 336**,** 140-148.

GHOSH, A. K., JEONG, B. H., HUANG, X. F. & HOEK, E. M. V. 2008. Impacts of reaction and curing conditions on polyamide composite reverse osmosis membrane properties. *Journal of Membrane Science,* 311**,** 34-45.

GIWA, A., AKTHER, N., DUFOUR, V. & HASAN, S. W. 2016. A critical review on recent polymeric and nano-enhanced membranes for reverse osmosis. *RSC Advances,* 6**,** 8134-8163.

GRANDA-VALDÉS, M., PÉREZ-CORDOVES, A. I. & DÍAZ-GARCÍA, M. E. 2006. Zeolites and zeolite-based materials in analytical chemistry. *Trends in Analytical Chemistry,* 25**,** 24-30.

HOLT, J. K., PARK, H. G., WANG, Y. M., STADERMANN, M., ARTYUKHIN, A. B., GRIGOROPOULOS, C. P., NOY, A. & BAKAJIN, O. 2006. Fast mass transport through sub-2-nanometer carbon nanotubes. *Science,* 312**,** 1034-1037.

HUISMAN, I. H., TRÄGÅRDH, G., TRÄGÅRDH, C. & PIHLAJAMÄKI, A. 1998. Determining the zeta-potential of ceramic microfiltration membranes using the electroviscous effect. *Journal of Membrane Science,* 147**,** 187-194.

HUMPLIK, T., LEE, J., O’HERN, S. C., FELLMAN, B. A., BAIG, M. A., HASSAN, S. F., ATIEH, M. A., RAHMAN, F., LAOUI, T., KARNIK, R. & WANG, E. N. 2011. Nanostructured materials for water desalination. *Nanotechnology,* 22**,** 292001.

IL KIM, H. & KIM, S. S. 2006. Plasma treatment of polypropylene and polysulfone supports for thin film composite reverse osmosis membrane. *Journal of Membrane Science,* 286**,** 193-201.

INUKAI, S., CRUZ-SILVA, R., ORTIZ-MEDINA, J., MORELOS-GOMEZ, A., TAKEUCHI, K., HAYASHI, T., TANIOKA, A., ARAKI, T., TEJIMA, S., NOGUCHI, T., TERRONES, M. & ENDO, M. 2015. High-performance multi-functional reverse osmosis membranes obtained by carbon nanotube·polyamide nanocomposite. *Scientific Reports,* 5**,** 13562.

JEONG, B. H., HOEK, E. M. V., YAN, Y. S., SUBRAMANI, A., HUANG, X. F., HURWITZ, G., GHOSH, A. K. & JAWOR, A. 2007. Interfacial polymerization of thin film nanocomposites: A new concept for reverse osmosis membranes. *Journal of Membrane Science,* 294**,** 1-7.

JIANG, J. W., BABARAO, R. & HU, Z. Q. 2011. Molecular simulations for energy, environmental and pharmaceutical applications of nanoporous materials: from zeolites, metal-organic frameworks to protein crystals. *Chemical Society Reviews,* 40**,** 3599-3612.

JIN, Y. & SU, Z. H. 2009. Effects of polymerization conditions on hydrophilic groups in aromatic polyamide thin films. *Journal of Membrane Science,* 330**,** 175-179.

KANG, G.-D., GAO, C.-J., CHEN, W.-D., JIE, X.-M., CAO, Y.-M. & YUAN, Q. 2007a. Study on hypochlorite degradation of aromatic polyamide reverse osmosis membrane. *Journal of Membrane Science,* 300**,** 165-171.

KANG, G. D., LIU, M., LIN, B., CAO, Y. M. & YUAN, Q. 2007b. A novel method of surface modification on thin-film composite reverse osmosis membrane by grafting poly(ethylene glycol). *Polymer,* 48**,** 1165-1170.

KAZEMIMOGHADAM, M. 2010. New nanopore zeolite membranes for water treatment. *Desalination,* 251**,** 176-180.

KESIEME, U. K., MILNE, N., ARAL, H., CHENG, C. Y. & DUKE, M. 2013. Economic analysis of desalination technologies in the context of carbon pricing, and opportunities for membrane distillation. *Desalination,* 323**,** 66-74.

KHAWAJI, A. D., KUTUBKHANAH, I. K. & WIE, J.-M. 2008. Advances in seawater desalination technologies. *Desalination,* 221**,** 47-69.

KIM, C. K., KIM, J. H., ROH, I. J. & KIM, J. J. 2000. The changes of membrane performance with polyamide molecular structure in the reverse osmosis process. *Journal of Membrane Science,* 165**,** 189-199.

KIM, E. S., KIM, Y. J., YU, Q. S. & DENG, B. L. 2009. Preparation and characterization of polyamide thin-film composite (TFC) membranes on plasma-modified polyvinylidene fluoride (PVDF). *Journal of Membrane Science,* 344**,** 71-81.

KIM, J. H., MOON, E. J. & KIM, C. K. 2003. Composite membranes prepared from poly(m-animostyrene-co-vinyl alcohol) copolymers for the reverse osmosis process. *Journal of Membrane Science,* 216**,** 107-120.

KIM, S. H., KWAK, S.-Y. & SUZUKI, T. 2005. Positron Annihilation Spectroscopic Evidence to Demonstrate the Flux-Enhancement Mechanism in Morphology-Controlled Thin-Film-Composite (TFC) Membrane. *Environmental Science & Technology,* 39**,** 1764-1770.

KITAO, O., DEMIRALP, E., CAGIN, T., DASGUPTA, S., MIKAMI, M., TANABE, K. & GODDARD, W. A. 1999. Theoretical studies on VPI-5. 3. The MS-Q force field for aluminophosphate zeolites. *Computational Materials Science,* 14**,** 135-137.

KUMAKIRI, I., TSURU, T., NAKAO, S. & KIMURA, S. 2000. Reverse osmosis performance at high pressure with high water recovery. *Journal of Chemical Engineering of Japan,* 33**,** 414-419.

LABBEZ, C., FIEVET, P., SZYMCZYK, A., VIDONNE, A., FOISSY, A. & PAGETTI, J. 2003. Retention of mineral salts by a polyamide nanofiltration membrane. *Separation and Purification Technology,* 30**,** 47-55.

LEE, C., WEI, X., KYSAR, J. W. & HONE, J. 2008. Measurement of the Elastic Properties and Intrinsic Strength of Monolayer Graphene. *Science,* 321**,** 385-388.

LEE, K. P., ARNOT, T. C. & MATTIA, D. 2011. A review of reverse osmosis membrane materials for desalination-Development to date and future potential. *Journal of Membrane Science,* 370**,** 1-22.

LEIGGENER, C., CURRAO, A. & CALZAFERRI, G. 2008. Zeolite A and ZK-4. *In:* SCHUBERT, U., HÜSING, N. & LAINE, R. (eds.) *Materials Syntheses.* Springer Vienna.

LI, D. & WANG, H. T. 2010. Recent developments in reverse osmosis desalination membranes. *Journal of Materials Chemistry,* 20**,** 4551-4566.

LI, L., ZHANG, S. B., ZHANG, X. S. & ZHENG, G. D. 2007a. Polyamide thin film composite membranes prepared from 3,4',5-biphenyl triacyl chloride, 3,3',5,5'-biphenyl tetraacyl chloride and m-phenylenediamine. *Journal of Membrane Science,* 289**,** 258-267.

LI, L., ZHANG, S. B., ZHANG, X. S. & ZHENG, G. D. 2008a. Polyamide thin film composite membranes prepared from isomeric biphenyl tetraacyl chloride and m-phenylenediamine. *Journal of Membrane Science,* 315**,** 20-27.

LI, L. X., DONG, J. H. & NENOFF, T. M. 2007b. Transport of water and alkali metal ions through MFI zeolite membranes during reverse osmosis. *Separation and Purification Technology,* 53**,** 42-48.

LI, L. X., DONG, J. H., NENOFF, T. M. & LEE, R. 2004a. Desalination by reverse osmosis using MFI zeolite membranes. *Journal of Membrane Science,* 243**,** 401-404.

LI, L. X., DONG, J. H., NENOFF, T. M. & LEE, R. 2004b. Reverse osmosis of ionic aqueous solutions on a MFI zeolite membrane. *Desalination,* 170**,** 309-316.

LI, L. X., LIU, N., MCPHERSON, B. & LEE, R. 2008b. Influence of counter ions on the reverse osmosis through MFI zeolite membranes: implications for produced water desalination. *Desalination,* 228**,** 217-225.

LIN, J. & MURAD, S. 2001. A computer simulation study of the separation of aqueous solutions using thin zeolite membranes. *Molecular Physics,* 99**,** 1175-1181.

LIU, N., LI, L. X., MCPHERSON, B. & LEE, R. 2008. Removal of organics from produced water by reverse osmosis using MFI-type zeolite membranes. *Journal of Membrane Science,* 325**,** 357-361.

LUCCHESE, M. M., STAVALE, F., FERREIRA, E. H. M., VILANI, C., MOUTINHO, M. V. O., CAPAZ, R. B., ACHETE, C. A. & JORIO, A. 2010. Quantifying ion-induced defects and Raman relaxation length in graphene. *Carbon,* 48**,** 1592-1597.

MADAENI, S. S., BARZIN, J. & JOKAR, Z. 2009. Evaluation of the Morphology and Performance of Polyether Sulfone Reverse Osmosis Composite and Non-composite Membranes. *Polymers & Polymer Composites,* 17**,** 101-108.

MAJUMDER, M., CHOPRA, N., ANDREWS, R. & HINDS, B. J. 2005. Nanoscale hydrodynamics: Enhanced flow in carbon nanotubes (vol 438, pg 44, 2005). *Nature,* 438**,** 930-930.

MALEKPOUR, A., MILLANI, M. R. & KHEIRKHAH, M. 2008. Synthesis and characterization of a NaA zeolite membrane and its applications for desalination of radioactive solutions. *Desalination*, 225**,** 199-208.

MCGINNIS, R. L. & ELIMELECH, M. 2007. Energy requirements of ammonia–carbon dioxide forward osmosis desalination. *Desalination,* 207**,** 370-382.

MURAD, S. 1996. Molecular dynamics simulations of osmosis and reverse osmosis in solutions. *Adsorption-Journal of the International Adsorption Society,* 2**,** 95-101.

MURAD, S. & POWLES, J. G. 1993. A computer-simulation of the classic experiment on osmosis and osmotic-pressure. *Journal of Chemical Physics,* 99**,** 7271-7272.

MURAD, S., RAVI, P. & POWLES, J. G. 1993. A computer-simulation study of fluids in model slit, tubular, and cubic micropores. *Journal of Chemical Physics,* 98**,** 9771-9781.

PETERSEN, R. J. 1993. Composite reverse-osmosis and nanofiltration membranes. *Journal of Membrane Science,* 83**,** 81-150.

RAVAL, H. D., RANA, P. S. & MAITI, S. 2015. A novel high-flux, thin-film composite reverse osmosis membrane modified by chitosan for advanced water treatment. *RSC Advances,* 5**,** 6687-6694.

RIGO, R. T., PRIGOL, C., ANTUNES, Â., Z. DOS SANTOS, J. H. & PERGHER, S. B. C. 2013. Synthesis of ZK4 zeolite: An LTA-structured zeolite with a Si/Al ratio greater than 1. *Materials Letters,* 102–103**,** 87-90.

RODRÍGUEZ-CALVO, A., SILVA-CASTRO, G. A., OSORIO, F., GONZÁLEZ-LÓPEZ, J. & CALVO, C. 2014. Novel Membrane Materials for Reverse Osmosis Desalination. *Hydrology: Current Research,* 5.

ROH, I. J., GREENBERG, A. R. & KHARE, V. P. 2006. Synthesis and characterization of interfacially polymerized polyamide thin films. *Desalination,* 191**,** 279-290.

SADRZADEH, M. & MOHAMMADI, T. 2008. Sea water desalination using electrodialysis. *Desalination,* 221**,** 440-447.

SAHA, N. K. & JOSHI, S. V. 2009. Performance evaluation of thin film composite polyamide nanofiltration membrane with variation in monomer type. *Journal of Membrane Science,* 342**,** 60-69.

SHENVI, S. S., ISLOOR, A. M. & ISMAIL, A. F. 2015. A review on RO membrane technology: Developments and challenges. *Desalination,* 368**,** 10-26.

SINT, K., WANG, B. & KRÁL, P. 2008. Selective Ion Passage through Functionalized Graphene Nanopores. *Journal of the American Chemical Society,* 130**,** 16448-16449.

SUK, M. E. & ALURU, N. R. 2010. Water Transport through Ultrathin Graphene. *Journal of Physical Chemistry Letters,* 1**,** 1590-1594.

SURWADE, S. P., SMIRNOV, S. N., VLASSIOUK, I. V., UNOCIC, R. R., VEITH, G. M., DAI, S.

& MAHURIN, S. M. 2015. Water desalination using nanoporous single-layer graphene. *Nat Nano,* 10**,** 459-464.

TRIVEDI, S. & ALAMEH, K. 2016. Effect of vertically aligned carbon nanotube density on the water flux and salt rejection in desalination membranes. *SpringerPlus,* 5**,** 1-13.

ZHANG, K., LIVELY, R. P., NOEL, J. D., DOSE, M. E., MCCOOL, B. A., CHANCE, R. R. & KOROS, W. J. 2012. Adsorption of Water and Ethanol in MFI-Type Zeolites. *Langmuir,* 28**,** 8664-8673.

Chapter 3 Molecular Dynamics Simulation and Application to Study of Transport through Zeolites

3.1 Principles of Molecular dynamics

Molecular dynamics (MD) simulation is one of the most powerful tools available to study molecular physics in systems on the atomic scale. Properties, that are almost impossible to access using experimental approaches, can be investigated; conditions highly controlled and molecular-level understanding of the processes obtained [see discussion in (Ebro et al., 2013, Schlick, 2002)]. For that reason, MD has been helpfully used to apply zeolites in various fields such as nanotechnology, biophysics, and materials science (Gascon et al., 2012, Jiang et al., 2011, Ceyhan et al., 2007). Specifically in the field of nanomaterials, MD is a powerful method to gain molecular-level insight into physical phenomena in nanoporous materials. By using MD, it is expected that quantification of nanoparticle movement through nanostructures and characterisation of the materials are achieved.

Classical molecular dynamics simulations are based on Newtonian mechanics. According to Newton's 2nd law of motion, there is a relationship between the force on particle i ($\mathbf{F}_i$), mass (m_i), and acceleration ($\boldsymbol{a}_i$)

$$\mathbf{F}_i = m_i \boldsymbol{a}_i = m_i \frac{d^2\mathbf{r}_i}{dt^2} \tag{3-1}$$

where $\mathbf{r}_i$ indicates the position of particle i, and t is time.

In a molecular system, the force on atom i ($\mathbf{F}_i$) can be defined as follows

$$\mathbf{F}_i = -\nabla_i U(\mathbf{r}_i) = -\frac{\partial U(\mathbf{r}^N)}{\partial \mathbf{r}_i} \tag{3-2}$$

where the force exerted on atom *i* is generated by the other *N-1* molecules, $U(\mathbf{r}^N)$ is potential energy which is a function of all the particles in the system, and $\mathbf{r}^N = (\mathbf{r}_1, \mathbf{r}_2, \ldots \mathbf{r}_N)$ represents a series of $3N$ molecular positions (Ebro et al., 2013). The kinetic energy of the system can be expressed as $K = \sum_{i=1}^{N} |\mathbf{p}_i|^2/2m_i$ where $\mathbf{p}_i$ is the momentum of atom *i*. Also, the total energy for the system can be described as a sum of the kinetic and potential energies ($H = K + U$). Now, the classic equations of motion for a system that conserves the total energy can be written as (Allen, 2004).

$$\dot{\mathbf{r}}_i = \frac{\mathbf{p}_i}{m_i} \tag{3-3a}$$

$$\dot{\boldsymbol{v}}_i = \frac{\mathbf{F}_i}{m_i} \tag{3-3b}$$

where $\boldsymbol{v}_i$ represents the velocity of atom *i*. The motion of all atoms can be defined by their successive positions, velocities, and forces generated from the combination of equations 3-2 and 3-3. In practice, the positions and velocities of the particles are evolved with a time interval by numerically integrating the first-order differential equations 3-3. This molecular trajectory is a basis of predicting a bulk system, and relating it to physical phenomena.

The most widely used integrator in MD simulations is the Verlet algorithm. There are different versions which have been employed, such as the classical form and a 'leapfrog' form (Verlet, 1967, Verlet, 1968, Hockney and Eastwood, 1988a). In this thesis, however, we focus on a 'velocity' Verlet form that is commonly used and is employed in numerical calculations in the present project. The general equation for this integrator can be expressed from the Taylor expansions for the particle positions and velocities; it is as written below (Meller, 2001, Allen, 2004).

$$\boldsymbol{v}_i\left(t + \frac{1}{2}\Delta t\right) \cong \boldsymbol{v}_i(t) + \frac{1}{2}\Delta t \frac{\mathbf{F}_i(t)}{m_i} \tag{3-4a}$$

$$\mathbf{r}_i(t + \Delta t) \cong \mathbf{r}_i(t) + \Delta t \, \boldsymbol{v}_i\left(t + \frac{1}{2}\Delta t\right) \tag{3-4b}$$

$$v_i(t+\Delta t) \cong v_i\left(t+\frac{1}{2}\Delta t\right)+\frac{1}{2}\Delta t\frac{\mathbf{F}_i(t+\Delta t)}{m_i} \tag{3-4c}$$

In equations (3-4), Δt indicates time step. The velocities and positions can be propagated in this scheme.

Each of the atoms in a given system interacts with neighbouring atoms, and the interaction potential can be defined using two main approaches. This mathematically-defined potential is called a 'force field'. One approach is the ab initio method used to derive the force field, which solves electronic structures of atomic nuclei from quantum mechanics, then calculates the interatomic potential and fits these results to a functional form. In many cases, the ab initio force field represents accurate and precise interatomic potentials, but allows us to calculate only a small molecular system (hundreds of atoms) for time scales of hundreds of picoseconds, resulting in difficulties describing the macroscale properties of molecules such as their bulk dynamics and structures. The empirical method determines the interatomic potential by approximation of the potentials from experimental results. The potential has bonding and non-bonding contributions. From such interactions, the potential energy terms can be determined (Weiner et al., 1986, Jorgensen et al., 1984, van Gunsteren and Berendsen, 1987, Mayo et al., 1990, Smith et al., 2012). The total interaction potential (U_{tot}) of the molecular system can be expressed as a sum of contributions due to various interactions. A commonly used form is:

$$U_{tot} = U_{bond} + U_{ang} + U_{dihed} + U_{vdW} + U_{coul} \tag{3-5}$$

where U_{bond}, U_{ang}, and U_{dihed} are bonding intramolecular interactions representing the stretching, bending, and torsion which occur between bonded atoms, respectively. U_{vdW} and U_{coul} indicate van der Waals interactions and electrostatic interactions, respectively, both types describe non-bonded interactions and can be employed to represent intramolecular and/or intermolecular interactions, sometimes used to define the dihedrals (torsion motions). A set of such mathematical functions and numerical parameters is used to represent the potential energy of a system of atoms in molecular simulations. This method can reproduce the bulk behaviour of the molecules well if sufficient experimental data is available, as the force field is derived by fitting experimental results. It also can be used to simulate a much bigger system containing hundreds of thousands of atoms for nanoseconds or even microseconds. However, it applies to the particular system and conditions used in the parameterisation, and its transferability to different systems and other conditions must always be validated. The interaction terms to be included in the total energy and input parameters are varied depending not only on different molecular systems, but on methods to derive the potentials and parameters. In the present thesis, only U_{bond}, U_{ang}, U_{vdW} and U_{coul} terms will be adopted to model zeolites, water, and salt ions. Detailed specifications of the functional forms and numerical parameters will be dealt with in further chapters 4, 5, and 6.

To model bulk systems, periodic boundary conditions (PBC) are commonly used. PBCs make the simulation system like an infinite bulk system to prevent problems caused by finite boundary effects as the PBC removes the boundary effect. This algorithm assumes the simulated unit cell is a single repeating unit of the large scale system, and enables us to calculate and predict the bulk properties of the unit as shown in Figure 3-1 for a 2-D system. However for very small simulation systems or statistically-nonequilibrated systems, the use of the PBCs leads to deviations from the bulk system, which may be due to truncation of the correlation interactions.

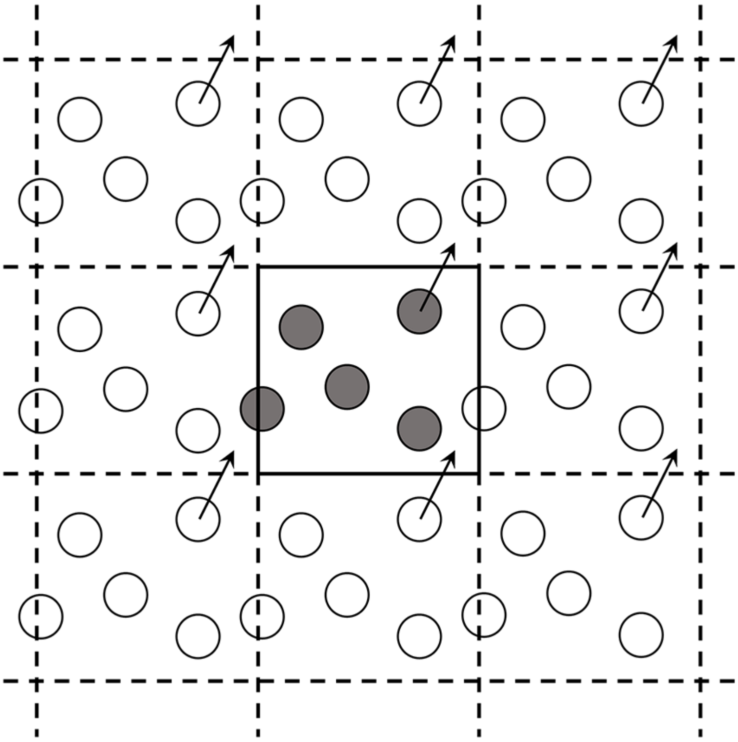

Figure 3-1 An illustration of 2-D periodic system. Particles in a unit box can move to or from the periodic replicas. Once a particle crosses over the box boundary, an image particle moves in from the opposite side to replace it. Both real (filled) and image (empty) neighbouring particles are taken into account for the interaction calculations.

In MD simulations, when calculating non-bonded atom-atom (pairwise) interactions, in principle, a large number of pairwise interactions must be taken into account to consider all possible interactions between each atom i and all other surrounding atoms j. This may consume a substantial computing time, i.e. a high cost. Due to this reason, it is generally assumed that the pairwise interactions are short-ranged, which means U_{vdW} (r_{ij}) = 0 if the pair distance goes beyond certain distance, $r_{ij} > r_{\mathrm{cut}}$ (Jensen, 2007). This is called potential cutoff, and is able to save the computing time by excluding some pairwise calculations. However, although this algorithm makes the simulation more efficient, still a considerable time will be required. To make a MD simulation more economic, lists of neighbouring pairs of atoms can be introduced. Verlet suggested that a potential sphere around an atom is surrounded by a skin, giving a larger sphere (Verlet, 1967) as shown in Figure 3-2.

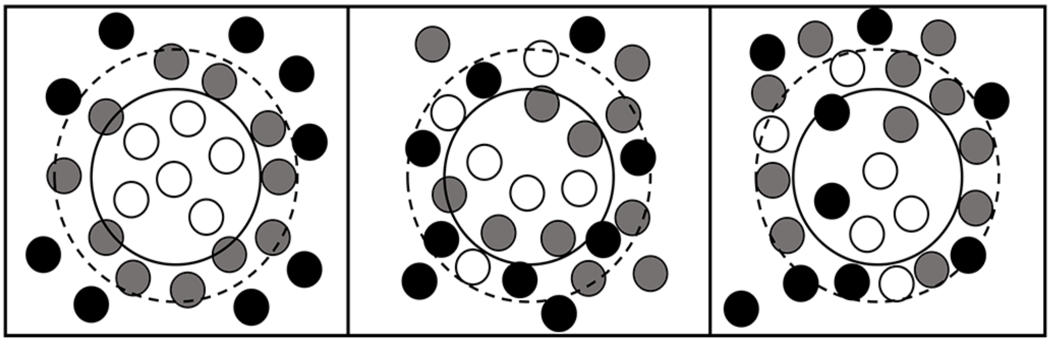

Figure 3-2 A neighbour list on its initial construction, and changes in atomic positions every several time-steps. The large solid circle represents a potential cutoff sphere, and the dashed circle indicates a list sphere. White particles represent atoms inside the cutoff sphere, and grey particles are atoms between the list and cutoff spheres. The list must be rebuilt before atoms originally outside the list boundary (black particles) have entered the potential cutoff range.

Here the potential sphere is defined by radius of the cutoff r_{cut}, and the extended sphere is called ‘list’ and defined by radius of the list r_{list}. A neighbour list is built in which all the neighbour atoms of each atom appear, for the pair distance within r_{list} at the beginning of a simulation, then the pairs in the list are used in the force/energy evaluation routine over the next few time steps. Atoms that originally appear on the list may move in and out of the potential sphere, but they are always considered, until a new list is formed. From time to time, the list must be rebuilt. This occurs if any of the pairs outside the list has moved into the potential cutoff boundary. It is thus important to update the neighbour list automatically in order to accurately refine the pairwise interaction. The list radius r_{list} is a compromise parameter that you are free to choose, but must be longer than the cutoff radius since the parameter is set as the cutoff plus the estimated distance particles may move in certain time-steps. The larger list will reduce the frequency of the list updates, but will not make an efficient saving on computing time compared to the smaller list (Allen and Tildesley, 1987).

In addition to computing the short-range interactions, the correct handling of long-range interactions is another key issue in evaluating non-bonded interactions. The electrostatic charge (Coulombic interaction) can be defined by both short- and long-range potentials. As for the van der Waals interaction, the short-range (real contribution) of Coulombic interaction is evaluated using the distance between atomic charges and the potential cutoff r_{cut}:

$$U_{coul}(r_{ij}) = \frac{q_i q_j}{4\pi\epsilon_0 r_{ij}} \tag{3-6}$$

where q_i, q_j are the charges on atoms i, j and ϵ_0 is the permittivity of free space. However, the long-range Coulombic charges (imaginary contribution) take the simulation cell and its periodic images into account. The long-range interaction can be defined as

$$U_{coul} = \frac{1}{4\pi\epsilon_0} \sum_{\mathbf{n}} \left(\sum_{i=1}^{N-1} \sum_{j=i+1}^{N} q_i q_j \left| \mathbf{r}_{ij} + \mathbf{n} \right|^{-1} \right) \tag{3-7}$$

where **n** is the lattice vector $\mathbf{n} = (n_x L_x, n_y L_y, n_z L_z)$ and **r** is the distance vector $(r_{xij}, r_{yij}, r_{zij})$ between atoms i and j. The summation of the terms in equation (3-7) converges if the summation is carried out in an appropriate order. The Ewald sum is one of the most widely used summation methods to evaluate the long-range interaction (Allen and Tildesley, 1987, Essmann et al., 1995, Toukmaji and Board, 1996). This scheme involves a decomposition of the summation in equation (3-7) into two rapidly convergent terms. The scheme works by surrounding each charge in a system by a charge distribution of equal magnitude and opposite sign. The counter-charge screens the original long-range potential, making it short-ranged. Then this is added in real space. Also, an imaginary charge distribution of the same sign as the charges is introduced to cancel out the effect of the screening charge. This second is added in reciprocal space. However, this method can be computationally-expensive for a large system since the computing time is proportional to $N^{\frac{3}{2}}$. Thus, some alternative schemes have been developed. One of such widely adopted methods is the Particle-Particle-Particle mesh (PPPM) Ewald sum (Hockney and Eastwood, 1988b). The scaling of PPPM is faster than that of Ewald, and is $N \ln N$ times. In this summation, short-range interactions are directly calculated and long-range interactions are measured by interpolating the charges onto a mesh. Thus, Poisson's equation (Jackson, 1999), which describes the electric field formed by the charge distribution, can be solved on this mesh to calculate the interactions. In such method, there are several variants to interpolate the charges onto a mesh (Toukmaji and Board, 1996).

In many cases of MD simulations, molecules in a system are simply modelled using non-bonded interaction terms (i.e. $U_{vdW} + U_{coul}$) for their intramolecular and intermolecular potentials. For some other molecules, that have a flexible geometry but tend to stay close to their most stable geometry such as solids, intramolecular bonding interactions must be considered. These molecules can be generally constructed by the following bonding terms

$$U_{bond}\left(r_{ij}\right) = \frac{1}{2}k_r\left(r_{ij} - r_0\right)^2 \tag{3-8}$$

$$U_{ang}\left(\theta_{jik}\right) = \frac{1}{2}k_\theta\left(\theta_{jik} - \theta_0\right)^2 \tag{3-9}$$

where k_r, k_θ are the bond force constant and the angle force constant, respectively, and r_0 is the equilibrium bond distance. θ_{jik} indicates the angle made by atoms j, k around the centred atom i, and θ_0 is the equilibrium angle. By means of the bonding terms, it is assumed that the bond involves a stretching motion between adjacent atoms in a molecule by a harmonic potential with the specified equilibrium distance while the three-atom angle has a bending motion by a harmonic oscillation with the equilibrium angle. These mathematical models in MD simulations have been used as reliable representations for intramolecular motion. Thus, they will be adopted and employed for modelling bonded structures in the rest of the thesis. Another form of bonding interaction will be also used to evaluate some specific case, and will be dealt with in detail for Chapter 6.

If intramolecular bonding interactions are not the main focus of interest, it is also common to keep molecules rigid, in order to increase computational efficiency, and to avoid unwanted classical contributions made from modes involving high bonding frequencies, which is for most ranges of temperature of interest in the ground state. The method to achieve this is called a 'Bond constraint' that is often used to make molecules, formed by bonding terms, rigid by fixing the bond length and angle. Thus, the rigid molecule is assumed to be a reasonable model for its experimental one, and its rigidity makes no significant effects on other molecules in a system. In classical mechanics, in general the constraint algorithm can be implemented through the method of Lagrangian multipliers (Goldstein, 1980). For instance, if there are two atoms *i* and *j* with a fixed bond length *b*, given their atomic coordinates, equations for the bond constraint can be written as

$$\chi(\mathbf{r}_i, \mathbf{r}_j) = (\mathbf{r}_i - \mathbf{r}_j) \cdot (\mathbf{r}_i - \mathbf{r}_j) - b^2 = 0 \qquad \text{(3-10a)}$$

$$\dot{\chi}(\mathbf{r}_i, \mathbf{r}_j) = 2(v_i - v_j) \cdot (\mathbf{r}_i - \mathbf{r}_j) = 0 \qquad \text{(3-10b)}$$

In equations of motion, the constraint forces exerted on the atoms will be added to the interaction forces to give

$$m_i \ddot{\mathbf{r}}_i = \mathbf{F}_i + \Lambda \boldsymbol{g}_i \qquad \text{(3-11)}$$

where Λ is the undetermined multiplier.

$$\boldsymbol{g}_i = -\frac{\partial \chi}{\partial \mathbf{r}_i} = -2(\mathbf{r}_i - \mathbf{r}_j) \qquad \text{(3-12a)}$$

$$\boldsymbol{g}_j = -\frac{\partial \chi}{\partial \mathbf{r}_j} = 2(\mathbf{r}_i - \mathbf{r}_j) \qquad \text{(3-12b)}$$

Considering one constraint to be imposed, the multiplier Λ can be simply calculated through equations (3-12). In general, however multiple constraints can be carried out, and will be generating a number of the equations. Thus, the constraints will become more violated as the simulation proceeds since the equations of motion are propagated by some approximation scheme in specified time steps (i.e. the numerical error will be propagated) (Allen, 2004). To rectify this issue, various ideas have been developed to determine the constraint forces, then to apply them in a way that the constraints are properly executed at the end of each time step specified. For the Verlet integration, this algorithm is called SHAKE (Ryckaert et al., 1977). The SHAKE algorithm will be used for rigid water molecules we model in further chapters.

Figure 3-3 shows a flowchart for molecular dynamics simulations. As shown in the diagram, the simulations involve producing trajectories and then using them in order to calculate the properties of the system (Ebro et al., 2013, Haile, 1992).

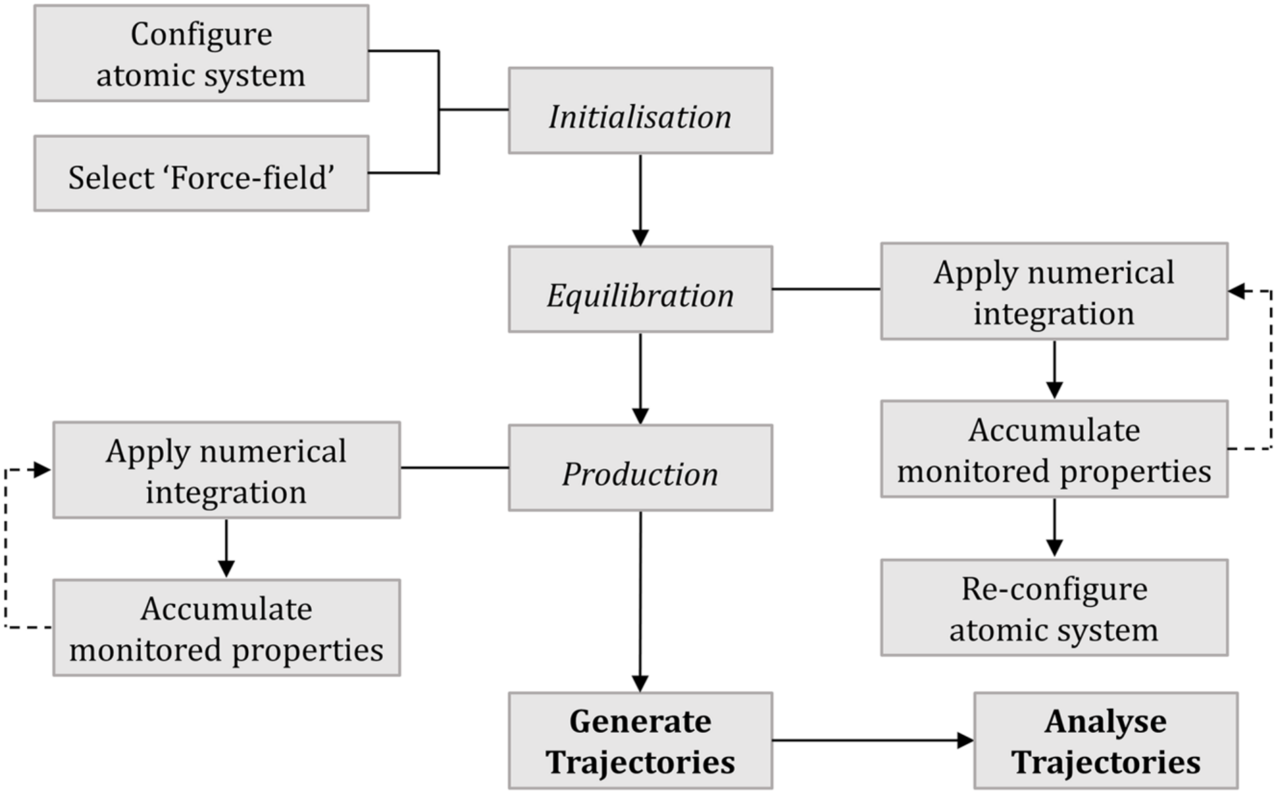

Figure 3-3 Flowchart of molecular dynamics simulations [Adopted and modified from Ref (Ebro et al., 2013)].

In many cases, storing the trajectories produced in MD for the water transport process is of importance since trajectories can be the raw data to be processed and analysed to obtain the properties of the system at a further stage. Generating trajectories involves three main steps: initialisation; equilibration; and production (Haile, 1992, Schlick, 2002). In initialisation, the number and type of atoms in the system, boundary conditions, and system size should be set. In addition, the particles' initial positions, velocities, and forces can be normally set up at this stage by building an initial atomic configuration, assigning random velocities to the atoms, and calculating forces on the atoms using the chosen force-field potential. Since the initial state is unlikely to be typical of the equilibrium distribution, it should be simulated to relax to its equilibrated level. This takes place in the equilibration step. There are both internal and external factors contributing to the equilibrium state. All potential terms that represent bonding and non-bonding interactions occurring in the molecular system are the internal factors, and the external factors include temperature and pressure controls: the thermostat and barostat, respectively. Two general methods are often used to simulate a molecular system under constant temperature rather than constant energy. One simple and reliable approach is to rescale atomic velocities of the system at every certain interval (Andersen, 1980). This random velocity assignment obeys the Maxwell-Boltzmann distribution. So-called ‘velocity rescaling’ can be defined as an occasional random coupling with a thermal bath. The random rescaling may apply to individual atoms, or to the whole system. Another common method is to introduce an external thermal reservoir which is linked to the system (Hoover, 1985, Allen, 2004). An example is the ‘Nosé-Hoover thermostat’ which will modify the general equations of motion given earlier as

$$\dot{\mathbf{r}}_i = \frac{\mathbf{p}_i}{m_i} \tag{3-13a}$$

$$\dot{\mathbf{p}}_i = \mathbf{F}_i - \xi \mathbf{p}_i \tag{3-13b}$$

$$\dot{\xi} = \frac{\sum_{i=1}^{N} \mathbf{p}_i^2/m_i - N_f k_B T_0}{Q} \equiv v_T^2 \left[\frac{\sum_{i=1}^{N} \mathbf{p}_i^2/m_i}{N_f k_B T_0} - 1\right] = v_T^2 \left[\frac{T}{T_0} - 1\right] \tag{3-13c}$$

where ξ indicates a friction coefficient that can be varied in time. Q is a thermal damping parameter which is redefined by a relaxation rate v_T for thermal fluctuations, N_f ($\approx 3N$) is the number of degrees of freedom, T_0 stands for the selected temperature to be kept constant, and T is the instantaneous temperature. When the system temperature is higher than the target temperature ($T > T_0$), the friction coefficient ξ will increase (be positive), then the system will start to cool down. The reverse situation will take place when $T < T_0$. In some cases for heterogeneous systems or nonequilibrium conditions (e.g. water absorption in nanopores or fluid flow through nanostructures), this scheme may produce non-ergodic molecular behaviour, i.e. $\sum_{i=1}^{N} \mathbf{p}_i \neq 0$

(Krishnan et al., 2013, Yong and Zhang, 2013), but it can be cancelled out by employing multiple chains of the thermal reservoir. Similar approaches can be also used to fix the pressure of the system, which are called 'barostat'. Further details on thermostat and also barostat, how these ensemble methods are applied to and their effects on the molecular system will be discussed in Chapter 4.

For studies of water diffusion in zeolites, in the equilibration stage, the water molecules should be allowed to relax within the framework of membrane atoms that are already equilibrated or allowed to equilibrate to typical positions at the same time as the water. This step ensures that the randomly assigned initial values for position and velocity will not affect the system to be simulated. In the final step, production, the main MD simulation is done with a defined number of time steps after the system has been equilibrated. During this period, the raw data or trajectories, are analysed and stored for analysis and prediction of system properties using post-processing. This trajectory cannot be directly obtained from experiments due to the difficulty of measuring the time evolution of all the positions and momenta of all the particles in a system, so MD simulations play a pivotal role in predicting many practical bulk properties and understanding the property of nano-scale system (Haile, 1992, Nasrabadi and Foroutan, 2011). One of the post-processing methods to evaluate transport properties of molecules is a diffusion coefficient measurement. This measurement can be quantified in two ways through the self-diffusion coefficient and collective diffusion coefficient. The self-diffusion coefficient is indicative of the molecular mobility by representing the spontaneous mixing of molecules among themselves, and the collective diffusion coefficient is directly related to the transport diffusion (Gubbins et al., 2011) that indicates the ratio of the flux of molecules in a fluid to a concentration gradient (Smith and Hashemi, 2009). In studying water diffusion in zeolites, thus the water mobility and flux through nanopores of zeolites can be quantitatively examined by these diffusion measurements.

The investigation into this spontaneous molecular mixing and/or bulk movement is carried out using equilibrium molecular dynamics simulations. Sometimes non-equilibrium molecular dynamics methods are employed to study the transport properties of molecules by applying external forces like a pressure gradient, mimicking the real conditions. This approach might give us a more intuitive value for the fluid flux, however in this case the equilibrium results were computationally efficient. Thus, in the present thesis, we focus on the equilibrium MD approach to examine the diffusion properties. Mathematical means to calculate both coefficient calculations and their applications will be discussed in depth for studies in further chapters.

Another method to examine structural properties of molecules is a distribution function that measures the average value of a probability as a function of an independent variable. One typical example is the radial distribution function that evaluates the probability of finding an atom of interest as a function of distance from a centred atom in respect to that atom expected from bulk (a completely uniform distribution) (Jensen, 2007). Figure 3-4 shows a schematic image representing a simple case of particle distribution.

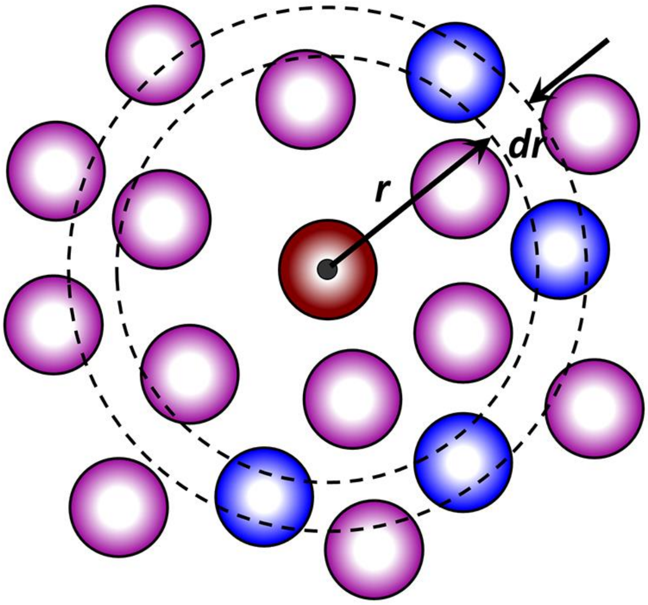

Figure 3-4 A schematic representation of an example of particle distribution in the radial distribution function measurement.

Here the probability of finding the particle of interest can be given by the number of particles, in a spherical shell between r and $r + dr$, relative to the total average number of particles in a sphere with radius r. For water molecules in zeolites, we are able to examine the local distribution of water in zeolite pores using this method. We will discuss mathematical expressions and applications of the function in next chapters.

The free energy calculation is often used to evaluate which state of a system is more thermodynamically favourable (that is, lower free energy) by comparing two different states where the system sits in. Thus, water and ion transport across a zeolite pore can be quantitatively examined using this approach to compute the free energy difference between successive stages where a molecule is assumed to pass through. The computed free energy profile will give a good indicator of whether the transport is likely or unlikely to happen for each type of molecule.

In statistical mechanics, this problem can be solved by the potential of mean force (PMF) that is related to the probability that a part of the system takes on a configuration, $\boldsymbol{\xi}_1$ (Roux, 1995). That is $P(\boldsymbol{\xi}_1) = \int e^{-H(\mathbf{r},\mathbf{p})/k_BT}\, \delta(\boldsymbol{\xi} - \boldsymbol{\xi}_1)\, d\mathbf{r}d\mathbf{p} / \int e^{-H(\mathbf{r},\mathbf{p})/k_BT}\, d\mathbf{r}d\mathbf{p}$ where $H(\mathbf{r},\mathbf{p})$ is the total energy of the system as a function of coordinates and momentums of particles, k_B is the Boltzmann constant, and $\delta(\boldsymbol{\xi} - \boldsymbol{\xi}_1)$ is the Dirac delta function (Arfken et al., 2013). The PMF is then given by $\mathrm{PMF}(\boldsymbol{\xi}_1) = \mathrm{PMF}(\boldsymbol{\xi}_0) - k_BT \ln P(\boldsymbol{\xi}_1)/P(\boldsymbol{\xi}_0)$. $\boldsymbol{\xi}_0$ is a reference point and $\mathrm{PMF}(\boldsymbol{\xi}_0)$ can be set to zero as long as its absolute free energy is not required. It is difficult to measure this directly if some configurations are rarely observed. Therefore, an “umbrella sampling” or “stiff spring” method can be used to approximate this (Roux, 1995, Hermans and Lentz, 2014). In umbrella sampling, the desired configuration is sampled more intensively (so-called ‘high sampling’) than in the natural system by adding a biasing force, often using a harmonic potential. The position of the biasing force is moved along the reaction coordinate to sample different “windows”. The averages are then calculated with a re-weighting term for each window that counters the effects of the biasing in calculation of the PMF.

Alternatively, a “stiff spring” approach can be used, which tightly binds the system and each configuration. This is problematic if it perturbs the surroundings, but can be useful if the constraints are simple. We will discuss the mathematical background on and the methodology to apply this approach for a system with zeolite and bulk solution in Chapter 6.

3.2 Zeolites studied by MD simulations

The main purpose of using MD to simulate zeolites is to understand physical aspects of their properties which cannot be obtained directly from experiments. Also, results from MD simulations of new membrane candidates could be very helpful in designing and modelling new materials for future applications.

In nanoporous materials, zeolites are extensively studied experimentally for various applications (Rimer et al., 2014, Rodríguez-Calvo et al., 2014). Nevertheless, physical behaviour of molecules passing through zeolite pores has yet to be well understood.

To date, only a few types of zeolite have been studied, mainly for LTA-types (e.g. ZK-4, zeolite A) and MFI-types (e.g. silicalite-1, ZSM-5) (Lin and Murad, 2001, Leiggener et al., 2008, Hughes et al., 2011, Yang et al., 2007, Zhang et al., 2012, Turgman-Cohen et al., 2013). Among those studies, some work has focused on water dynamics, such as water diffusion in nanochannels and water adsorption by the zeolite to gain atomic-scale insights into correlation between water behaviour and the nanoporous materials (Hughes et al., 2011, Zhang et al., 2012, Yang et al., 2008, Turgman-Cohen et al., 2013). It is found that hydrophobic inner channels (e.g. all-silica LTA-type, silicalite-1) have a faster diffusion rate than their hydrophilic counterparts (e.g. zeolite A, ZSM-5). In addition, hydrophilic zeolites exhibit a larger water adsorptivity than the hydrophobic ones. It is also conclusive that the general trend of water transport through nanopores is that water flux becomes higher with increasing temperature, increasing pore size, and/or decreasing water loadings.

A number of studies have considered the dynamics of liquids passing through zeolite pores (Demontis et al., 2012, Arı et al., 2009, Demontis et al., 2010, Gabrieli et al., 2012, Demontis et al., 1995, Hughes et al., 2011, Fleys et al., 2004, Joshi et al., 2014). Arı *et al*. used MD simulations with the COMPASS force-field (Fleys et al., 2004) to investigate water dynamics for silicalite-1 (all-silica MFI-type) and Na-ZSM-5 (Si/Al = 95, 191 MFI-type) zeolites at different temperatures, 297, 354, and 393 K (Table 3-1) (Arı et al., 2009). This study suggested that diffusion rates are reduced as the fraction of aluminium is increased in the framework due to an ion-dipole interaction that inhibits water moving in Na-ZSM-5. The activation energy of water diffusion rises with decreasing Si/Al ratio, which implies MFIs with more Al require higher energy to move water. The water structure is highly ordered in silicalite-1 channels at low temperature, but is found to become less ordered with increasing temperature and decreasing Si/Al ratio. This is due to the H-bond interactions being less dominant.

Table 3-1 Diffusion coefficients (× 10^{-9} m^2 s^{-1}) of water molecules in silicalite-1 and ZSM-5 (Si/Al = 191 and 95) at 297, 354, and 393 K (Reproduced from Ref (Arı et al., 2009))

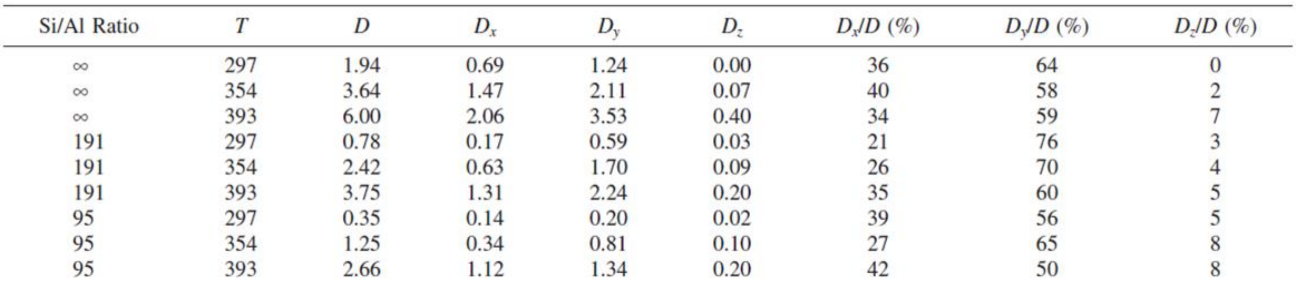

Si/Al Ratio	T	D	D_x	D_y	D_z	D_x/D (%)	D_y/D (%)	D_z/D (%)
∞	297	1.94	0.69	1.24	0.00	36	64	0
∞	354	3.64	1.47	2.11	0.07	40	58	2
∞	393	6.00	2.06	3.53	0.40	34	59	7
191	297	0.78	0.17	0.59	0.03	21	76	3
191	354	2.42	0.63	1.70	0.09	26	70	4
191	393	3.75	1.31	2.24	0.20	35	60	5
95	297	0.35	0.14	0.20	0.02	39	56	5
95	354	1.25	0.34	0.81	0.10	27	65	8
95	393	2.66	1.12	1.34	0.20	42	50	8

In addition, using MD techniques, Demontis *et al*. studied water behaviour when it is in zeolite Na A (Na:Si:Al = 1:1:1, LTA-type) and NaCa A (Ca:Na:Si:Al = 0.5:0.5:1.0:1.0, LTA-type) at different water loadings, 40, 120, and 200 molecules per unit cell (Figure 3-5) (Demontis et al., 2010). A unit cell is the simplest and smallest repeating unit in a 3-D crystal structure and often referred to in MD simulations. Water loading per unit cell means the number of water molecules residing in the crystal's unit cell, indicating the water number density. In the study, the authors calculated the activation energies to water transport, depending on the different loadings. They derived the activation energies by fitting the gradient of $\ln k$ versus $1/T$ from the Arrhenius equation, $\ln k = (-E_a/RT) + \ln A$, where T is the temperature, k is the rate constant, R is the universal gas constant, A is the frequency factor, E_a is the activation energy, and $D = k$ in this case where D is the water diffusion coefficient. The activation energy for water diffusion reduced to almost half of that for zeolite Na A when the water loading increased from 40 /u.c. to 120 /u.c., but the reverse happened when increasing from 120 /u.c. to 200 /u.c.. This is in semi-quantitative agreement with the results obtained by two experimental techniques, pulsed field gradient nuclear magnetic resonance (PFG NMR) and quasi-elastic neutron scattering (QENS). This trend implies that, with a range of water loadings 40 to 120 per unit cell, the interaction between water molecules and the charge-compensating cations (Na^+) becomes less important in governing water diffusion since the number of molecules not belonging to the first hydration shell is greater. Between water loadings of 120 /u.c. and 200 /u.c., however as the channels of zeolite Na A become more saturated with water, the activation energy increases. Unlike the Na A, for zeolite NaCa A, reliable data for activation energies with 40 molecules/u.c. was not obtained due to the very low diffusivity at the low loading of zeolite NaCa A channels, while the activation energy was increased when the loading increased from 120 /u.c. to 200 /u.c..

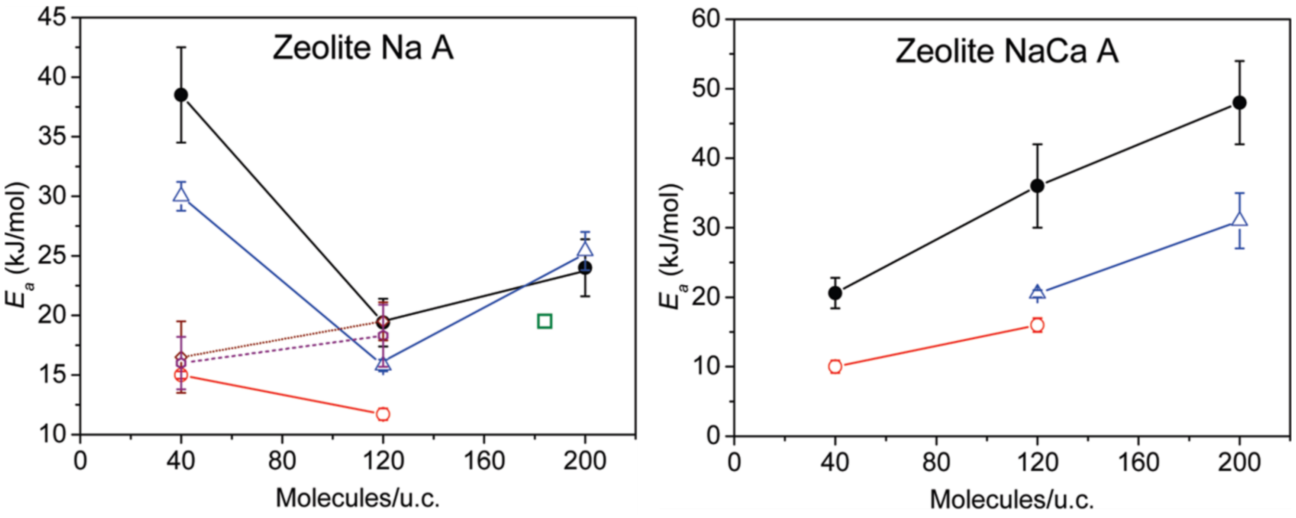

Figure 3-5 Activation energies to water diffusion as a function of water loading in zeolites: open triangles (blue line) from the work done in (Demontis et al., 2010); open diamonds (wine-coloured dotted line) from Ref (Wu et al., 2009); open hexagons (violet dashed line) from Ref (Wu et al., 2009); open circles (red line) from QENS experiments in Ref (Paoli et al., 2002); full circles (black line) from PFG NMR experiments in Ref (Paoli et al., 2002). [Reproduced from Ref (Demontis et al., 2010)]

In addition to aluminosilicate zeolites mentioned above, more recently aluminophosphate zeolites have been investigated using molecular dynamics methods (Demontis et al., 2012). This research studied the physical properties of water adsorbed in $AlPO_4$-5 (AFI-type) and SSZ-24 (all-silica AFI-type) at different temperatures and water loading. This MD study showed that water molecules adsorbed in pores of $AlPO_4$-5 form helicoidal chains running along the pore channel, which was also experimentally studied and verified (Floquet et al., 2004), whereas the simulations suggest that the structure of water molecules in SSZ-24 are linear chains along the channel axis. This structural difference is believed to stem from the smaller effective diameter of SSZ-24 than that of $AlPO_4$-5, and the Al-P alternation of $AlPO_4$-5. Figure 3-6 indicates distribution functions of water molecules projected on the zeolites' 2-D cross sections perpendicular to the channel axis. As mentioned earlier, distribution functions can be obtained by calculating the probability of a property as a function of some independent variable. Here the distribution functions represent the probabilities that water molecules sit at a particular position in the stationary zeolites. Thus, the figure shows the more dense lines, the higher probability of the presence of water, meaning that water molecules adopt different symmetries according to different water loading densities within $AlPO_4$-5 and SSZ-24, respectively. Notably in $AlPO_4$-5, hexagonal symmetry was found at the highest loading (108 molecules/simulation cell), and indicated the presence of the helicoidal water chains.

Demontis *et al*. found the diffusivities for both zeolites increased with decreasing water density and even overwhelmed that of bulk water at 24 loadings per individual zeolite box. The higher diffusivity for lower loadings can be explained by more available positions for water molecules to be in, that is an entropic effect. The energy barriers to diffusion are ca. 10 and 15 kJ mol^{-1} for SSZ-24 and $AlPO_4$-5, respectively, both are lower than that of the bulk (ca. 19 kJ mol^{-1}). This phenomenon could be attributed to the smaller number of H-bonds in each of the zeolites than in bulk, and the weaker H-bonds with the inner surfaces than the intermolecular H-bonds. Also, both types of zeolite have hydrophobic inner walls that may provide energetically-favourable environment for water diffusion. The difference in activation energies between two frameworks is largely due to the different atomic charges.

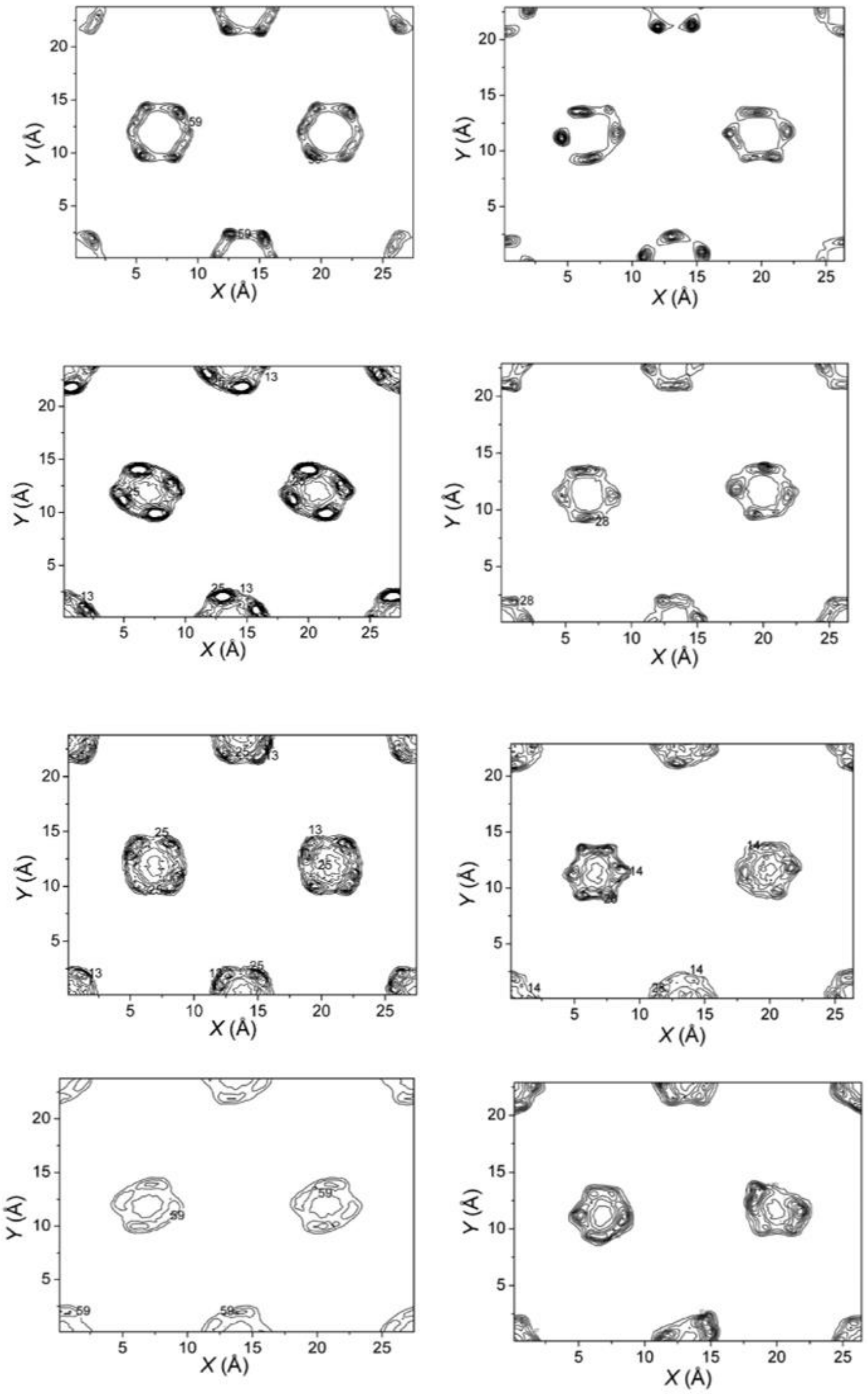

Figure 3-6 Distribution functions of water oxygens displayed on the cross sections of the zeolites at 300 K and at different loading. Left-sided projections (from top to down): $AlPO_4$-5 with 108, 72, 48, and 24 water molecules; right-sided projections (from top to down): SSZ-24 with 100, 72, 48, and 24 water molecules [Reproduced from Ref (Demontis et al., 2012)].

Hughes *et al*. have intensively studied materials for RO membranes in a broad range from conventional polyamide composites (Hughes and Gale, 2010, Hughes and Gale, 2012) to zeolites (Hughes et al., 2011) using MD techniques. They suggested four different zeolites as new types of

RO desalination membranes. The zeolites they focused on (pure silica MTF-, SFF-, VET-, GON-type) are 1-D channel frameworks (Figure 3-7) closely analogous to aligned nanotubes (Holt et al., 2006, Majumder et al., 2005) and thus may be expected to show a higher permeability than zeolites with two or more dimensional pores because the diffusion takes place in a single direction. Also, the systems were selected to have pores with a size that is expected to reject salt ions and let water smoothly pass through. The MD results showed that water diffuses through the zeolites at a faster rate than that of the polymer composite membranes commercially used. In addition, free energy perturbation calculations (Truhlar, 2008) were performed, which calculated the free energy difference (ΔA) between two states by $\Delta A = -k_B T \ln\langle \exp[-\Delta U / k_B T] \rangle_0$ where ΔU is the potential energy difference between the two states, k_B is the Boltzmann constant, and $<\ldots>_0$ is the ensemble average over sample configurations at state 0. At this point, the two states 0 and 1 mean 'before' and 'after' a chemical reaction and/or configurational change. Using this method, in the study, it was possible to determine how thermodynamically favourable ions of interest find the zeolite pores compared to when the ions in bulk solution. It was revealed that all four zeolite membranes studied here have a high free energy difference between Cl^- ions inside and outside the pore. Assuming Na^+ to enter the pore, extra energy penalty will be required to break the charge balance with its counter ion, Cl^- due to the charge separation. Consequently, the zeolites are considered to reject the main salt from the bulk solution.

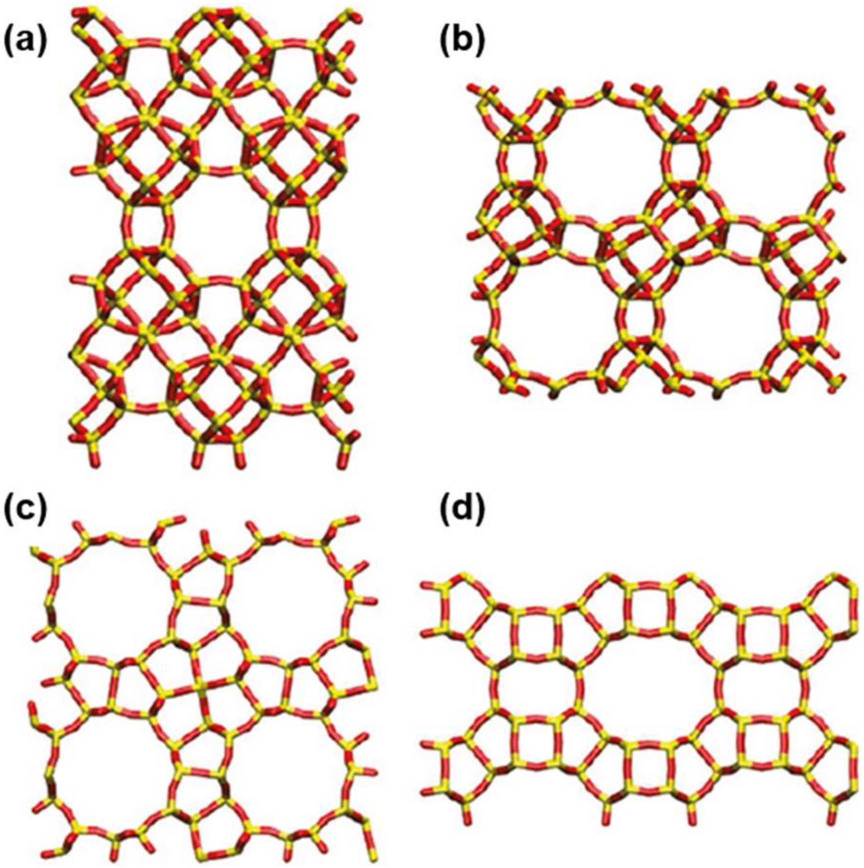

Figure 3-7 1-D pore zeolites as viewed along the 1-D channel: (**a**) MTF, (**b**) SFF, (**c**) VET, and (**d**) GON. Silicon and oxygen atoms are coloured in yellow and red, respectively [Reproduced from Ref (Hughes et al., 2011)].

From the results of studies on water diffusion in nanochannels, in general, it may be concluded that diffusion is improved for increasing temperature, decreasing water loadings, and weaker charge attractions between the channel walls and fluid. However, Al-containing zeolites such as ZSM-5, zeolite A, and $AlPO_4$-5 exhibit enhanced water adsorptivities in relation to pure silica zeolites since their hydrophilicity is improved due to the electrical charges. This tendency stems from the fact that the hydrophilic character offers a larger number of non-bonding interactions with water molecules.

3.3 MD studies on water and ion transport through various membranes

Some work has been done with MD simulations to examine water and/or ion transport during the RO process. One study by Cohen-Tanugi and Grossman explored the RO performance of nanoporous graphenes as a function of pore size, pore chemistry, and applied pressure (Cohen-Tanugi and Grossman, 2012). Their MD data indicated that the salt rejection performance strongly depends on having a pore diameter that is adequate to allow water permeation while hindering ions. The water flux of such membranes is generally several orders of magnitude higher than existing polymeric membranes. In addition, it was observed that the chemistry of the graphene pores notably influences the water flux. OH-functionalised pores were shown to have roughly double the water permeability due to their hydrophilic surface nature compared to the H-functionalised hydrophobic pores. In this ultrathin membrane, the variation in water flux may arise from the different behaviour of water molecules around the pores. The hydroxyl groups broaden the pore effective area available to water molecules than the hydrogen-functionalised groups due to the water affinity to the OH groups. In addition, the water molecules make a greater number of configurations by the additional hydrogen-bonding from the –OH groups. Unfortunately, the increase in water flux is accompanied by lower ion rejection, due to the substituting ability of the pore –OH groups for water molecules in the hydration shell of the ions that permeate the pore more easily by being dehydrated and re-hydrated with the hydroxyl groups.

Other works related to membranes have attempted to scrutinise ion transport in confined model cylindrical pores with effective radius ranging from 2.5 to 6.5 Å (Richards et al., 2012b, Richards et al., 2012a). For example, the purpose of the work done by Richards *et al.* is to gain a deep understanding about correlations between anion transport and the effective radii of nanopores (Richards et al., 2012a, Richards et al., 2012b). Energy barriers to ion permeation through the pores were observed to depend heavily on pore size and ion properties. To investigate a variation in the free energy for each anion passing across the pore, they carried out a potential of mean force (PMF) calculation using umbrella sampling (Roux, 1995, Hermans and Lentz, 2014). PMF gives the free energy profile along a trajectory path. The free energy variation is given by 'work' done on a system in a reversible equilibrium process, thus is equal to the integral of a force exerted over the trajectory. This trajectory is often called 'reaction coordinate **r**'. As mentioned earlier, the free energy (*A*) can be defined with the canonical partition function for a system, therefore given as $A = -k_B T \ln\{\int \exp[-H(\mathbf{r},\mathbf{p})/k_B T]\, d\mathbf{r}\, d\mathbf{p}\}$ (Roux, 1995).

The computed free energy change for ion transport through a pore where the ion can fit with its full primary hydration shell are small compared to when the ion in bulk water since the ion is only required to rearrange its inner shell and/or to displace the secondary hydration shells. The free energy barrier in a pore with sizes between the bare ion and hydrated ion are relatively high due to the need for partial dehydration of the ion. When the pore is too small for bare ions to fit, energy barriers in this pore become very large. The general ordering of energy barriers for the hydrated anions is $F^- > Cl^- > NO_2^- > NO_3^-$ at the range of pore radii from 3.3 to 6.5 Å.

Some studies have been performed on water and ion transport through zeolite membranes in terms of free energy calculations which play a critical role to evaluate the performance as a desalination membrane (Hughes et al., 2011). Hughes *et al*. used the thermodynamic perturbation or the free energy perturbation (FEP) method (Chipot and Pohorille, 2007), to determine the free energy difference between NaCl ions in bulk water and the zeolites, for identifying the thermodynamically favourable region for the salt ions in the desalination membrane system The study (Hughes et al., 2011) showed hydrated Cl^- ions are highly unlikely to enter the zeolite membrane from the bulk solution, while hydrated Na^+ ions might be easier to penetrate it according to the FEP calculations. However, as long as the counter ions (Cl^-) seldom enters the zeolite channel at the same time when the sodium ions moves into it, it would be unlikely for the hydrated Na^+ to enter the pore. It is believed that an additional energy must be taken into account to break the charge balance between sodium cations and chloride anions due to the charge separation.

More work on water and ions behaviour with zeolite membranes have to be carried out using the free energy calculations in order to find and assess a new class of zeolites for desalination membranes. In addition to the umbrella sampling and FEP, the stiff spring method has been often used as a PMF approximation. This method is based on the fact that differentiation of the free energy with respect to a specified coordinate $\mathbf{r}$ is equal to minus the ensemble average of the force applied on a target molecule at the fixed configuration. Thus, a number of continuous simulations at equally quantified $\mathbf{r}$ generates the mean values of the force, then can be integrated to obtain the free energy profile for the molecule passing along the full trajectory. In this thesis, therefore, we will carry out free energy studies using the stiff spring approach on water or ion penetration into widely-used and potential zeolite membranes. All those details about theoretical background, method, and discussion will be dealt with in Chapter 6.

3.4 Summary and conclusions

Molecular dynamics (MD) simulation is one of the most useful and widely-used tools to achieve such purpose of studies since it helps investigators to access molecular-level physical properties of materials, and predict the properties of macroscopic materials.

Computational methods have been adopted and utilised to investigate several types of zeolite for their suitability as desalination membrane. MD techniques have been also used to explore ion transport in nanopores by quantifying energy barriers to ion permeation into the pore and examining the desalination performance of membranes with different pore diameters and different chemistries.

This project will explore the following aspects: gaining a deeper insight into water and ion transport through zeolite membranes in a desalination system; identifying a new class of zeolitic materials which have a high potential as a desalination membrane; understanding the influences of variations in zeolite topology and pore size upon water behaviour and ion rejection performance; predicting and suggesting the better zeolites in terms of desalination.

First we will validate our MD approach by studying zeolites that have previously been investigated theoretically and/or experimentally. This will entail established force-fields which were used for these or similar type of zeolite in literature and the MD simulations will be carried out under the same condition as written in the literature and different ensemble methods (e.g. NVE, NVT, NPT) for comparison. The second part of the work is to explore a new class of zeolites that have a high potential to be used for desalination by employing reliable MD force-fields which already exist. We will then build models of these materials and study water diffusion within them. These simulation results may predict promising zeolites that could be useful as a future desalination membrane. The final step for this project is to examine the potential of mean force for water and ion movement through the membranes from bulk solution. This approach will help us determine whether or not Na^+ and Cl^- are likely to be rejected, and also the structural properties of the pores that lead to enhanced diffusion.

To achieve all these membrane performance of the target zeolites, diffusivities of water and/or water and ions in a periodic pore will be calculated.

References

ALLEN, M. P. 2004. Introduction to molecular dynamics simulation. *In:* ATTIG, N., BINDER, K., GRUBMÜLLER, H. & KREMER, K. (eds.) *Computational soft matter: from synthetic polymers to proteins.* Jülich: John von Neumann Institute for Computing, NIC-Directors.

ALLEN, M. P. & TILDESLEY, D. J. 1987. *Computer Simulation of Liquids,* New York, Oxford University Press, Oxford.

ANDERSEN, H. C. 1980. Molecular dynamics simulations at constant pressure and/or temperature. *The Journal of Chemical Physics,* 72**,** 2384-2393.

ARFKEN, G. B., WEBER, H. J. & HARRIS, F. E. 2013. Chapter 23 - Probability and Statistics. *Mathematical Methods for Physicists.* 7th ed. Boston: Academic Press.

Arı, M. U., AHUNBAY, M. G., YURTSEVER, M. & ERDEM-ŞENATALAR, A. 2009. Molecular Dynamics Simulation of Water Diffusion in MFI-Type Zeolites. *Journal of Physical Chemistry B,* 113**,** 8073-8079.

CEYHAN, T., TATLIER, M. & AKÇAKAYA, H. 2007. In vitro evaluation of the use of zeolites as biomaterials: effects on simulated body fluid and two types of cells. *Journal of Materials Science: Materials in Medicine,* 18**,** 1557-1562.

CHIPOT, C. & POHORILLE, A. 2007. Calculating Free Energy Differences Using Perturbation Theory. *In:* CHIPOT, C. & POHORILLE, A. (eds.) *Free Energy Calculations.* Springer Berlin Heidelberg.

COHEN-TANUGI, D. & GROSSMAN, J. C. 2012. Water Desalination across Nanoporous Graphene. *Nano Letters,* 12**,** 3602-3608.

DEMONTIS, P., GULÍN-GONZÁLEZ, J., JOBIC, H. & SUFFRITTI, G. B. 2010. Diffusion of Water in Zeolites Na A and NaCa A: A Molecular Dynamics Simulation Study. *The Journal of Physical Chemistry C,* 114**,** 18612-18621.

DEMONTIS, P., GULÍN-GONZÁLEZ, J. & SUFFRITTI, G. B. 2012. Water Adsorbed in $AlPO_4$-5 and SSZ-24 Studied by Molecular Dynamics Simulation. *The Journal of Physical Chemistry C,* 116**,** 11100-11109.

DEMONTIS, P., SUFFRITTI, G. B., BORDIGA, S. & BUZZONI, R. 1995. Atom pair potential for molecular dynamics simulations of structural and dynamical properties of aluminosilicates:

test on silicalite and anhydrous Na-A and Ca-A zeolites and comparison with experimental data. *Journal of the Chemical Society, Faraday Transactions,* 91**,** 525-533.

EBRO, H., KIM, Y. M. & KIM, J. H. 2013. Molecular dynamics simulations in membrane-based water treatment processes: A systematic overview. *Journal of Membrane Science,* 438**,** 112-125.

ESSMANN, U., PERERA, L., BERKOWITZ, M. L., DARDEN, T., LEE, H. & PEDERSEN, L. G. 1995. A smooth particle mesh Ewald method. *The Journal of Chemical Physics,* 103**,** 8577-8593.

FLEYS, M., THOMPSON, R. W. & MACDONALD, J. C. 2004. Comparison of the Behavior of Water in Silicalite and Dealuminated Zeolite Y at Different Temperatures by Molecular Dynamic Simulations. *The Journal of Physical Chemistry B,* 108**,** 12197-12203.

FLOQUET, N., COULOMB, J. P., DUFAU, N. & ANDRE, G. 2004. Structure and Dynamics of Confined Water in $AlPO_4$-5 Zeolite. *The Journal of Physical Chemistry B,* 108**,** 13107-13115.

GABRIELI, A., SANT, M., DEMONTIS, P. & SUFFRITTI, G. B. 2012. Development and Optimization of a New Force Field for Flexible Aluminosilicates, Enabling Fast Molecular Dynamics Simulations on Parallel Architectures. *The Journal of Physical Chemistry C,* 117**,** 503-509.

GASCON, J., KAPTEIJN, F., ZORNOZA, B., SEBASTIAN, V., CASADO, C. & CORONAS, J. 2012. Practical Approach to Zeolitic Membranes and Coatings: State of the Art, Opportunities, Barriers, and Future Perspectives. *Chemistry of Materials,* 24**,** 2829-2844.

GOLDSTEIN, H. 1980. *Classical Mechanics,* Reading, Massachusetts, Addison Wesley.

GUBBINS, K. E., LIU, Y.-C., MOORE, J. D. & PALMER, J. C. 2011. The role of molecular modeling in confined systems: impact and prospects. *Physical Chemistry Chemical Physics,* 13**,** 58-85.

HAILE, J. M. 1992. Molecular Dynamics Simulation: Elementary Methods. *John Wiley & Sons, Inc., Canada*.

HERMANS, J. & LENTZ, B. 2014. Appendix D - Methods to compute a potential of mean force. *Equilibria and Kinetics of Biological Macromolecules.* 1st ed.: Wiley & Sons, Inc. John.

HOCKNEY, R. W. & EASTWOOD, J. W. 1988a. *Computer simulation using particles,* Bristol and New York, CRC Press.

HOCKNEY, R. W. & EASTWOOD, J. W. 1988b. Particle-Particle-Particle-Mesh (P3M) Algorithms. *Computer simulation using particles.* CRC Press.

HOLT, J. K., PARK, H. G., WANG, Y. M., STADERMANN, M., ARTYUKHIN, A. B., GRIGOROPOULOS, C. P., NOY, A. & BAKAJIN, O. 2006. Fast mass transport through sub-2-nanometer carbon nanotubes. *Science,* 312**,** 1034-1037.

HOOVER, W. G. 1985. Canonical dynamics: Equilibrium phase-space distributions. *Physical Review A,* 31**,** 1695-1697.

HUGHES, Z. E., CARRINGTON, L. A., RAITERI, P. & GALE, J. D. 2011. A Computational Investigation into the Suitability of Purely Siliceous Zeolites as Reverse Osmosis Membranes. *The Journal of Physical Chemistry C,* 115**,** 4063-4075.

HUGHES, Z. E. & GALE, J. D. 2010. A computational investigation of the properties of a reverse osmosis membrane. *Journal of Materials Chemistry,* 20**,** 7788-7799.

HUGHES, Z. E. & GALE, J. D. 2012. Molecular dynamics simulations of the interactions of potential foulant molecules and a reverse osmosis membrane. *Journal of Materials Chemistry,* 22**,** 175-184.

JACKSON, J. D. 1999. *Classical Electrodynamics*, Wiley.

JENSEN, F. 2007. *Introduction to Computational Chemistry,* UK, Wiley.

JIANG, J. W., BABARAO, R. & HU, Z. Q. 2011. Molecular simulations for energy, environmental and pharmaceutical applications of nanoporous materials: from zeolites, metal-organic frameworks to protein crystals. *Chemical Society Reviews,* 40**,** 3599-3612.

JORGENSEN, W. L., MADURA, J. D. & SWENSON, C. J. 1984. Optimized intermolecular potential functions for liquid hydrocarbons. *Journal of the American Chemical Society,* 106**,** 6638-6646.

JOSHI, K. L., PSOFOGIANNAKIS, G., VAN DUIN, A. C. T. & RAMAN, S. 2014. Reactive molecular simulations of protonation of water clusters and depletion of acidity in H-ZSM-5 zeolite. *Physical Chemistry Chemical Physics,* 16**,** 18433-18441.

KRISHNAN, T. V. S., BABU, J. S. & SATHIAN, S. P. 2013. A molecular dynamics study on the effect of thermostat selection on the physical behavior of water molecules inside single walled carbon nanotubes. *Journal of Molecular Liquids,* 188**,** 42-48.

LEIGGENER, C., CURRAO, A. & CALZAFERRI, G. 2008. Zeolite A and ZK-4. *In:* SCHUBERT, U., HÜSING, N. & LAINE, R. (eds.) *Materials Syntheses.* Springer Vienna.

LIN, J. & MURAD, S. 2001. A computer simulation study of the separation of aqueous solutions using thin zeolite membranes. *Molecular Physics,* 99**,** 1175-1181.

MAJUMDER, M., CHOPRA, N., ANDREWS, R. & HINDS, B. J. 2005. Nanoscale hydrodynamics: Enhanced flow in carbon nanotubes (vol 438, pg 44, 2005). *Nature,* 438**,** 930-930.

MAYO, S. L., OLAFSON, B. D. & GODDARD, W. A. 1990. DREIDING: a generic force field for molecular simulations. *The Journal of Physical Chemistry,* 94**,** 8897-8909.

MELLER, J. 2001. Molecular Dynamics. *eLS.* John Wiley & Sons, Ltd.

NASRABADI, A. T. & FOROUTAN, M. 2011. Ion-separation and water-purification using single-walled carbon nanotube electrodes. *Desalination,* 277**,** 236-243.

PAOLI, H., METHIVIER, A., JOBIC, H., KRAUSE, C., PFEIFER, H., STALLMACH, F. & KARGER, J. 2002. Comparative QENS and PFG NMR diffusion studies of water in zeolite NaCaA. *Microporous and Mesoporous Materials,* 55**,** 147-158.

RICHARDS, L. A., SCHAEFER, A. I., RICHARDS, B. S. & CORRY, B. 2012a. The Importance of Dehydration in Determining Ion Transport in Narrow Pores. *Small,* 8**,** 1701-1709.

RICHARDS, L. A., SCHAEFER, A. I., RICHARDS, B. S. & CORRY, B. 2012b. Quantifying barriers to monovalent anion transport in narrow non-polar pores. *Physical Chemistry Chemical Physics,* 14**,** 11633-11638.

RIMER, J. D., KUMAR, M., LI, R., LUPULESCU, A. I. & OLEKSIAK, M. D. 2014. Tailoring the physicochemical properties of zeolite catalysts. *Catalysis Science & Technology,* 4**,** 3762-3771.

RODRÍGUEZ-CALVO, A., SILVA-CASTRO, G. A., OSORIO, F., GONZÁLEZ-LÓPEZ, J. & CALVO, C. 2014. Novel Membrane Materials for Reverse Osmosis Desalination. *Hydrology: Current Research,* 5.

ROUX, B. 1995. The calculation of the potential of mean force using computer simulations. *Computer Physics Communications,* 91**,** 275-282.

RYCKAERT, J.-P., CICCOTTI, G. & BERENDSEN, H. J. C. 1977. Numerical integration of the cartesian equations of motion of a system with constraints: molecular dynamics of n-alkanes. *Journal of Computational Physics,* 23**,** 327-341.

SCHLICK, T. 2002. Molecular modeling and simulation: an interdisciplinary guide. *Springer-Verlag New York Inc., New York.*

SMITH, W., FORESTER, T. R. & TODOROV, I. T. 2012. The DL_POLY Classic User Manual. *STFC Daresbury Laboratory, UK*.

SMITH, W. F. & HASHEMI, J. 2009. *Foundations of Materials Science and Engineering,* London, UK, McGraw-Hill.

TOUKMAJI, A. Y. & BOARD, J. A. 1996. Ewald summation techniques in perspective: a survey. *Computer Physics Communications,* 95**,** 73-92.

TRUHLAR, D. G. 2008. Chipot, C., Pohorille, A., Eds. Free Energy Calculations: Theory and Applications in Chemistry and Biology. *Theoretical Chemistry Accounts,* 121**,** 105-106.

TURGMAN-COHEN, S., ARAQUE, J. C., HOEK, E. M. V. & ESCOBEDO, F. A. 2013. Molecular Dynamics of Equilibrium and Pressure-Driven Transport Properties of Water through LTA-Type Zeolites. *Langmuir,* 29**,** 12389-12399.

VAN GUNSTEREN, W. F. & BERENDSEN, H. J. C. 1987. Groningen Molecular Simulation (GROMOS) Library Manual. *BIOMOS, The Netherlands*.

VERLET, L. 1967. Computer "Experiments" on Classical Fluids. I. Thermodynamical Properties of Lennard-Jones Molecules. *Physical Review,* 159**,** 98-103.

VERLET, L. 1968. Computer "Experiments" on Classical Fluids. II. Equilibrium Correlation Functions. *Physical Review,* 165**,** 201-214.

WEINER, S. J., KOLLMAN, P. A., NGUYEN, D. T. & CASE, D. A. 1986. An all atom force field for simulations of proteins and nucleic acids. *Journal of Computational Chemistry,* 7**,** 230-252.

WU, J. Y., LIU, Q. L., XIONG, Y., ZHU, A. M. & CHEN, Y. 2009. Molecular Simulation of Water/Alcohol Mixtures' Adsorption and Diffusion in Zeolite 4A Membranes. *Journal of Physical Chemistry B,* 113**,** 4267-4274.

YANG, J. Z., CHEN, Y., ZHU, A. M., LIU, Q. L. & WU, J. Y. 2008. Analyzing diffusion behaviors of methanol/water through MFI membranes by molecular simulation. *Journal of Membrane Science,* 318**,** 327-333.

YANG, J. Z., LIU, Q. L. & WANG, H. T. 2007. Analyzing adsorption and diffusion behaviors of ethanol/water through silicalite membranes by molecular simulation. *Journal of Membrane Science,* 291**,** 1-9.

YONG, X. & ZHANG, L. T. 2013. Thermostats and thermostat strategies for molecular dynamics simulations of nanofluidics. *The Journal of Chemical Physics,* 138**,** 084503.

ZHANG, K., LIVELY, R. P., NOEL, J. D., DOSE, M. E., MCCOOL, B. A., CHANCE, R. R. & KOROS, W. J. 2012. Adsorption of Water and Ethanol in MFI-Type Zeolites. *Langmuir*, 28**,** 8664-8673.

Chapter 4 Water diffusion in zeolites: Molecular dynamics studies on effects of water loading and thermostat

4.1 Abstract

Molecular dynamics simulations were employed to investigate diffusion and structural properties of water molecules confined in one-dimensional zeolites. Several water loadings and thermostatting methods were used, and insight into the effects of these was obtained by comparing diffusion and structural properties. Water diffusion was characterised via mean square displacements (self and collective diffusivities) and radial distribution functions enabled the structural ordering of water for different pore sizes and loadings to be compared. Interestingly at lower loadings, molecules tend to form clusters and move collectively, while at higher loadings, the self-diffusion coefficient in the pores is similar to that in bulk water. The length of the simulation cell was varied to determine the system size effects on the results, and narrow pores were also investigated in order to examine how this affected the effectiveness of water transport through the zeolite.

4.2 Introduction

Zeolites and zeolite-like materials (e.g. metal organic frameworks) have attracted considerable attention over the last few decades due to their versatile industrial applications as materials for catalysis, absorption, and molecular sieving (Auerbach et al., 2003, Granda-Valdés et al., 2006). Their flexibility stems from the large range of nanoporous crystal structures (Baerlocher and McCusker, 2015, First et al., 2011, Gascon et al., 2012) that their chemistry allows them to form. In addition, their chemical composition and reactivity can be varied. Such materials have recently been employed as membrane materials (Drobek et al., 2012, Lee et al., 2011, Zhu et al., 2013, Duke et al., 2009, Li and Wang, 2010). We select zeolites that have pore sizes that are sufficiently small that small ions and molecules are expected to be excluded from the pores due to a molecular sieving effect, and focus on the diffusion coefficients of water in these materials.

Molecular dynamics (MD) simulations have proven to be a reliable method to characterise the kinetics, dynamics and thermodynamics of nanostructures at the molecular scale, enabling the probing of time and length scales which are previously difficult to access experimentally. The possibility of mimicking the behaviour of atomic and molecular clusters can therefore help to predict and successively fine tune better materials for specific applications. With the advancement of computing performance, MD simulations can be employed for bigger and more complex structures e.g. water transport across zeolitic systems (Lin and Murad, 2001, Hughes et al., 2011, Liu and Chen, 2013).

Carbon nanotubes (CNTs) and porous graphene are alternative membrane materials that possess well-defined pores; the pore size can be under 1 nm, which is molecular sieving to small ions and molecules (Wang et al., 2013, Cohen-Tanugi and Grossman, 2014, Holt et al., 2006). Both materials exhibit exceptional water flow rates through the pores due to the fact that the hydrophobicity as well as straightness of the pores provide water molecules inside with “hyperlubricity” (Alexiadis and Kassinos, 2008, Holt et al., 2006, Cohen-Tanugi and Grossman, 2012). However, from an experimental point of view, making such small and well-defined pores is very difficult to achieve. Techniques for formation of uniform pore size and high pore density materials are still far from being commercially viable for membranes (Liu and Chen, 2013). In contrast, zeolites naturally exist as well-defined crystalline structures and the pores are well packed, giving a high pore density. Due to this practical advantage, zeolites that have well-defined one-dimensional (1-D) pores of sub-nanometre diameter are proposed to have high potential as membrane materials. This work thus studies on 1-D zeolite based membranes.

Both experimental and simulation results have identified that water in hydrophobic and/or nanoporous structures forms clusters at some loadings (Ohba et al., 2005, Demontis et al., 2008, Iiyama et al., 2006). In computational simulations, water is easily filled up along the nanopores using either a manual or grand canonical Monte Carlo (GCMC) approach, while experiments can control the water loading in generally two ways: a pre-heating method and a pressure-induced infiltration. For the pre-heating method, the nanoporous structure/material is pre-heated in a vacuum condition, then cooled down with varying vapour pressure, resulting in varied amounts of water loading in the pore. The other method controls the water loading in nanostructures by compressing a water-nanostructure chamber at various loading rates.

Small-angle x-ray scattering (SAXS) experiments and GCMC studies have shown that water molecules begin to form clusters that are 6 Å in diameter at 0.6 relative pressure (P/P_0) within a 11 Å width slit-pore and the cluster size becomes bigger with increasing the pressure (higher water loading) due to combination of clusters (Ohba et al., 2005). Also, it has been found that water assemblies of 15 Å diameter are formed and the structure has ice-like order in slit-pores of 16.3 Å in width at $P/P_0 = 0.6$ using x-ray diffraction (XRD) measurements and reverse Monte Carlo simulations (Iiyama et al., 2006). Recently, some interesting studies have been carried out for slit-pores of different widths (7 and 11 Å) and at different pressures (P/P_0), revealing that the kinetics of water assembly is dominantly influenced by the pore width at low pressure (under $P/P_0 = 0.5$) and water adsorption rate is faster for the narrower pores at just above the critical pressure (0.4 for 7 Å width and 0.6 for 11 Å) (Ohba and Kaneko, 2009). In addition, cage-like pores (LTA-type zeolite) can also hold water clusters: α-cages with 10 Å diameter have 24 molecules in a cluster, whereas β-cages with 6 Å have 4 molecules (Demontis et al., 2008). Despite these efforts, understanding water behaviour in nanopores is still far from complete.

As we expect water clustering to have a significant impact on water diffusivity and in particular on the transport diffusion coefficient, in this work we will examine structural and dynamical properties of zeolite-confined water in relation to cluster size and stability. In previous work (Bussai et al., 2002, Zhang et al., 2009, Arı et al., 2009, Hughes et al., 2011), water diffusivity in zeolites has been studied by considering self-diffusion coefficients, which quantify the rate of diffusion of a single molecule within a fluid in equilibrium, and the simulation results have been validated by comparison with experiment. In the present work, collective diffusion coefficients, which quantify the flow of molecules, were also calculated since the fluid flux is related to the collective diffusivity and is therefore important for assessing the suitability of zeolites as a membrane. At very low densities, the self-diffusion and per-molecule collective diffusion coefficients become equal, but with the higher water loadings we are considering, this is not the case.

In order that MD simulations resemble experimental conditions, temperature control algorithms, so-called thermostats, are often used. Thermostats can be classified into two major categories: stochastic thermostats, which include Andersen and Langevin (LGV) thermostats; and deterministic thermostats, which include Gaussian, Berendsen, kinetic rescaling, and Nosé-Hoover (NH) thermostats. Of the deterministic thermostats, the Nosé-Hoover and Gaussian thermostats have been shown to generate the canonical (NVT) and isokinetic canonical ensemble (NVT-iso) respectively (Evans and Morriss, 2008), and are therefore widely used. In this work we will use a Nosé-Hoover thermostat, which gives good agreement with experimental results for molecular diffusion (Hünenberger, 2005, Basconi and Shirts, 2013), and compare the results obtained with those obtained using adiabatic (unthermostatted) simulations. Thermostats can be applied to the whole system or parts of it: in the case of zeolites they could be applied to the water, the zeolite or both. It has been found that unphysical behaviour can take place due to the misuse of thermostats, especially for heterogeneous systems such as water-absorbed in nanostructures and in nonequilibrium conditions, e.g. in the presence of flow. Often the streaming velocity rather than the peculiar velocity is thermostatted, and this can result in the thermostat doing work on the system (Bright et al., 2005).

A number of studies have compared the effects of thermostats on water diffusion when confined in porous materials. Krishnan *et al.* (Krishnan et al., 2013) reported their influence on pressure-driven water within carbon nanotubes. They compared NH, Berendsen and LGV thermostats, and found that the particular type of thermostat used can influence the behaviour of water confined in the smaller pores at lower temperatures (Krishnan et al., 2013). We have recently found that thermostatting the framework / walls of a confined fluid rather than the whole system or just the fluid inside it (e.g. keeping the walls rigid), has a significant effect on properties of fluids undergoing Couette flow (Bernardi et al., 2010). Yong and Zhang (Yong and Zhang, 2013) extended this work, comparing the effects of LGV, dissipative particle dynamics (DPD) and simulations with NH chain thermostats on Couette flow of Lennard-Jones particles, thermostatting walls and/or fluid and found that thermostatting the walls gave better agreement with experiments in terms of the fluid transport coefficients. A recent work on the diffusion rates of water through carbon nanotubes subject to pressure gradients showed discrepancies in the results obtained using different thermostatting methods (Thomas and Corry, 2014). All these studies show that when thermostatting is not carried out appropriately, for confined systems under flow, this can result in unphysical, and rather unpredictable, behaviour such as unusual thermal and kinetic conditions of flow (i.e. extreme temperature and rate) (Chi et al., 2014).

Differently to those studies, we will focus on determining diffusion coefficients using equilibrium simulations. Even in the absence of external fields or gradients, it has been observed that water can form clusters at low loadings that will flow in one direction for periods of time (Alberto, 2007). These clusters will therefore have a streaming component to their velocity that will change with time. It is therefore important to be sure that the thermostatting mechanism is not enhancing or diminishing this effect. For equilibrium simulations the results for uniformly thermostatted systems and unthermostatted systems should converge in the thermodynamic limit. This will be checked for the systems considered in this paper. As we are ultimately interested in studying flow under pressure gradients where thermostats are necessary to prevent the system from heating up (Hünenberger, 2005) it is important to check that at equilibrium the use of wall thermostats are effective for these systems.

The purpose of this study is to gain deeper insight into changes in confined fluid flow with different loadings. We will observe if clustering of the water occurs, and what affect that has on the diffusion of water. To ensure that the behaviour we are observing is not due to the thermostatting mechanism, we examine a number of different thermostats. These results will be of use in future studies of zeolitic systems as membrane candidates.

4.3 Background and methods

4.3.1 Water structure and transport properties

In this work, we consider the structure and transport of water in zeolite nanopores, and consider how these vary with loading and thermostatting mechanisms. As noted above, clustering of water in hydrophobic nanopores at moderate loading has been experimentally observed in (Ohba et al., 2005, Iiyama et al., 2006) by in situ SAXS and in situ XRD. In simulations, this effect can be qualitatively observed through direct visualisation of the water molecules within the pore, and can be quantitatively characterised by calculation of the radial distribution function $g(r)$ that for two particles of the same species is

$$g(r) = \frac{N_s(r)}{V_s(r)} \times \frac{1}{\rho} \tag{4-1}$$

where N_s is the number of particles in a spherical shell of radius between r and $r + dr$ and volume V_s, centred on a particle of interest, and ρ is the average particle number density for the whole system. This is most appropriate for study of spherically symmetric systems where it becomes equal to 1 when the particles are uniformly distributed. It can be measured experimentally by scattering spectroscopy. For the asymmetric systems considered here where the water molecules are confined to a pore, it is more useful to consider a function which is modified to account for the confinement $g(r)_{pore}$

$$g(r)_{pore} = g(r) \times \frac{V_s(r)}{V_{ps}(r)} \times \frac{\rho}{\rho_p} \approx g(r) \times \frac{V_s(r)}{2\pi {r_p}^2 dr} \times \frac{\rho}{\rho_p} \tag{4-2}$$

where V_{ps} represents the accessible volume of the pore shell between r and $r + dr$ (i.e. the portion of the spherical shell that is in the pore), ρ_p is defined as the particle number density of the pore and r_p

is the radius of the pore. Here we use the approximation that $V_{ps} \approx 2\pi r_p^2 dr$ which will be accurate at large r and overestimate $g(r)_{pore}$ at $r \approx r_p$, however since the accessible pore volume can only be estimated, this approximation is accepted. Use of $g(r)_{pore}$ is appropriate for the characterisation of density profiles in one dimensional pores and will have a value of 1 at all r if the particles are uniformly distributed in the pore.

Transport within a pore can be quantified through the self-diffusion coefficient D_s, and the collective diffusion coefficient D_c which is directly related to the transport diffusion coefficient (Gubbins et al., 2011). Self-diffusion represents the spontaneous mixing of particles among themselves, as such it is an indicator of molecular mobility. Experimentally, self-diffusivity can be determined by using pulsed field gradient nuclear magnetic resonance (PFG NMR) (Bussai et al., 2002) and quasielastic neutron scattering (QENS) measurements (Gubbins et al., 2011, Jobic et al., 1999), however from the self-diffusivity measurement, discrimination of collective motion, i.e. transport of nano-sized water droplet, is not possible. The collective diffusivity, which is more important parameter for evaluation of a zeolite as a potential membrane. The transport diffusivity is given by the ratio of the flux of molecules in the fluid due to a concentration gradient (Smith and Hashemi, 2009), ($J = -D_t \partial C/\partial z$ where J is the flux, D_t is the transport diffusion coefficient, C is the concentration, and z is the position), and is directly related to the collective diffusion coefficient through a thermodynamic factor (Gubbins et al., 2011) ($D_t = 1/(k_B T)\,(\partial\mu/\partial \ln C)_T D_c$ where μ is the chemical potential). Thus, the membrane performance in terms of flux can be evaluated by the collective diffusion coefficient. Transport/collective diffusivities in zeolites have been experimentally measured by QENS (Jobic et al., 1999) and by direct experimental measurements (Kapteijn et al., 1995).

The self-diffusion coefficient can be obtained by monitoring the mean square displacement (MSD) of each water molecule within the system, and if the motion is diffusive it will be given by the Einstein relationship

$$MSD(t) = \frac{1}{N}\lim_{t\to\infty}\left\langle \sum_{i=1}^{N} |\mathbf{r}_i(t) - \mathbf{r}_i(0)|^2 \right\rangle = 2dD_s t \qquad (4\text{-}3)$$

where $\mathbf{r}_i(t)$ is the position of the ith particle at time t, d is the system dimensionality and N is the number of molecules in the pore. The collective diffusion coefficient per molecule D_c' monitors the MSD of the centre-of-mass (com) of all the water molecules in a pore

$$MSD_{com}(t) = \frac{1}{M} \lim_{t\to\infty} \langle \sum_{j=1}^{M} \left| \mathbf{r}_{com,j}(t) - \mathbf{r}_{com,j}(0) \right|^2 \rangle = 2dD_c't \tag{4-4}$$

where M is the number of pores, $\mathbf{r}_{com,j} = 1/N \sum_{i=1}^{N} \mathbf{r}_i$ is the centre-of-mass of the N water molecules in the jth pore, and $D_c' = D_c/N$ represents the mean collective diffusion coefficient of individual molecule. In the limit of low density, or if the water moves as a cluster, D_s and D_c' will converge to the same value.

In the bulk (i.e. isotropic systems), each direction contributes equally to the diffusion coefficients:

$$D_x = D_y = D_z = D \tag{4-5}$$

where

$$2D_\alpha t = \frac{1}{N} \lim_{t\to\infty} \langle \sum_{i=1}^{N} \left| r_{\alpha,i}(t) - r_{\alpha,i}(0) \right|^2 \rangle, \quad \alpha = x, y, z \tag{4-6}$$

D_x, D_y, D_z represent diffusion coefficients in x, y, z direction, respectively, and D is a global diffusion coefficient.

In one-dimensional pores however, the water diffusion is constricted to a pore along the z-axis and the relationship between D and D_z changes

$$\frac{1}{3} D_z \cong D \tag{4-7}$$

4.3.2 Simulations algorithms

For our simulations we used an all-atom model and periodic boundary conditions (PBCs) in all directions. We consider a number of different molecular dynamics algorithms/ensembles: (i) constant volume and energy (NVE); (ii) constant volume with the temperature of the full system thermostatted (NVT); (iii) constant pressure with the temperature of the full system thermostatted (NPT); (iv) constant pressure and enthalpy (NPH); (v) constant volume with the temperature of the water thermostatted (NVT-w); (vi) constant volume with the temperature of the zeolite thermostatted (NVT-z). The simplest simulation approach is to carry out NVE simulations where the dynamics is simply Newtonian and the system samples a microcanonical distribution (Rapaport, 2004). All calculations were carried out using LAMMPS (Plimpton, 1995, Shinoda et al., 2004, Martyna et al., 1994).

Thermostatted dynamics is often used to generate a canonical distribution (NVT) and closely mimic experimental conditions. In this work this is achieved using a Nosé-Hoover chain thermostat (Thijssen, 2007), which links the system to multiple fictitious heat baths with the heat flowing in and out of the system in order to keep the average temperature at the target value. A damping parameter *Q*, determines the strength of the bath coupling. The value of *Q* will not change the ensemble, but it will affect the instantaneous rate of change of energies.

The pressure can also be controlled using a Nosé-Hoover barostat with a damping parameter, W_g, generating a NPH ensemble or an NPT ensemble when combined with a thermostat. As well as thermostatting the whole system, either the water or zeolite can be thermostatted. Thermostatting the zeolite only is particularly useful when simulating flow i.e. when it is important that the streaming velocity of the water is not misinterpreted as a contribution to the thermal energy.

The equations of motion for our system are

$$\dot{\mathbf{r}}_i = \frac{\mathbf{p}_i}{m_i} + \frac{\mathbf{p}_g}{W_g}\mathbf{r}_i$$

$$\dot{\mathbf{p}}_i = \mathbf{F}_i - \frac{\mathbf{p}_g}{W_g}\mathbf{p}_i - \frac{1}{N_f}\frac{\mathrm{Tr}[\mathbf{p}_g]}{W_g}\mathbf{p}_i - \frac{p_\xi}{Q}\mathbf{p}_i$$

$$\dot{\xi}_k = \frac{p_{\xi k}}{Q_k} \quad \text{for } k=1,\ldots,\mathrm{M}$$

$$\dot{p}_{\xi 1} = \sum_{i=1}^{N} \frac{\mathbf{p}_i^2}{m_i} + \frac{1}{W_g} \mathrm{Tr}\left[\mathbf{p}_g^t \mathbf{p}_g\right] - \left(N_f + d^2\right) kT_0 - p_{\xi 1} \frac{p_{\xi 2}}{Q_2}$$

$$\dot{p}_{\xi k} = \left(\frac{p_{\xi k-1}^2}{Q_{k-1}} - kT_0\right) - p_{\xi k} \frac{p_{\xi k+1}}{Q_{k+1}} \quad \text{for } k=2,\ldots,M-1$$

$$\dot{p}_{\xi M} = \left(\frac{p_{\xi M-1}^2}{Q_{M-1}} - kT_0\right) \tag{4-8}$$

where $\mathbf{r}_i$ represents the position of a given particle i having mass of m_i, $\mathbf{p}_i$ is the momentum of particle i and $\mathbf{F}_i$ denotes force exerted on the particle i. The term $\mathbf{p}_g$ is the modularly invariant form of the cell momenta (Martyna et al., 1994, Shinoda et al., 2004), ξ_k and $p_{\xi k}$ are the thermostat variable and its conjugated momentum of the kth thermostat, respectively. W_g and Q_k are the damping parameters of barostat and kth thermostat respectively, and control the oscillation frequency of the instantaneous pressure and temperature. N_f is the number of degrees of freedom and T_0 is the target temperature. There are several possible implementations of the Nosé-Hoover NPT equations, and this follows that used in LAMMPS (Plimpton, 1995, Shinoda et al., 2004, Martyna et al., 1994).

By considering the different molecular dynamics algorithms considered above, we will be able to check that the thermostatting mechanism does not influence the structure and dynamics of the water molecules in the zeolite pores.

4.3.3 Zeolite membrane construction and potential

Several MD simulations were carried out at different water loadings. We mostly focused on the VET framework as a membrane model which possesses cylindrical-like one dimensional channels with hydrophobic internal walls composed of Si and O only. All pores in the framework that are accessible to the water are approximately cylindrical and the accessible volume for water molecules is 78.2 Å^3/1000 Å^3. According to crystallographic data (Freyhardt et al., 1996, Baerlocher and McCusker, 2015), the effective diameter of the pore is 5.9 Å, and this is anticipated to be a useful material for applications such as water purification since pores of this size are expected to let water pass through while fully rejecting small ions and molecules including hydrated sodium and chloride ions. A unit cell of VET was taken from the crystallographic database (Baerlocher and McCusker, 2015), the unit cell size is 13.048 x 13.048 x 4.948 Å for *x*, *y*, *z* coordinates, respectively and the angles between all lattice vectors are 90°, it consists of 17 Si and 34 O atoms with a single 5.9 Å pore. In all the calculations we use a periodic simulation box with the pore aligned with the *z*-axis. The simulation box was composed of 2 x 2 crystallographic unit cells in the *x*, *y*-coordinates, and from 7 unit cells in the *z*-direction, making an initial cell size of 26.096 x 26.096 x 34.636 Å with 476 Si and 952 O (see Figure 4-1(a), (b)). In order to check the stability of the zeolite structure using the selected force field and to relax the structure at the desired temperature and pressure, an equilibration simulation run was carried out on the framework with constant pressure and temperature ensemble (NPT) at 300 K and 1 atm before placing water molecules inside.

In order to examine the effects of pore width on the results, the TON zeolite was also considered. This material has the same chemical composition but a smaller pore width (4.6 x 5.7 Å). Like VET, TON has 1-D channels, however the pores are slightly elliptic and the unit cell size is 13.859 x 17.420 x 5.038 Å for *x*, *y*, *z* coordinates, respectively, with the angles between all lattice vectors being 90°. The unit cell comprising 24 Si and 48 O atoms, was replicated to construct a 2 x 2 x 7 simulation box, with the *z*-axis aligned with the pore. The simulation size is 27.718 x 34.840 x 35.266 Å with 672 Si and 1344 O (see Figure 4-1(c), (d)). The accessible volume of the TON membrane is 80.4 Å^3/1000 Å^3. The TIP4P-Ew water model (Horn et al., 2004) was used, as it gives reasonable agreement with experimental data in terms of structure and diffusion rates (Cohen-Tanugi and Grossman, 2014, Horn et al., 2004, Horn et al., 2005) even though the model is unable to represent the intramolecular vibration of water. This model consists of three atoms (H, O, H) rigidly constrained and one massless charged particle that is 0.125 Å away from the oxygen in the direction of the centroid of the molecule. A Lennard-Jones (LJ) intermolecular interaction exists between the oxygen atoms

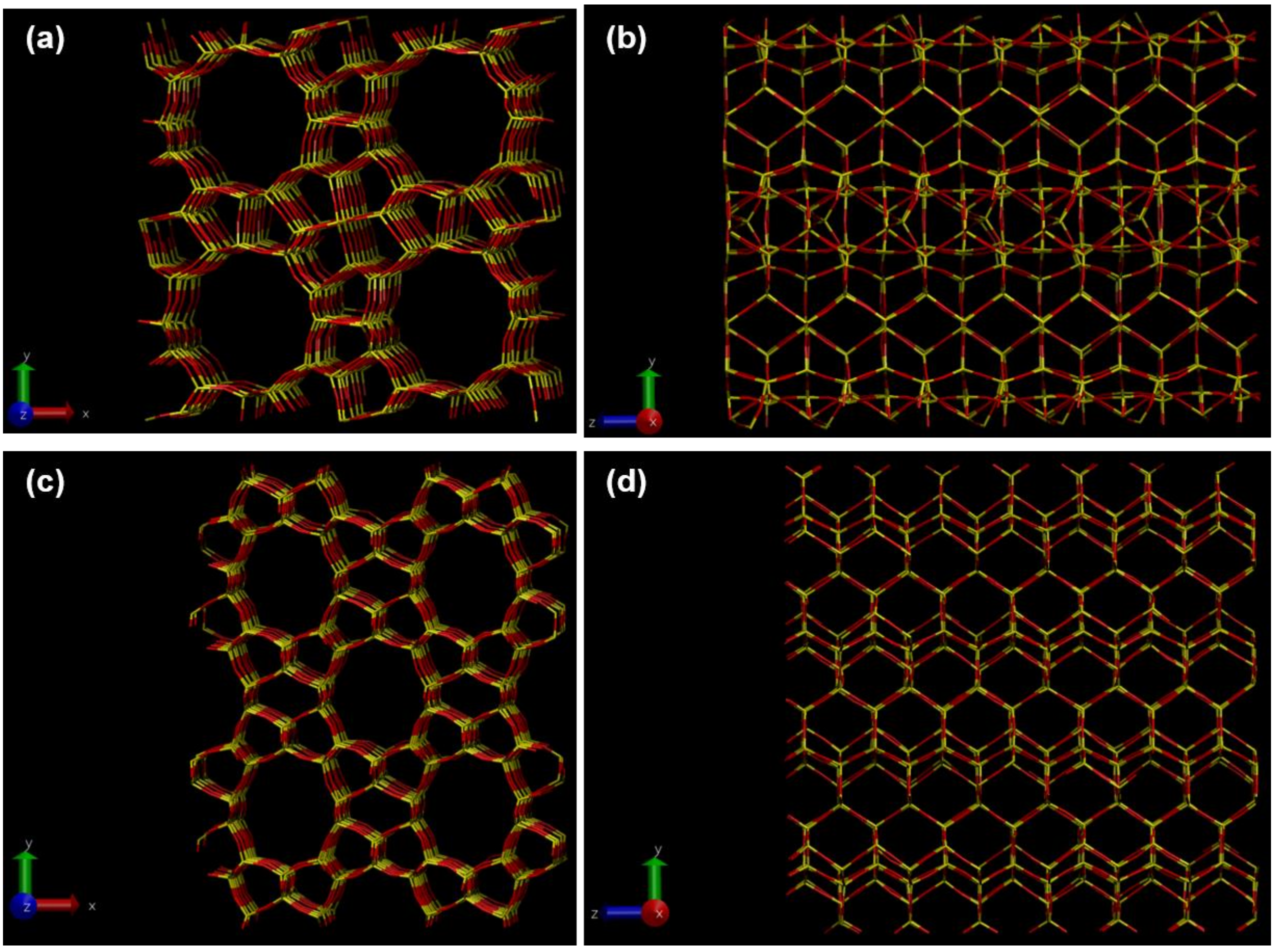

Figure 4-1 Simulation cells used for the two zeolites considered (zeolites represented by wires, oxygen coloured in red and silicon in yellow): VET views along the (a) *z*-axis (slightly distorted towards *x*-direction to better show the geometry of pores, the representations viewed in this direction were applied in the same manner in the rest of the chapter) and (b) *x*-axis; and TON views along the (c) *z*-axis; and (d) *x*-axis. *x*-, *y*-, *z*-directions of each zeolite cell are in periodic boundary condition.

$$U(r_{ij}) = 4\varepsilon\left[\left(\frac{\sigma}{r_{ij}}\right)^{12} - \left(\frac{\sigma}{r_{ij}}\right)^{6}\right] \tag{4-9}$$

where ε is the well depth of potential, r_{ij} is the distance between atoms, and σ is the distance at which the LJ energy is zero (Smit, 1992). In addition there is a Coulombic potential between charges on the hydrogen atoms and the massless particle. For interactions between the zeolite atoms and between zeolite-water interactions we used the Buckingham potential

$$U(r_{ij}) = A\,exp\left(-\frac{r_{ij}}{\rho}\right) - \frac{C}{r_{ij}^{6}} \tag{4-10}$$

where A, ρ, and C are constants (Jensen, 2007).

The three-body non-bonding interaction for the O-Si-O is given by

$$U(\theta_{jik}) = \frac{1}{2}k_{\theta}(\theta_{jik} - \theta_0)^2 \tag{4-11}$$

where k_θ is the force constant, θ_{jik} is the angle made by the three atoms, and θ_0 is the equilibrium angle.

Parameters for zeolite-zeolite interactions were derived by Hughes *et al.* (Hughes et al., 2011) who further developed the potential of Sanders *et al.* (Sanders et al., 1984). As the potential of Sanders *et al.* reproduced its zeolite structure well but the mechanical and electronic properties, the potential was refitted to first principle calculations values in order to match elastic constants and static dielectric constants of the zeolite. For water-zeolite interactions, we used parameters from experiments of de Leeuw and Parker (de Leeuw and Parker, 1998) for the interaction of α-quartz with water slightly adjusted by Hughes *et al.* in order to better match the binding energy obtained by quantum mechanical MP2 calculation.

4.3.4 MD simulations

The energy of the system (zeolite + water) was firstly minimised using the conjugate gradient algorithm, then equilibrated for 1 ns. A 2 ns simulation using a time step of 1 fs in isobaric-isothermal (NPT) ensemble followed to produce an equilibrated phase point. A NH barostat and thermostat with relaxation time of 1 ps (i.e. damping parameter of 1/ps) each were applied and variation in volume was monitored depending on the water loading, then the average volume for each case was employed for the constant volume simulations: NVE, NVT, NVT-z, NVT-w.

To model the long range Coulombic interactions, the particle-particle-particle mesh (PPPM) Ewald sum (Hockney and Eastwood, 1988b) was used. The SHAKE algorithm (Ryckaert et al., 1977) was used to constrain the geometry of the water molecule.

Ten independent runs were performed for each system considered. All the systems were re-minimised and equilibrated for 1 ns using a time step of 1 fs under NVT ensemble at 300 K before 2 ns production runs with different ensemble approaches were carried out: NVE, NVT, NVT-w, NVT-z, NPH, NPT.

Two different water loadings were considered: 6 and 32 water molecules per channel (7 unit cells long) for the VET zeolite for each of the thermostatting methods. Three longer channels were also considered for the smaller loading (i.e. 14, 21 and 28 unit cells with 12, 18 and 24 water molecules respectively). In addition the results for the TON zeolite with a loading of 6 water molecules per channel (7 unit cells long) were also considered. Due to the different unit cell sizes 6 water molecules in pores which are 7 unit cells correspond to different densities; using the available volumes given in (Baerlocher and McCusker, 2015), they would correspond to densities of 0.39 g cm^{-3} for VET and 0.52 g cm^{-3} for TON.

4.4 Results and discussion

4.4.1 Transport properties

We firstly considered water diffusion in the VET zeolite with simulation cells constructed with 7 unit cells in the z direction and two different water loadings, 6 and 32 water molecules/pore, which we refer to as VET6 and VET32 systems, respectively. Mean square displacement (MSD) measurements were performed to determine self-diffusion and per-particle collective transport coefficients given by equations (4-3) and (4-4), respectively, as well as their components in each direction. Theoretically, diffusion under confinement is divided mainly into three types of behaviour (Gubbins et al., 2011): one follows Fick’s law in which MSD of the fluid increases linearly with time, the second is a slower mode referred as the anomalous diffusion (Nguyen and Bhatia, 2012) not strictly following the Fickian behaviour, and the other is the single-file diffusion (Felderhof, 2009, Alexander and Pincus, 1978, Fedders, 1978) where the MSD is linearly proportional to the square root of time. The Fickian mechanism takes place when there are large enough pores for the guest molecules to pass each other, and when guest-guest and host-guest collisions allow movement in three-dimensions. Anomalous diffusion can occur due to confinement when fluid motion is restricted due to the channel shape. Single-file diffusion arises from the motion in pores that are small enough that the molecules cannot pass one another but the motion in one dimension unrestricted. This will occur in narrow, one-dimensional, smooth pores and can result in unusually high fluxes in narrow pores.

In this study, the water molecules diffusing through the zeolite channels are found to follow Fickian-like behaviour regardless of the ensemble and of the thermostatting mechanism employed. Linear relations for the MSD with time are obtained even though the pores are one-dimensional. This indicates that the pores are sufficiently wide that molecules can pass each other. It is also indicates that the pores are quite cylindrical with adsorption to all sites on the pore walls are of similar strength. The VET zeolite therefore resembles wide CNTs. As shown in Figure 4-2, water transport in *z* direction is the main component of the three-dimensional diffusion and displacement in *x*- and *y*-directions makes nearly no contribution to the MSD. In directions normal to the pore wall, the MSD increases linearly with time for a very short period (< 1 ps), until the complete restriction of motion in those directions occurs. Thus, the pores aligned one-dimensionally have both molecular and collective diffusion in one direction. The self and collective diffusion coefficients (D_{sz}, D'_{cz}) with different water loadings are summarised in Table 4-1.

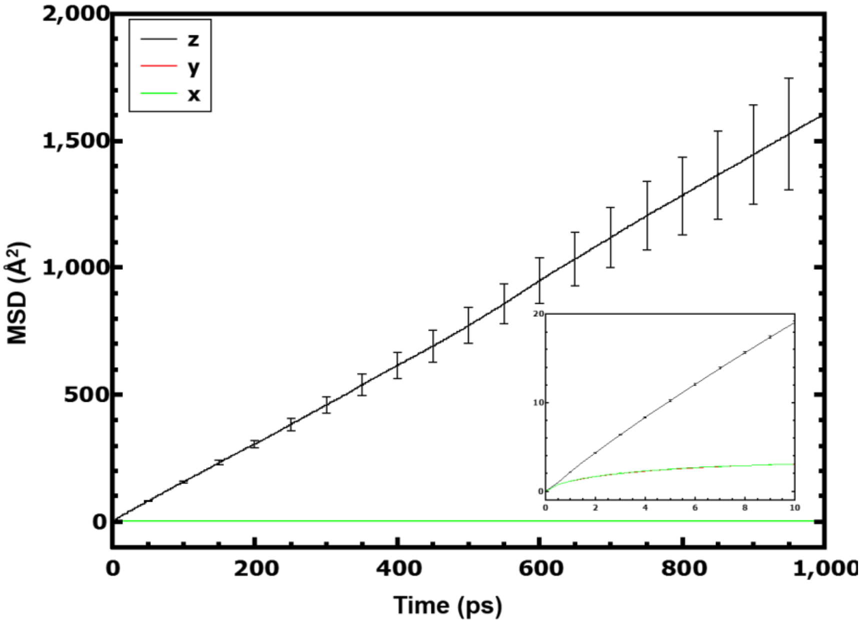

Figure 4-2 MSD of the water molecules in a VET zeolite. MSD for *x*, *y*, *z* directions (D_{sx}, D_{sy}, D_{sz}, respectively). The inset plot is a magnified MSD at 0 to 10 ps of this figure. *x* and *y* contributions to MSD were nearly identical, therefore they are indistinguishable as shown in the figure. The periodic simulation cell had 7 unit cells in the direction parallel to the pore, and 6 water molecules in each pore. The simulation was carried out in the NVT ensemble.

As shown in Table 4-1 and Figures 4-3 and 4-4, MSD data is insensitive to the way in which the system is thermostatted. When small numbers of particles are considered, it would be expected that there is some difference in the results obtained with different ensembles due to finite-size effects, however despite this, even unusual ensembles (NVT-w, NPH) give very similar results to other ensembles for water diffusing through the channel.

Table 4-1 *z*-component of the diffusion coefficients for water in zeolites

	VET6		VET32	
Ensemble	D_{sz}/ 10^{-9} m^2 s^{-1}	D'_{cz}/ 10^{-9} m^2 s^{-1}	D_{sz}/ 10^{-9} m^2 s^{-1}	D'_{cz}/ 10^{-9} m^2 s^{-1}
NVE	7.8 ± 1.2	6.9 ± 1.2	2.3 ± 0.1	0.5 ± 0.1
NVT	8.1 ± 1.2	7.2 ± 1.2	2.1 ± 0.1	0.5 ± 0.1
NVT-w	7.8 ± 0.9	7.2 ± 0.9	2.1 ± 0.1	0.5 ± 0.1
NVT-z	8.7 ± 1.2	8.1 ± 1.2	2.2 ± 0.1	0.5 ± 0.1
NPH	8.7 ± 1.2	8.1 ± 1.2	2.2 ± 0.1	0.5 ± 0.1
NPT	7.5 ± 0.6	6.6 ± 0.9	2.2 ± 0.1	0.4 ± 0.1

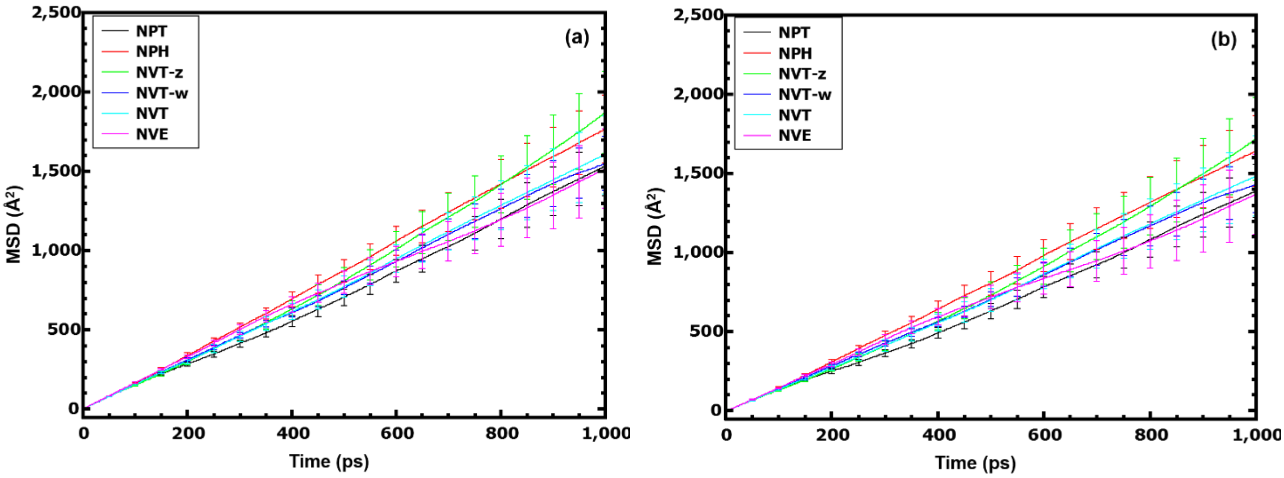

Figure 4-3 MSD of the (a) molecules of water and (b) centre-of-mass of the water in a VET zeolite. The periodic simulation cell had 7 unit cells in the direction parallel to the pore, and 6 water molecules in each pore. The simulations were carried out using various thermostatting mechanisms as indicated in the legend. The terms NVT-z and NVT-w refer to cases where only the zeolite or water was thermostatted, respectively.

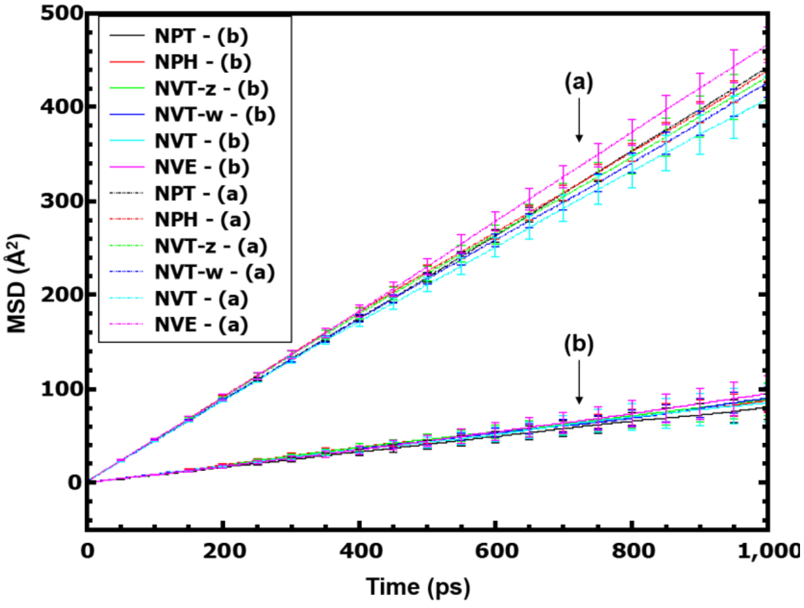

Figure 4-4 MSD of the (a) molecules of water and (b) centre-of-mass of the water in a VET zeolite. The periodic simulation cell had 7 unit cells in the direction parallel to the pore, and 32 water molecules in each pore. The simulation was carried out using various thermostatting mechanisms as indicated in the legend. The terms NVT-z and NVT-w refer to cases where only the zeolite or water was thermostatted, respectively.

For a loading of 6 water molecules/pore (VET6), very similar results were obtained for the molecular and com MSD, which is consistent with the observation that water molecules inside the pores tend to form clusters and move collectively most of the time (see Figure 4-6). In contrast, there is a substantial difference between the molecular MSD and the com MSD for the 32 water molecules/pore loading (VET32) where clusters do not appear to form.

The *z*-component of the self-diffusion coefficients for VET6 is 7.5 – 8.7 × 10^{-9} m^2 s^{-1}, while for VET32 it is 2.1 to 2.3 × 10^{-9} m^2 s^{-1} that is similar to that of bulk water (2.2 – 2.4 × 10^{-9} m^2 s^{-1}) (Horn et al., 2004, Krynicki et al., 1978, Mills, 1973), indicating VET32 diffusion in this direction is similar to that in the bulk. These correspond to values of global D_s of 2.5 – 2.9 × 10^{-9} m^2 s^{-1} and 0.7 – 0.8 × 10^{-9} m^2 s^{-1} for VET6 and VET32, respectively. These values are consistent with those in Ref (Hughes et al., 2011) using the same force field (Hughes et al., 2011, Sanders et al., 1984), assuming 5 unit cells formed pore used for that work (Figure 9 of (Hughes et al., 2011)). As we demonstrate below, at low loadings the values obtained for the diffusion coefficients is very sensitive to the number of unit cells used and not just to the loading.

As stated before, the per-molecule collective diffusion coefficients we obtained (6.6 – 8.1 × 10^{-9} m^2 s^{-1}) are almost identical to our self-diffusion counterparts at the lower loadings, indicating that water is forming stable clusters. While at higher loadings the collective diffusivities per molecule are ca. 0.5 × 10^{-9} m^2 s^{-1} which is 4 times lower than their counterparts.

4.4.2 Structural properties

The radial distribution function (RDF) quantifies how particles are distributed around each other in a certain specified region. We used $g_{pore}(r)$ to characterise cluster sizes and distributions along the channels, where the oxygen atoms of the water molecules were selected as the species of interest.

Figure 4-5 shows $g_{pore}(r)$ for VET6 (4-5(a)) and VET32 (4-5(b)) and using a range of ensembles. The results obtained using the different ensembles are almost indistinguishable for both VET6 and VET32, indicating that the thermostatting/barostatting mechanisms had little effect on the structures. As it can be seen in Figure 4-5(a), for VET6 there is a very high peak at short distances (ca. just below 3 Å) corresponding to the nearest neighbour water molecules, followed by another peak at about 4 Å which drops to about one at about 6 Å and then falls to a value closer to zero. The positions of the peaks correspond well with those in $g(r)$ for the oxygen atoms of TIP4P water (Horn et al., 2004, Hughes et al., 2011). It should be noted that pore radius is about 3 Å and that the minimum distance between water molecules at the edge of one pore and those at the edge of an adjacent pore is about 7 Å. Therefore the peak at 6 Å suggests that the water molecules tend to form stable clusters, and the lengths of these clusters are about 6 Å. This phenomenon, to some extent, is consistent with the finding from the study mentioned earlier in which water molecules have a 6 Å size assembly as a starting clustering length in the 11 Å width slit-pore, water clusters with this size seem very stable (Ohba et al., 2005). Integration of $g_{pore}(r)$ to 6 Å gives a value of 6.5 (it can be higher than 6 due to the approximation for the pore shell volume made in equation (4-2)), indicating that all the 6 water molecules tend to be clustered together most of the time. This is verified in Figure 4-6, which shows snapshots of the VET6 for the NVT simulation. Furthermore the clusters appear to be of similar length to their width, consistent with a cluster of length 6 Å. The fact that there is a small deviation in $g_{pore}(r)$ from zero at 7 Å is likely to be due to water molecules that have dissociated from the cluster for short periods of time, and at distances beyond this there may also be a contribution from water molecules in adjacent pores.

Considering Figure 4-5(b), it is seen $g_{pore}(r)$ for the water oxygen atoms in VET32 is similar to $g(r)$ for bulk water (Horn et al., 2004, Hughes et al., 2011), with a value close to 1 for $r > 6$ Å. Again, this is consistent with the absence of discrete clusters of water molecules in the system at this density. This is also seen in Figure 4-7 which shows snapshots of the VET32 system at various times.

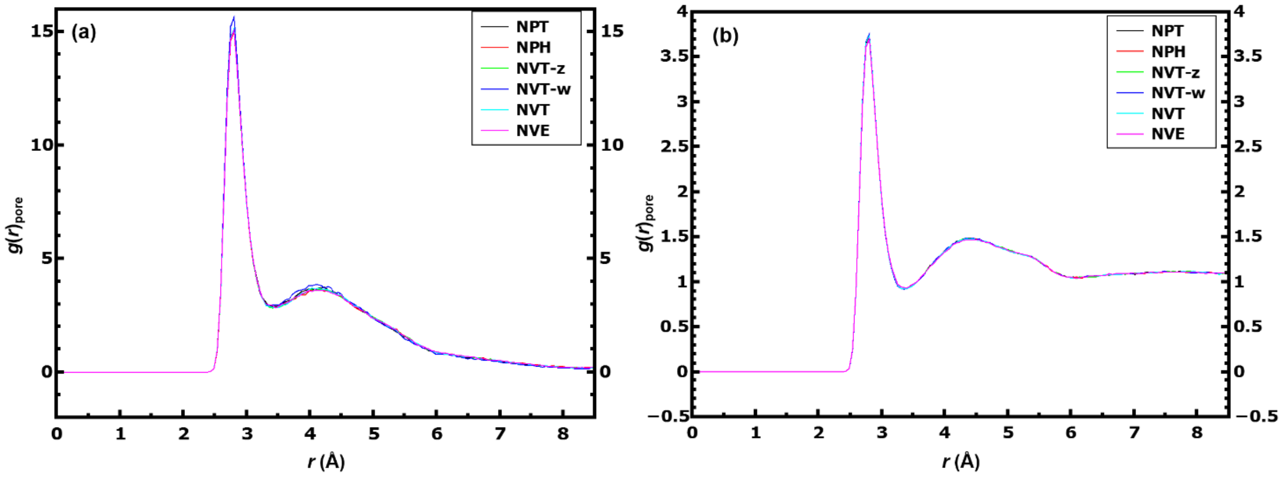

Figure 4-5 The pore radial distribution function, $g_{pore}(r)$ for the O-O atoms of the water molecules in (a) VET6 and (b) VET32. The simulations were carried out using various thermostatting mechanisms as indicated in the legend. The terms NVT-z and NVT-w refer to cases where only the zeolite or water was thermostatted, respectively.

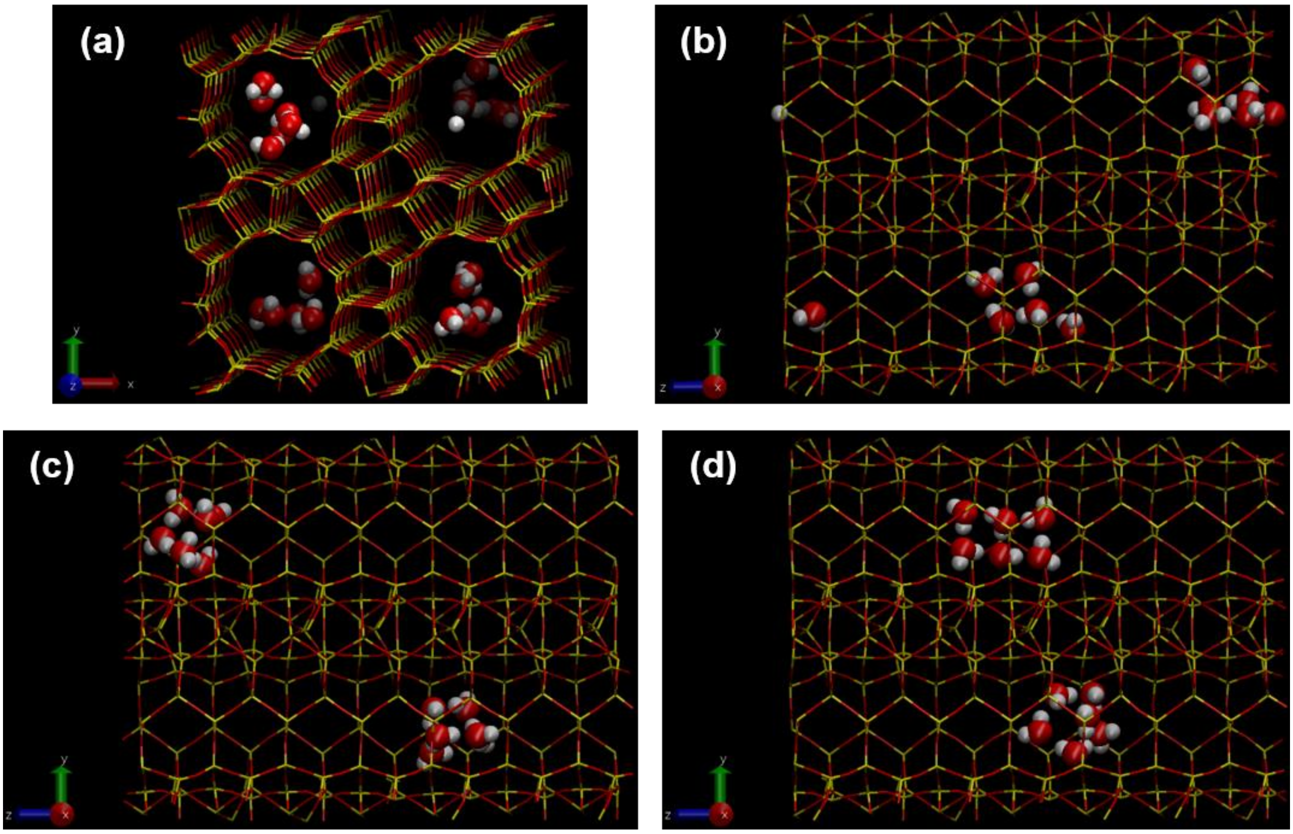

Figure 4-6 Snapshots taken from the VET6 simulations (water represented by ball-and-sticks and zeolites by wires, oxygen coloured in red, hydrogen in white, silicon in yellow): (a) view along the *z*-axis and (b)-(d) views along the *x*-axis initially, at 1000 ps, and at 2000 ps, respectively. Only water molecules in the front pores are shown in (b)-(d), for better visualisation. All *x*-, *y*-, *z*-directions are in periodic boundary condition.

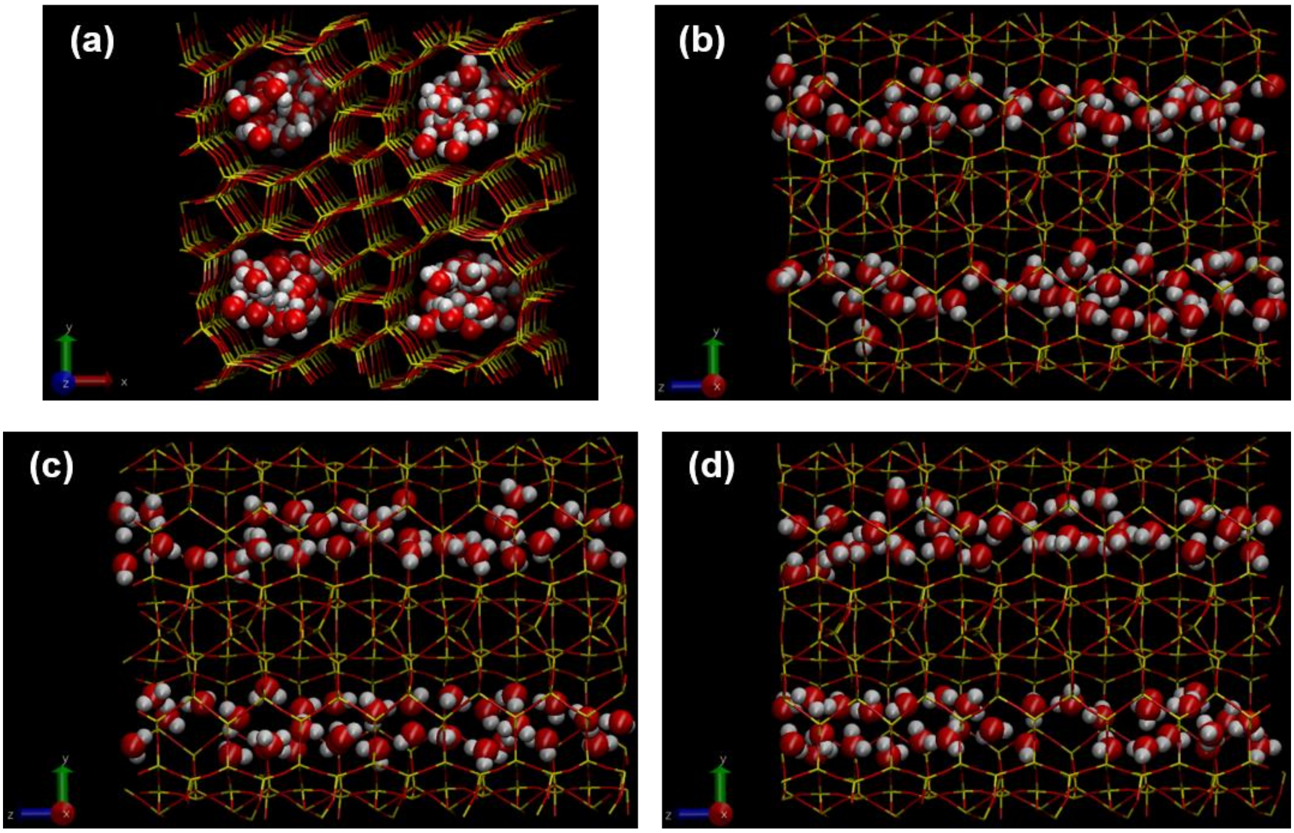

Figure 4-7 Snapshots taken from the VET32 simulations (water represented by ball-and-sticks and zeolites by wires, oxygen coloured in red, hydrogen in white, silicon in yellow): (a) view along the *z*-axis and (b)-(d) views along the *x*-axis initially, at 1000 ps, and at 2000 ps, respectively. Only water molecules in the front pores are shown in (b)-(d), for better visualisation. All *x*-, *y*-, *z*-directions are in periodic boundary condition.

4.4.3 Effects of pore size and length on properties

In Table 4-2, we report the diffusion coefficients depending on the length of the simulation cell and the size of the pores. The water density for VET6, VET12-double, VET18-tri, and VET24-quad has been kept constant (0.39 g cm^{-3}) while the length of the simulation cell is increased i.e. double, three-times, and four-times respectively. This density corresponds to having six water molecules in each of the four pores of VET, built with 2 x 2 x 7 unit cells. As shown in Figure 4-8, VET12-double consisted of 2 x 2 x 14 unit cells while 2 x 2 x 21 and 2 x 2 x 28 cells were used for VET18-tri and VET24-quad respectively. Because the system is periodic, we are simulating an infinitely long pore. However, the periodicity of the cell means that that the properties observed might be different from those obtained without periodicity. In order to obtain results that are comparable with experiment, it is necessary to examine how the properties vary as the length of the periodic cell changes. In the VET6 system it was found that clusters of water molecules were formed and this places limitations on the maximum number of water molecules that can be in the cluster (i.e. 6) and the spacing between clusters. It was therefore of importance to consider the effects of increasing the length of the pore while keeping the average density constant.

Table 4-2 *z*-component of the diffusion coefficients for water in zeolites with various loadings, different simulation cell lengths in different types of zeolites

	Water density / g cm^{-3}	Self (D_{sz}) / 10^{-9} m^2 s^{-1}	Collective (D'_{cz}) / 10^{-9} m^2 s^{-1}
VET6 [a]	0.39	8.1 ± 1.2	7.2 ± 1.2
VET12-double [b]	0.39	3.4 ± 0.5	2.4 ± 0.5
VET18-tri [c]	0.39	3.3 ± 0.4	1.5 ± 0.2
VET24-quad [d]	0.39	3.4 ± 0.2	0.9 ± 0.1
TON6 [e]	0.52	3.4 ± 0.2	1.9 ± 0.2
VET6-tri [f]	0.13	11.3 ± 1.7	9.6 ± 1.2

[a] *6 water molecules in a simulation cell of length 7 unit cells; VET-type zeolite*

[b] *12 water molecules in a simulation cell of length 14 unit cells; VET-type zeolite*

[c] *18 water molecules in a simulation cell of length 21 unit cells; VET-type zeolite*

[d] *24 water molecules in a simulation cell of length 28 unit cells; VET-type zeolite*

[e] *6 water molecules in a simulation cell of length 7 unit cells; TON-type zeolite*

[f] *6 water molecules in a simulation cell of length 21 unit cells; VET-type zeolite*

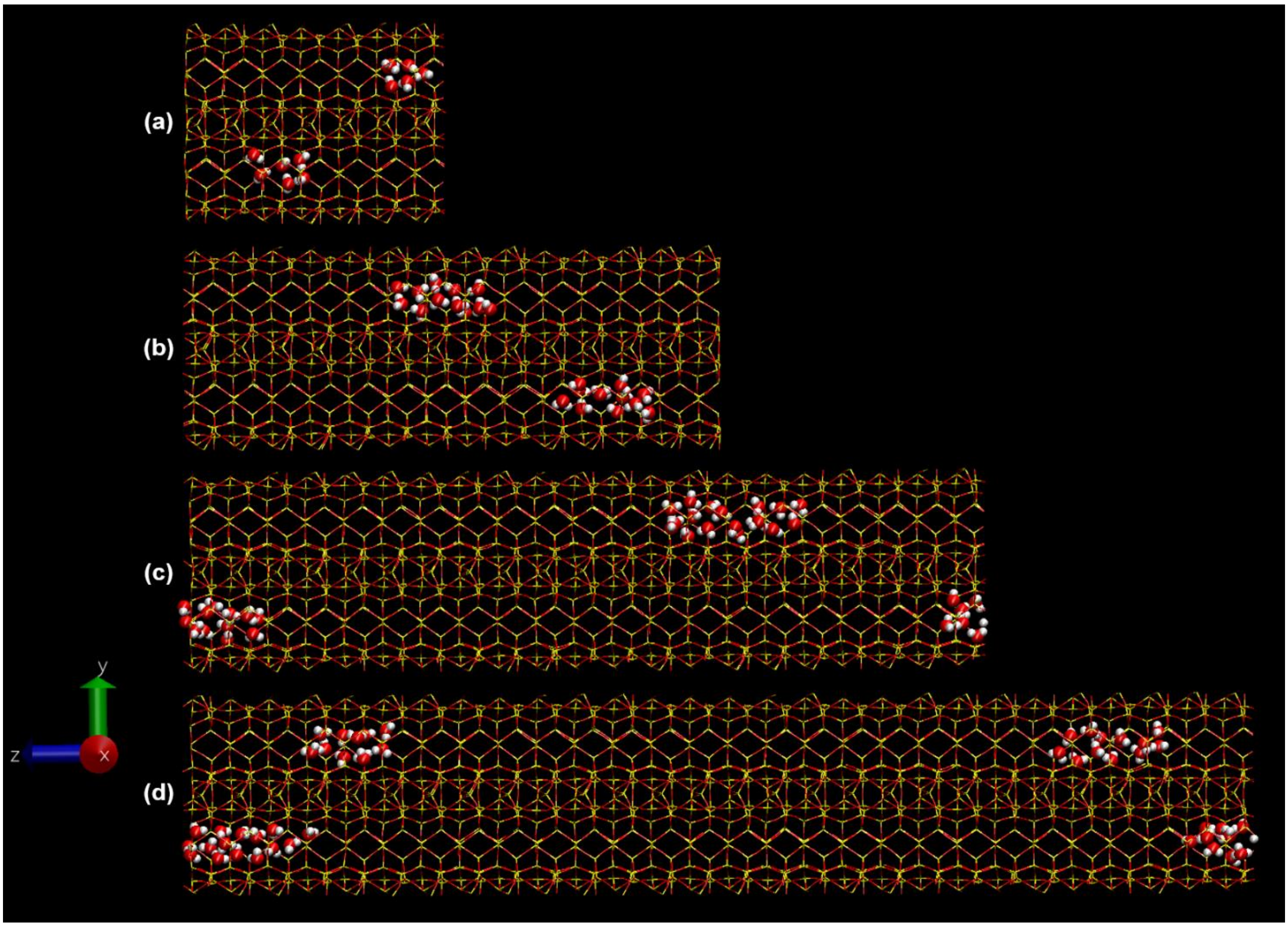

Figure 4-8 Snapshots of (a) VET6, (b) VET12-double, (c) VET18-tri, and (d) VET24-quad (water represented by ball-and-sticks and zeolites by wires, oxygen coloured in red, hydrogen in white, silicon in yellow). Only water molecules in the front pores are shown for better visualisation. *x*-, *y*-, *z*-directions of each simulation cell are in periodic boundary condition.

As can be seen in Table 4-2, VET12-double, VET18-tri, and VET24-quad produce similar *z*-components of the self-diffusion coefficients ($3.3 - 3.4 \times 10^{-9}$ m^2 s^{-1}) but they are significantly lower than the self-diffusion coefficient in VET6. All diffusivities were determined from MSDs computed using the equations (4-3) and (4-4) in which MSDs of the confined water show linear diffusive regimes for all the extended zeolites. We also observe that the value of the *z*-component of the per-molecule collective diffusion coefficient vary, seeming to converge to a value of about 0.9×10^{-9} m^2 s^{-1} when the VET24-quad system is considered. Experimentally, there exists an ideal droplet size and distribution. If this includes droplets with a larger number of water molecules than that existing in the periodic cell, then that droplet cannot form. As the length of the pore, and hence the number of molecules in the periodic cell, increases (while keeping the density constant) the droplet size and its distribution will converge to the thermodynamic value.

As the number of the water molecules increases in the periodic system, the collective diffusivities per molecule will be lower as displayed in Table 4-2. Increasing the number of molecules allows formation of large clusters which diffuse less freely.

The results shown in $g_{pore}(r)$ in Figure 4-9(a) clearly demonstrate differences in the water structure between VET6 and the extended zeolites. In VET6, $g_{pore}(r)$ drops below 1 at about 6 Å, suggesting that water clusters of 6 molecules exist and are quite stable. Comparing with VET12-double, VET18-tri, and VET24-quad we see several differences although the water densities are the same. Firstly, when comparing to the second peak, the first peak is relatively higher for VET6. This is consistent with the formation of clusters in which more water molecules are involved in the first shell of the cluster: the first peak represents the average number of water molecules directly hydrogen-bonded to the molecule of interest, or its coordination number. In a water cluster in a pore, the water molecules at the ends of the cluster will have lower coordination numbers than those in the centre of the cluster, and therefore the longer the cluster, the higher the average coordination number will be. This will also be evident in the height of the second peak. Comparison of the heights of the first peak with different simulation cell lengths indicates that the average cluster size is growing considerably as the number of water molecules increases from 6 to 12 (with corresponding increases in the length of the cell), and there is a further increase in VET18-tri with little change going to VET24-quad. The length of these clusters grows and from the images in Figure 4-8, clusters of over 26 Å form in VET24, however several clusters can co-exist and clusters of 6 molecules are still common. The formation of long clusters is reflected in the fact that $g_{pore}(r)$ is still well above 1 in the region 7 - 8.5 Å in all cases considered in 4-9(a) except the VET6 system. These results indicate that in considering the relatively low water loadings where clusters tend to form, it is important to examine the system size effect before comparison of the results with experiment. Although the z-component of the self-diffusion coefficient in VET6 is well above the self-diffusion coefficient of bulk water, a more reliable value is obtained using the longer simulations cells. It is interesting to observe that this value is also above that of bulk water and VET32, indicating that the clustering results in enhanced self-diffusion just as shown in existing literature regarding water diffusion through nanotubes (Alberto, 2007, Falk et al., 2010, Cicero et al., 2008). Comparison of the collective diffusion coefficient in VET24-quad with that in VET32 suggests that collective diffusion coefficient is only slightly lower at the higher loading, and that order of magnitude enhancement observed with VET6 was misleading.

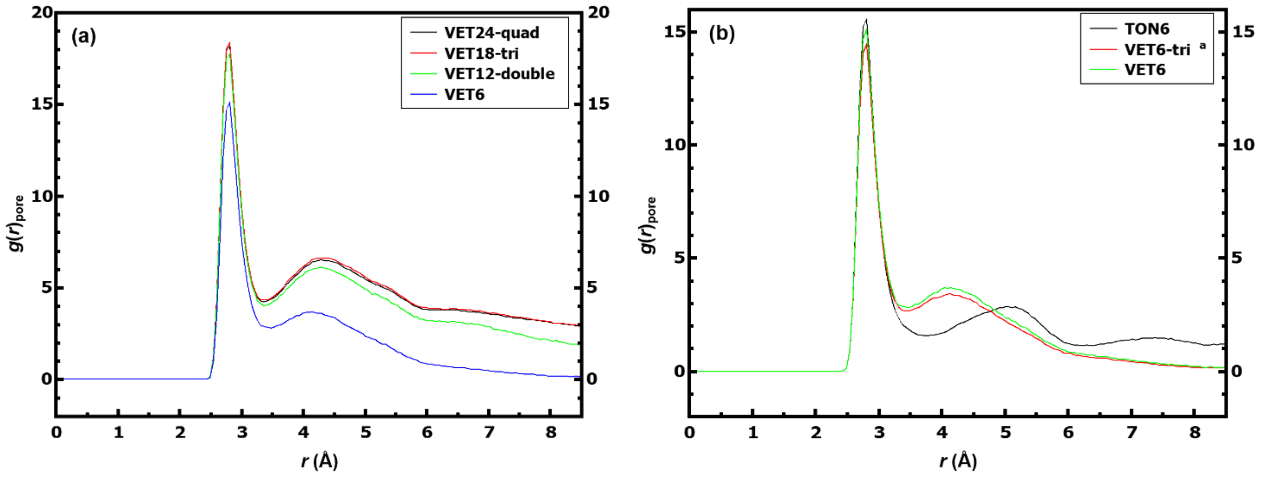

Figure 4-9 The pore radial distribution function, $g_{pore}(r)$ for the O-O atoms of the water for (a) various loadings, and (b) different simulation cell lengths in different types of zeolites.

Considering VET24-quad, we can conclude that at lower loadings the self-diffusion coefficient ($D_s = D_{sz}/3 = 1.1 \times 10^{-9}$ m^2 s^{-1}) is about 5 times higher than that found in commercially used polyamide membranes when hydrated ca. 0.2×10^{-9} m^2 s^{-1} (Ding et al., 2014, Hughes and Gale, 2010, Hughes and Gale, 2012). According to previous work on polyamide membranes, the hydrated membrane contains 23 wt% of water in the pores, meaning that the water density in the commercial membrane is 0.32 g/cm^3 which is similar to that of the lower loadings case (0.39 g cm^{-3}) in this study. We can also compare these results to those from different zeolite membrane candidates that have been previously determined: the self-diffusivities have been reported as $1.0 - 4.0 \times 10^{-9}$ m^2 s^{-1} (Bussai et al., 2002, Yang et al., 2008, Joshi et al., 2014, Caro et al., 1987) when 0.47 g/cm^3 of water is loaded in MFI zeolites, while hydrated LTA zeolites have values of ~0.5×10^{-9} m^2 s^{-1} (Demontis et al., 2010, Lin and Murad, 2001). Those values are comparable to and about 2 times lower than VET24-quad (1.1×10^{-9} m^2 s^{-1}), respectively. Given that MFI and LTA zeolites possess fully-connected 3-D pores, well-defined 1-D channels of VET will produce much higher water transport in one-direction than the 3-D pores. This high diffusivity can be associated with the hydrophobic nature of the pore which enhances the formation of nanodroplets. Even for the higher loadings, i.e. 32 water molecules per pore, diffusivities are approximately four times higher than the polyamide membranes, and the self-diffusion coefficient in the z-direction nearly corresponds to the self-diffusion coefficient for bulk water. At high loadings water-water interactions becomes dominant for the diffusive behaviour as opposed to water-zeolite interactions.

In VET6 and TON6, 6 water molecules were placed in simulation cells consisting of 7 unit cells, however due to the different pore sizes their number densities were different (0.39 g cm^{-3} for

VET6 and 0.52 g cm^{-3} for TON6). Figure 4-9(b) compares $g_{pore}(r)$ for these systems and the results indicate the water molecules do not form stable 6 membered clusters in TON6. The shifted second peak suggests the formation of chains of molecules, however the linearity of the MSD versus time indicates molecules can pass one another. Comparison of the snapshots in Figures 4-10 and 4-6 verify this result and also indicate that the chains vary in length and are less stable. TON6 has a lower self-diffusion coefficient than VET6, and its self-diffusion and collective diffusion coefficients differ, however it should be noted that the results are similar to those obtained for VET24-quad, and the collective diffusion coefficient is somewhat higher.

We also consider the effect of density on the results by comparing the results of 6 water molecules in a pore consisting of 21 unit cells in the *z*-direction (VET6-tri) with VET6. The VET6-tri (6 water molecules/triple-longer pore) results a slightly higher self and collective diffusivity than VET6, although the statistical significance of the difference is marginal. Figure 4-9(b) compares $g_{pore}(r)$ for these systems and the results are very similar, indicating that the structures in the two cases are very similar. Presumably as the density of the water decreases, a phase transition will occur and the clusters will dissociate, however even at this low density of 0.13 g/cm^3, this has not occurred. Effect of density difference and same density with different pore geometries on transport and structure of water confined in zeolites will be further studied in the next chapter.

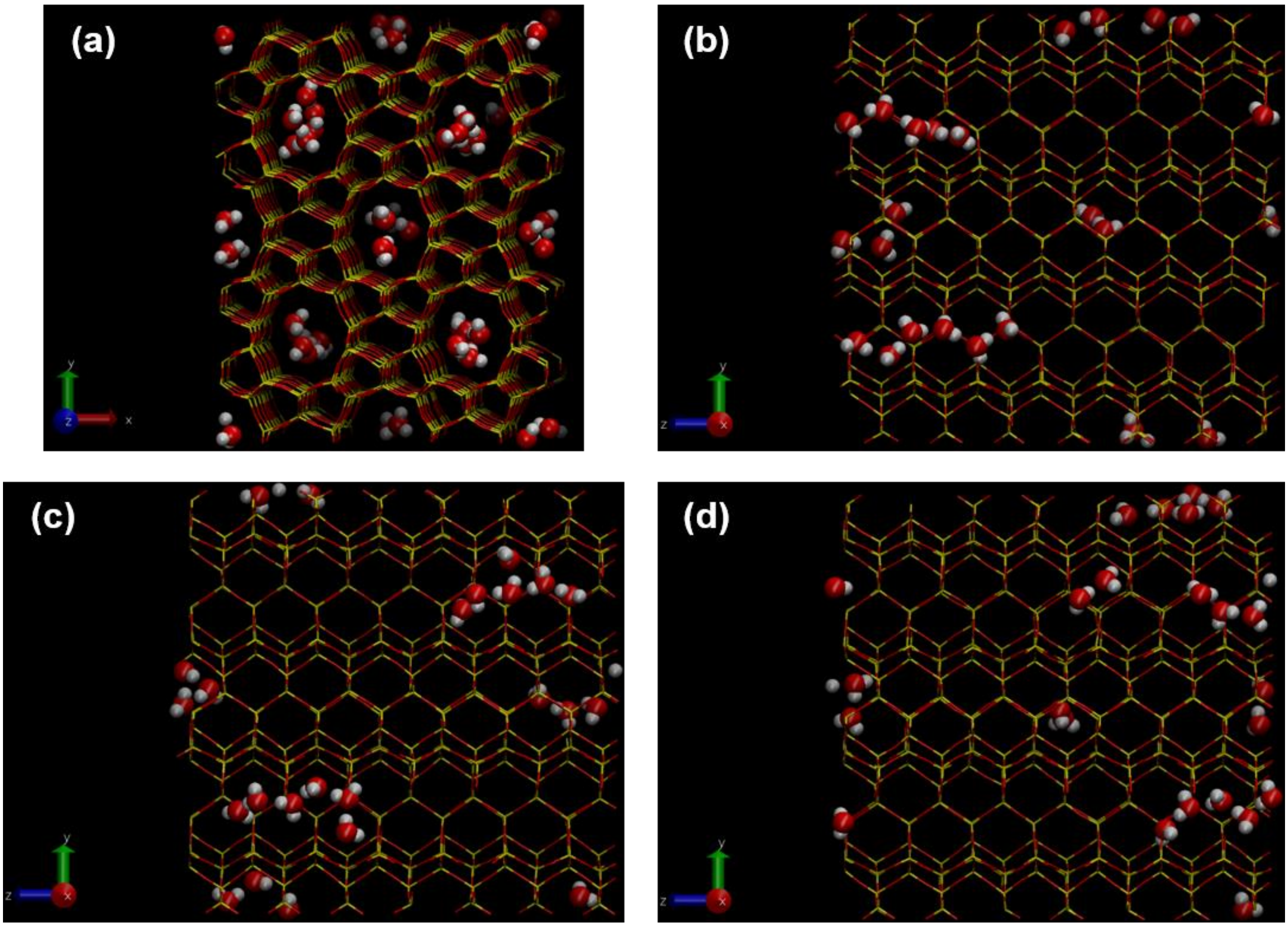

Figure 4-10 Snapshots of TON6 simulations (water represented by ball-and-sticks and zeolites by wires, oxygen coloured in red, hydrogen in white, silicon in yellow): (a) view along the *z*-axis and (b)-(d) views along the *x*-axis initially, at 1000 ps, and at 2000 ps, respectively. Only water molecules in four of the pores are shown in (b)-(d), for better visualisation. *x*-, *y*-, *z*-directions of each simulation cell are in periodic boundary condition.

4.5 Conclusions

In this study, transport and structural properties of water inside zeolites were explored using MD simulations, with the aim of assessing a class of candidate zeolites as membrane materials. Force fields previously validated against experimental data were employed. Different thermostatting strategies were investigated. The thermostatting mechanism had little effect on the diffusion coefficients for water confined in a VET zeolite and even produced consistent results with those obtained from NVE and NPT simulations.

Long, narrow pores with the same loading and/or the same density were also examined. Considering low loadings of water, when the simulation cell size was increased while keeping the same density as VET6, self-diffusivities in the *z*-direction were observed to converge to ca. 3.4×10^{-9} m^2 s^{-1}. It should be noted that at low loadings, it is important to ensure that the number of unit cells along the pore is sufficient that convergence to thermodynamic behaviour is obtained or otherwise non-physical results are obtained due to the upper bound on the number of water molecules in the water cluster. For example the results obtained for VET6 (6 water molecules per pore) does not give an accurate prediction for the self-diffusion coefficient of a system with a loading of 0.39 g cm^{-3} because it prevents the formation of clusters larger than 6 molecules.

TON6 has a comparable self-diffusivity to that of VET24-quad, but a higher collective diffusivity per particle. This is because the water molecules did not form a stable cluster, resulting the collective diffusivity being significantly lower than the self-diffusivity.

High diffusion rates for both low and high water loading were measured compared with commercially-available polyamide membranes. The self-diffusivities for VET24-quad, VET32, and TON6 were all higher than for the polyamide membrane (ca. 0.2×10^{-9} m^2 s^{-1}) that are currently used for water desalination, suggesting that these materials may be useful. In particular, the fully-loaded VET32 had a comparable self-diffusion rate with bulk water (2.3×10^{-9} m^2 s^{-1}) even though the water density of VET32 was twofold higher (2.1 g/cm^3).

This study on the diffusional and structural properties of confined water in zeolites has analysed a number of important issues that need to be considered in evaluation of diffusion coefficients for fluids in pores using computational methods. It suggests that the one dimensional cylindrical pores can result in higher diffusivities, guiding the selection of future membranes for practical applications.

References

ALBERTO, S. 2007. Water self-diffusion through narrow oxygenated carbon nanotubes. *Nanotechnology,* 18**,** 475704.

ALEXANDER, S. & PINCUS, P. 1978. Diffusion of labeled particles on one-dimensional chains. *Physical Review B,* 18**,** 2011-2012.

ALEXIADIS, A. & KASSINOS, S. 2008. Molecular Simulation of Water in Carbon Nanotubes. *Chemical Reviews,* 108**,** 5014-5034.

Arı, M. U., AHUNBAY, M. G., YURTSEVER, M. & ERDEM-ŞENATALAR, A. 2009. Molecular Dynamics Simulation of Water Diffusion in MFI-Type Zeolites. *Journal of Physical Chemistry B,* 113**,** 8073-8079.

AUERBACH, S. M., CARRADO, K. A. & DUTTA, P. K. 2003. Handbook of Zeolite Science and Technology. New York: CRC Press.

BAERLOCHER, Ch. & MCCUSKER, L. B. 2015. *Database of Zeolite Structures* [Online]. http://www.iza-structure.org/databases/, IZA-SC. Available: http://www.iza-structure.org/databases/ [Accessed 15 Sep 2016].

BASCONI, J. E. & SHIRTS, M. R. 2013. Effects of Temperature Control Algorithms on Transport Properties and Kinetics in Molecular Dynamics Simulations. *Journal of Chemical Theory and Computation,* 9**,** 2887-2899.

BERNARDI, S., TODD, B. D. & SEARLES, D. J. 2010. Thermostating highly confined fluids. *The Journal of Chemical Physics,* 132**,** 244706.

BRIGHT, J. N., EVANS, D. J. & SEARLES, D. J. 2005. New observations regarding deterministic, time-reversible thermostats and Gauss's principle of least constraint. *The Journal of Chemical Physics,* 122**,** 194106.

BUSSAI, C., VASENKOV, S., LIU, H., BÖHLMANN, W., FRITZSCHE, S., HANNONGBUA, S., HABERLANDT, R. & KÄRGER, J. 2002. On the diffusion of water in silicalite-1: MD simulations using ab initio fitted potential and PFG NMR measurements. *Applied Catalysis A: General,* 232**,** 59-66.

CARO, J., BÜLOW, M., RICHTER-MENDAU, J., KÄRGER, J., HUNGER, M., FREUDE, D. & REES, L. V. C. 1987. Nuclear magnetic resonance self-diffusion studies of methanol-water mixtures in pentasil-type zeolites. *Journal of the Chemical Society, Faraday Transactions 1:*

Physical Chemistry in Condensed Phases, 83**,** 1843-1849.

CHI, Z., LUO, C. & DAI, Y. 2014. Comment on "Electrical-Driven Transport of Endohedral Fullerene Encapsulating a Single Water Molecule". *Physical Review Letters,* 113**,** 119601.

CICERO, G., GROSSMAN, J. C., SCHWEGLER, E., GYGI, F. & GALLI, G. 2008. Water Confined in Nanotubes and between Graphene Sheets: A First Principle Study. *Journal of the American Chemical Society,* 130**,** 1871-1878.

COHEN-TANUGI, D. & GROSSMAN, J. C. 2012. Water Desalination across Nanoporous Graphene. *Nano Letters,* 12**,** 3602-3608.

COHEN-TANUGI, D. & GROSSMAN, J. C. 2014. Water permeability of nanoporous graphene at realistic pressures for reverse osmosis desalination. *The Journal of Chemical Physics,* 141**,** 074704.

DE LEEUW, N. H. & PARKER, S. C. 1998. Molecular-dynamics simulation of MgO surfaces in liquid water using a shell-model potential for water. *Physical Review B,* 58**,** 13901-13908.

DEMONTIS, P., GULÍN-GONZÁLEZ, J., JOBIC, H., MASIA, M., SALE, R. & SUFFRITTI, G. B. 2008. Dynamical Properties of Confined Water Nanoclusters: Simulation Study of Hydrated Zeolite NaA: Structural and Vibrational Properties. *ACS Nano,* 2**,** 1603-1614.

DEMONTIS, P., GULÍN-GONZÁLEZ, J., JOBIC, H. & SUFFRITTI, G. B. 2010. Diffusion of Water in Zeolites Na A and NaCa A: A Molecular Dynamics Simulation Study. *The Journal of Physical Chemistry C,* 114**,** 18612-18621.

DING, M., SZYMCZYK, A., GOUJON, F., SOLDERA, A. & GHOUFI, A. 2014. Structure and dynamics of water confined in a polyamide reverse-osmosis membrane: A molecular-simulation study. *Journal of Membrane Science,* 458**,** 236-244.

DROBEK, M., YACOU, C., MOTUZAS, J., JULBE, A., DING, L. & DINIZ DA COSTA, J. C. 2012. Long term pervaporation desalination of tubular MFI zeolite membranes. *Journal of Membrane Science,* 415–416**,** 816-823.

DUKE, M. C., O'BRIEN-ABRAHAM, J., MILNE, N., ZHU, B., LIN, J. Y. S. & DA COSTA, J. C. D. 2009. Seawater desalination performance of MFI type membranes made by secondary growth. *Separation and Purification Technology,* 68**,** 343-350.

EVANS, D. J. & MORRISS, G. 2008. *Statistical Mechanics of Nonequilibrium Liquids,* London, Cambridge University Press.

FALK, K., SEDLMEIER, F., JOLY, L., NETZ, R. R. & BOCQUET, L. 2010. Molecular Origin of

Fast Water Transport in Carbon Nanotube Membranes: Superlubricity versus Curvature Dependent Friction. *Nano Letters,* 10**,** 4067-4073.

FEDDERS, P. A. 1978. Two-point correlation functions for a distinguishable particle hopping on a uniform one-dimensional chain. *Physical Review B,* 17**,** 40-46.

FELDERHOF, B. U. 2009. Fluctuation theory of single-file diffusion. *The Journal of Chemical Physics,* 131**,** 064504.

FIRST, E. L., GOUNARIS, C. E., WEI, J. & FLOUDAS, C. A. 2011. Computational characterization of zeolite porous networks: an automated approach. *Physical Chemistry Chemical Physics,* 13**,** 17339-17358.

FREYHARDT, C. C., LOBO, R. F., KHODABANDEH, S., LEWIS, J. E., TSAPATSIS, M., YOSHIKAWA, M., CAMBLOR, M. A., PAN, M., HELMKAMP, M. M., ZONES, S. I. & DAVIS, M. E. 1996. VPI-8: A High-Silica Molecular Sieve with a Novel “Pinwheel” Building Unit and Its Implications for the Synthesis of Extra-Large Pore Molecular Sieves. *Journal of the American Chemical Society,* 118**,** 7299-7310.

GASCON, J., KAPTEIJN, F., ZORNOZA, B., SEBASTIAN, V., CASADO, C. & CORONAS, J. 2012. Practical Approach to Zeolitic Membranes and Coatings: State of the Art, Opportunities, Barriers, and Future Perspectives. *Chemistry of Materials,* 24**,** 2829-2844.

GRANDA-VALDÉS, M., PÉREZ-CORDOVES, A. I. & DÍAZ-GARCÍA, M. E. 2006. Zeolites and zeolite-based materials in analytical chemistry. *Trends in Analytical Chemistry,* 25**,** 24-30.

GUBBINS, K. E., LIU, Y.-C., MOORE, J. D. & PALMER, J. C. 2011. The role of molecular modeling in confined systems: impact and prospects. *Physical Chemistry Chemical Physics,* 13**,** 58-85.

HOCKNEY, R. W. & EASTWOOD, J. W. 1988b. Particle-Particle-Particle-Mesh (P3M) Algorithms. *Computer simulation using particles.* CRC Press.

HOLT, J. K., PARK, H. G., WANG, Y. M., STADERMANN, M., ARTYUKHIN, A. B., GRIGOROPOULOS, C. P., NOY, A. & BAKAJIN, O. 2006. Fast mass transport through sub-2-nanometer carbon nanotubes. *Science,* 312**,** 1034-1037.

HORN, H. W., SWOPE, W. C. & PITERA, J. W. 2005. Characterization of the TIP4P-Ew water model: vapor pressure and boiling point. *Journal of Chemical Physics,* 123**,** 194504.

HORN, H. W., SWOPE, W. C., PITERA, J. W., MADURA, J. D., DICK, T. J., HURA, G. L. & HEAD-GORDON, T. 2004. Development of an improved four-site water model for biomolecular simulations: TIP4P-Ew. *Journal of Chemical Physics,* 120**,** 9665-9678.

HUGHES, Z. E., CARRINGTON, L. A., RAITERI, P. & GALE, J. D. 2011. A Computational Investigation into the Suitability of Purely Siliceous Zeolites as Reverse Osmosis Membranes. *The Journal of Physical Chemistry C,* 115**,** 4063-4075.

HUGHES, Z. E. & GALE, J. D. 2010. A computational investigation of the properties of a reverse osmosis membrane. *Journal of Materials Chemistry,* 20**,** 7788-7799.

HUGHES, Z. E. & GALE, J. D. 2012. Molecular dynamics simulations of the interactions of potential foulant molecules and a reverse osmosis membrane. *Journal of Materials Chemistry,* 22**,** 175-184.

HÜNENBERGER, P. 2005. Thermostat Algorithms for Molecular Dynamics Simulations. *In:* HOLM, C. & KREMER, K. (eds.) *Advanced Computer Simulation.* Springer Berlin Heidelberg.

IIYAMA, T., ARAGAKI, R., URUSHIBARA, T. & OZEKI, S. 2006. Direct Determination of the Intermolecular Structure of the Adsorbed Phase Using *in situ* X-Ray Diffraction and Reverse Monte Carlo Methods. *Adsorption Science & Technology,* 24**,** 815-821.

JENSEN, F. 2007. *Introduction to Computational Chemistry,* UK, Wiley.

JOBIC, H., KÄRGER, J. & BÉE, M. 1999. Simultaneous Measurement of Self- and Transport Diffusivities in Zeolites. *Physical Review Letters,* 82**,** 4260-4263.

JOSHI, K. L., PSOFOGIANNAKIS, G., VAN DUIN, A. C. T. & RAMAN, S. 2014. Reactive molecular simulations of protonation of water clusters and depletion of acidity in H-ZSM-5 zeolite. *Physical Chemistry Chemical Physics,* 16**,** 18433-18441.

KAPTEIJN, F., BAKKER, W. J. W., ZHENG, G., POPPE, J. & MOULIJN, J. A. 1995. Permeation and separation of light hydrocarbons through a silicalite-1 membrane: Application of the generalized Maxwell-Stefan equations. *The Chemical Engineering Journal and the Biochemical Engineering Journal,* 57**,** 145-153.

KRISHNAN, T. V. S., BABU, J. S. & SATHIAN, S. P. 2013. A molecular dynamics study on the effect of thermostat selection on the physical behavior of water molecules inside single walled carbon nanotubes. *Journal of Molecular Liquids,* 188**,** 42-48.

KRYNICKI, K., GREEN, C. D. & SAWYER, D. W. 1978. Pressure and temperature dependence of self-diffusion in water. *Faraday Discussions of the Chemical Society,* 66**,** 199-208.

LEE, K. P., ARNOT, T. C. & MATTIA, D. 2011. A review of reverse osmosis membrane materials for desalination-Development to date and future potential. *Journal of Membrane Science,* 370**,** 1-22.

LI, D. & WANG, H. T. 2010. Recent developments in reverse osmosis desalination membranes. *Journal of Materials Chemistry,* 20**,** 4551-4566.

LIN, J. & MURAD, S. 2001. A computer simulation study of the separation of aqueous solutions using thin zeolite membranes. *Molecular Physics,* 99**,** 1175-1181.

LIU, Y. & CHEN, X. 2013. High permeability and salt rejection reverse osmosis by a zeolite nano-membrane. *Physical Chemistry Chemical Physics,* 15**,** 6817-6824.

MARTYNA, G. J., TOBIAS, D. J. & KLEIN, M. L. 1994. Constant pressure molecular dynamics algorithms. *The Journal of Chemical Physics,* 101**,** 4177-4189.

MILLS, R. 1973. Self-diffusion in normal and heavy water in the range 1-45.deg. *The Journal of Physical Chemistry,* 77**,** 685-688.

NGUYEN, T. X. & BHATIA, S. K. 2012. Some Anomalies in the Self-Diffusion of Water in Disordered Carbons. *The Journal of Physical Chemistry C,* 116**,** 3667-3676.

OHBA, T. & KANEKO, K. 2009. Initial filling mechanism of predominant water adsorption on hydrophobic slit-shaped carbon nanopores. *Journal of Physics: Conference Series,* 177**,** 012001.

OHBA, T., KANOH, H. & KANEKO, K. 2005. Water cluster growth in hydrophobic solid nanospaces. *Chemistry - A European Journal,* 11**,** 4890-4894.

PLIMPTON, S. J. 1995. Fast Parallel Algorithms for Short-Range Molecular Dynamics. *Journal of Computational Physics,* 117**,** 1-19.

RAPAPORT, D. C. 2004. *The Art of Molecular Dynamics Simulation,* Cambridge, UK, Cambridge University Press.

RYCKAERT, J.-P., CICCOTTI, G. & BERENDSEN, H. J. C. 1977. Numerical integration of the cartesian equations of motion of a system with constraints: molecular dynamics of n-alkanes. *Journal of Computational Physics,* 23**,** 327-341.

SANDERS, M. J., LESLIE, M. & CATLOW, C. R. A. 1984. Interatomic potentials for SiO2. *Journal of the Chemical Society, Chemical Communications***,** 1271-1273.

SHINODA, W., SHIGA, M. & MIKAMI, M. 2004. Rapid estimation of elastic constants by molecular dynamics simulation under constant stress. *Physical Review B,* 69**,** 134103.

SMIT, B. 1992. Phase diagrams of Lennard-Jones fluids. *The Journal of Chemical Physics,* 96**,** 8639-8640.

SMITH, W. F. & HASHEMI, J. 2009. *Foundations of Materials Science and Engineering,* London, UK, McGraw-Hill.

THIJSSEN, J. M. 2007. *Computational Physics,* Cambridge, UK, Cambridge University Press.

THOMAS, M. & CORRY, B. 2014. Thermostat choice significantly influences water flow rates in molecular dynamics studies of carbon nanotubes. *Microfluidics and Nanofluidics***,** 1-7.

WANG, L., DUMONT, R. S. & DICKSON, J. M. 2013. Nonequilibrium molecular dynamics simulation of pressure-driven water transport through modified CNT membranes. *Journal of Chemical Physics,* 138.

YANG, J. Z., CHEN, Y., ZHU, A. M., LIU, Q. L. & WU, J. Y. 2008. Analyzing diffusion behaviors of methanol/water through MFI membranes by molecular simulation. *Journal of Membrane Science,* 318**,** 327-333.

YONG, X. & ZHANG, L. T. 2013. Thermostats and thermostat strategies for molecular dynamics simulations of nanofluidics. *The Journal of Chemical Physics,* 138**,** -.

ZHANG, Q., CHAN, K.-Y. & QUIRKE, N. 2009. Molecular dynamics simulation of water confined in a nanopore of amorphous silica. *Molecular Simulation,* 35**,** 1215-1223.

ZHU, B., DOHERTY, C. M., HU, X. R., HILL, A. J., ZOU, L. D., LIN, Y. S. & DUKE, M. 2013. Designing hierarchical porous features of ZSM-5 zeolites via Si/Al ratio and their dynamic behavior in seawater ion complexes. *Microporous and Mesoporous Materials,* 173**,** 78-85.

Chapter 5 Water structure and transport in zeolites with pores in one or three dimensions: a molecular dynamics simulation study

5.1 Abstract

Molecular dynamics simulations were carried out to explore the kinetic and structural properties of water diffusing through several types of zeolite with pore sizes that make them suitable for application as membranes for small ion filtering. Zeolites with pores in one and three dimensions were considered and insights into the effect of the structures of the zeolites were obtained by studying diffusion and ordering of the confined water. Interestingly, water molecules in the zeolites with pores in one-dimension showed up to 2.5-fold higher diffusivities than in those with pores in three-dimensions for a given water density and a similar pore diameter. The distribution of water molecules across pores and the number of water molecules in a specified region were also investigated to determine the effects of pore shape and size on the water assembly. The arrangement and the number of water molecules in a cluster were observed to depend heavily on the shape and size of pores. The present study provides a deeper understanding of how various structural features affect the dynamics and structure of the water within zeolites.

5.2 Introduction

Zeolites are microporous crystalline materials that are widely used as membranes in ion exchange, gas separation and desalination due to a variety of channel structures, pore sizes and chemical compositions. In particular, with increasing global demand for clean water, zeolite membranes have attracted growing attention as desalination materials in the last decades due to their high selectivity, chemical stability and mechanical strength. Lin and Murad (Lin and Murad, 2001, Murad and Lin, 2001) carried out computational studies on the separation of water from NaCl solution using a ZK-4 (all-silica LTA zeolite) membrane to demonstrate their utility. Kazemimoghadam (Kazemimoghadam, 2010) synthesised hydroxysodalite (SOD zeolite) and set the prepared membrane in a lab-scale reverse-osmosis system to test desalination performance. Another computational study on zeolites as membranes by Liu and Chen (Liu and Chen, 2013) compared MFI with FAU zeolites, and considered the effects the of hydrophilicity, membrane thickness and water loading. Recently, MFI-type zeolites, silicalite (all-silica) and ZSM-5, have been intensively studied in experiments and computer simulations to investigate their use as future desalination materials (Wenten and Khoiruddin, 2016, Liu and Chen, 2013, Dong et al., 2015, Zhu et al., 2013, Drobek et al., 2012). However, despite the intensive efforts to study their suitability as for water purification, zeolites and zeolite-incorporated membranes are still not a suitable commercial option due to their poor water flux.

In recent years, carbon nanotubes (CNTs) and porous graphene have been studied as an alternative to conventional polymeric membrane materials (Corry, 2011, Cohen-Tanugi and Grossman, 2012, Wang et al., 2013, Cohen-Tanugi and Grossman, 2014, Gai et al., 2014). The advantage of these materials is that their pores are well-defined and the pores can be manufactured with sizes of less than 1 nm, which is suitable for rejection of salt ions (Wang et al., 2013, Cohen-Tanugi and Grossman, 2014, Holt et al., 2006). Also, ultrafast water flow takes place through the pores due to their smooth and hydrophobic walls (Alexiadis and Kassinos, 2008, Holt et al., 2006, Cohen-Tanugi and Grossman, 2012). However, manufacturing high density, small and well-defined pores of uniform pore size is very challenging, and not commercially viable with current techniques (Liu and Chen, 2013). In contrast, zeolites are crystalline structures that are naturally-occurring or can be more easily fabricated. The pores in zeolites are well-defined and closely-packed, giving a high pore density. Also, zeolites with channels/pores all in aligned in one direction (which we refer to as '1-D pores zeolites') and suitable pore diameter show a high potential as desalination membrane materials due to their higher water flow rates as in the case for CNT.

Only a few studies have been carried out on the performance of 1-D pore zeolites in desalination. Hughes *et al.* (Hughes et al., 2011) investigated the behaviour of water in all-silica 1-D pore zeolites and their use as desalination membranes by employing quantum mechanical and molecular dynamics calculations, and found higher self-diffusivities than those obtained from conventional polyamide membranes (ca. 0.2×10^{-9} m^2 s^{-1}) (Ding et al., 2014b, Hughes and Gale, 2010, Hughes and Gale, 2012). In addition, it was shown that the penetration of Cl^- into the framework was energetically unfavourable. In our previous work (Han et al., 2015), two different 1-D pore zeolites (i.e. VET- and TON-type) were examined, and self-diffusion coefficients were found to be around 5 times higher than that in commercial aromatic polyamide membranes (Ding et al., 2014a) with water densities of 0.39 and 0.52 g cm^{-3}. Additionally, we found promising collective diffusion coefficients of $11.5 - 23.4 \times 10^{-9}$ m^2 s^{-1}.[1]

---

[1] Note that a non-standard definition was used in Chapter 4, whereas these values are obtained using the standard definition (see equation (5-3)).

Although it is still challenging to align 1-D pores normal to the zeolite surface, some attempts have recently been made to control the direction of the crystal growth. It is reported that zeolite crystal patterns can be controlled by using organic molecules, called zeolite growth modifiers, to tailor crystal direction, thickness, and morphology (Rimer, 2012, Rimer et al., 2014). Therefore, the technique will make it more feasible to use 1-D pore zeolite membranes for desalination.

Studies on water behaviour within hydrophobic two-dimensional (2-D) slits and three-dimensional (3-D) pores has previously been carried out both experimentally and computationally. Small-angle X-ray scattering (SAXS) and grand canonical Monte Carlo (GCMC) studies have revealed that water molecules form clusters which are 6 Å in diameter within a 11 Å width slit-pore under 0.6 relative pressure (P/P_0), and with increasing pressure (higher water loading) the cluster becomes larger due to fusion of different clusters (Ohba et al., 2005). Another study found that ice-like structures of water clusters, which were about 15 Å in diameter, are formed in slit-pores of 16.3 Å width at $P/P_0 = 0.6$ by using X-ray diffraction (XRD) measurements and reverse Monte Carlo simulations (Iiyama et al., 2006). In addition, some interesting studies have been performed for slit-pores of different widths (7 Å and 11 Å), showing that the kinetics of the water assembly is mainly affected by the pore width at low pressure (under $P/P_0 = 0.5$) and that water adsorption rates are faster for the narrower pores at just above the critical pressure (0.4 for 7 Å width and 0.6 for 11 Å) (Ohba and Kaneko, 2009). Water clusters also form within cage-like pores of the LTA zeolite: 11 Å diameter α-cages hold 24 molecules in a cluster, whereas 6 Å β-cages can hold 4 molecules (Demontis et al., 2008). However, a complete theoretical understanding of water behaviour in nanostructures is still lacking.

In this study molecular dynamics (MD) simulations are used to characterize the kinetics, dynamics and structure of water confined in zeolites with different dimensionality and morphology. As found in our previous work (Han et al., 2015), clustering of water has a significant impact on the self and collective diffusion coefficients. Therefore, we examine how the cluster size and stability affect water diffusivity in 1-D pore zeolites and zeolites with channels in three directions (referred to as ‘3-D pore zeolites’) that could potentially offer faster diffusion rates than the most commonly considered 3-D channel zeolites (i.e. MFI and LTA) or the commercial polymeric membranes.

5.3 Methods

5.3.1 Zeolite construction and force field

Six different types of zeolites were investigated and compared in this work. Three 1-D pore zeolites (VET, TON, CFI) that possess cylinder-like 1-D channels with hydrophobic internal walls composed of Si and O only were studied, as well as three widely studied 3-D pore zeolites (MFI, LTA, FAU), which have three-dimensionally connected pores and cages in the frameworks. We only considered zeolites with pore sizes that are sufficiently small to exclude Na^+ and Cl^- ions through molecular-sieving.

All pores in the 1-D pore zeolites considered are large enough to be accessible by water, and according to crystallographic data (Freyhardt et al., 1996, Baerlocher and McCusker, 2015), the pores for VET and CFI are cylindrical with an effective diameter of 5.9 and 7.2 Å, respectively, whereas TON has slightly elliptic pores with dimensions 4.6 × 5.7 Å. The unit cells of the 1-D pore zeolites were taken from the crystallographic database (Baerlocher and McCusker, 2015). The unit cell of VET consists of 17 Si and 34 O atoms with orthogonal lattice vectors with lengths (a × b × c) 13.048 × 13.048 × 4.948 Å. The TON unit cell has orthogonal lattice vectors with lengths 14.105 × 17.842 × 5.256 Å and is composed of 24 Si and 48 O. The unit cell of CFI has orthogonal lattice vectors with lengths, 13.961 × 5.264 × 25.967 Å and there are 32 Si and 64 O. The 1-D channels in the VET and TON are aligned with c lattice vector, while CFI possesses 1-D pores in the direction of the b lattice vector. In our results below we consider the pores to be aligned with the *z*-axis (so the *x*, *y* and *z* axes are parallel to the *a*, *b* and *c* lattice vector in VET and TON; and the *x*, *y* and *z* axis parallel to the *a*, *c* and *b* lattice vectors in CFI). Each simulation box was composed of 2 × 2 crystallographic unit cells in the x and y directions and 28, 21 and 14 unit cells in the *z*-direction for VET, TON and CIF, respectively (see Figure 5-1). The accessible volumes for the water molecules are 78.2, 80.4, 133.8 $Å^3$/1000 $Å^3$, respectively for VET, TON and CFI.

MFI has straight channels parallel to the y-axis with dimensions 5.1 × 5.5 Å which are perpendicular to channels whose centres zigzag in the x-direction, and with dimension 5.3 × 5.6 Å. LTA has 4.1 Å pores in all three directions that are connected by cavities with diameters of about 11 Å. FAU possesses larger pores (7.4 Å) with cavities of similar size to those in LTA. Interestingly, the FAU cylindrical channels cross diagonally at 45° to the *xy*-, *yz*- and *xz*- planes of unit cell. The simulation cell for MFI was built from 2 × 2 × 3 unit cells (40.180 × 39.476 × 39.426 Å) in *x*, *y*, *z*-coordinates, LTA was of 3 × 3 × 3 unit cells (35.757 × 35.757 × 35.757 Å), and FAU was of 2 × 2 × 2 unit cells (48.690 × 48.690 × 48.690 Å). The simulation boxes for the 3-D pore zeolites considered here have angles of 90° between all lattice vectors. The details of the zeolites studied here are summarised in Table 5-1 and Figure 5-1.

An equilibration simulation was carried out on empty frameworks at a constant pressure and temperature (NPT) of 300 K and 1 atm in order to check the stability of the zeolite structures and confirm the suitability of the choice of force fields.

Table 5-1 Details of zeolite candidates for desalination membranes (Baerlocher and McCusker, 2015, First et al., 2011)

Channel	Framework	Name	Chemical formula	LCD[a] (Å)	PLD[b] (Å)
3-D	MFI	Silicalite-1	$[Si_{96}O_{192}]$	6.3	4.4
	LTA	ZK-4	$[Si_{24}O_{48}]$	11.0	4.2
	FAU	Zeolite Y	$[Si_{192}O_{384}]$	11.2	7.3
1-D	VET	VPI-8	$[Si_{17}O_{34}]$	6.4	5.9
	TON	Theta-1	$[Si_{24}O_{48}]$	5.7	5.1
	CFI	CIT-5	$[Si_{32}O_{64}]$	7.4	7.2

[a] Largest cavity diameter: size of the largest sphere that can fit at some position in the pore

[b] Pore limiting diameter: size of the largest sphere that can pass through the pore

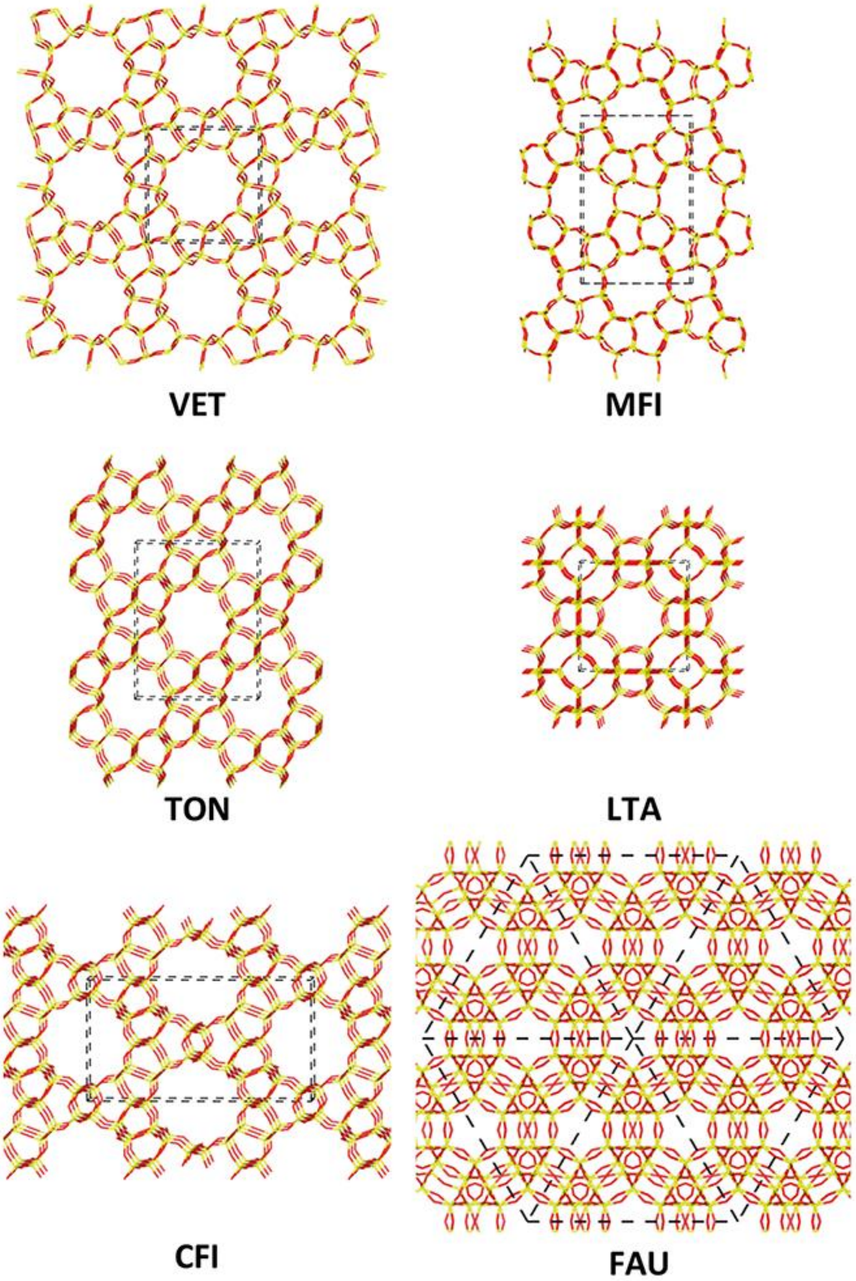

Figure 5-1 Zeolite frameworks considered in this work, showing lines between silicon (yellow) and oxygen (red) atoms in each case. In each case the structure is oriented to view it along the widest straight pore. For CFI and MFI the view is along the *b* lattice vector, for FAU it is along the (1,1,1) vector and in the other cases it is along the *c* lattice vector. A similar scale is used in each of the figures. 1-D pore zeolites are on the left, and the 3-D pore zeolites are on the right. Unit cells are shown by dashed lines.

The TIP4P-Ew (Horn et al., 2004) force field was used for water as it gives reasonable agreement with experimental data in terms of structure and diffusion coefficients (Cohen-Tanugi and Grossman, 2014, Horn et al., 2005). The water molecule is modelled by three atoms (H, O, H) and one massless charged particle, and the molecule kept rigid using the SHAKE algorithm

(Ryckaert et al., 1977). There is a Lennard-Jones (LJ) intermolecular interaction between the water oxygen atoms and Coulombic potentials between charges on the hydrogen atoms and the massless particle.

To model the interactions between the zeolite atoms and between zeolite-water, the Buckingham potential was used,

$$U(r_{ij}) = A\,exp\left(-\frac{r_{ij}}{\rho}\right) - \frac{C}{r_{ij}^6} \tag{5-1}$$

where A, ρ, and C are constants, r_{ij} is the distance between atoms. The parameters for the zeolite intramolecular interactions used were those determined by Hughes *et al.* (Hughes et al., 2011) who further developed the SiO_2 interatomic potentials (Sanders et al., 1984). For water-zeolite interactions, we used parameters for the interaction of α-quartz with water, which was originally derived by de Leeuw and Parker (de Leeuw and Parker, 1998), then later adjusted by Hughes *et al.* for the zeolite-water potential in order for the better agreement with the binding energy obtained by MP2 ab-initio quantum calculations. A three-body non-bonding harmonic angle potential, with the parameters obtained by Sanders *et al.* (Sanders et al., 1984), was used to maintain the geometry of O-Si-O in the zeolite framework. The particle-particle-particle mesh (PPPM) Ewald sum (Hockney and Eastwood, 1988b) was employed for long ranged Coulombic interactions.

5.3.2 Characterisation of transport and structure of water in zeolites

Water diffusion can be examined by consideration of the self-diffusion coefficient D_s which is indicative of the molecular mobility and the collective diffusion coefficient D_c that is directly related to the transport diffusion coefficient (Gubbins et al., 2011). The transport diffusivity represents the ratio of the flux of molecules in the fluid to a concentration gradient (Smith and Hashemi, 2009), ($J = -D_t \partial C/\partial z$ where J is the flux, D_t is the transport diffusivity, C is the concentration, and z is the position), and is directly related to the collective diffusion coefficient through a thermodynamic factor (Gubbins et al., 2011) ($D_t = 1/(k_B T)\,(\partial\mu/\partial \ln C)_T D_c$ where μ is the chemical potential). Thus, the flux of water through the material and its utility as a membrane can be evaluated by the collective diffusion coefficient. For real world membranes, the flux is driven by a pressure gradient hydrodynamic permeance *K* is one of the most important factors to evaluate the performance of the real world membrane. *K* is a degree of the quantity of the flux under a steady state by the applied pressure, and a proportional factor of the flow rate induced by the pressure gradient. This non-equilibrium-driven permeance is physically correlated to the equilibrium-driven collective diffusion coefficient: $K = (D_c V)/(N k_B T)$ where *V* is the volume of the membrane and *N* is the number of diffusing molecules (Falk et al., 2015). Therefore, the hydrodynamic permeance performance of membranes can be estimated by measuring the collective diffusivity based on equilibrium MD simulations.

Self-diffusion coefficients can be experimentally determined using pulsed field gradient nuclear magnetic resonance (PFG-NMR) (Bussai et al., 2002) and quasi-elastic neutron scattering (QENS) techniques (Jobic et al., 1999, Gubbins et al., 2011). Transport/collective diffusivities in zeolites have also been experimentally measured by QENS (Jobic et al., 1999) and by direct experimental measurements (Kapteijn et al., 1995).

In simulations the diffusion coefficient can be obtained by measuring the mean square displacement (MSD) for each water molecule in the system, and if the motion is diffusive (MSD varies linearly in time) it will be defined by the Einstein relationship:

$$MSD(t) = \frac{1}{N} \lim_{t\to\infty} \langle \sum_{i=1}^{N} |\mathbf{r}_i(t) - \mathbf{r}_i(0)|^2 \rangle = 6D_s t \tag{5-2}$$

where $\mathbf{r}_i(t)$ is the position of the *i*th particle at time *t*, and *N* is the number of molecules in the framework. To calculate the collective diffusion coefficient the MSD of the centre-of-mass (com) of all the water molecules in a pore is computed:

$$MSD_{com}(t) = N_p \lim_{t\to\infty} \langle |\mathbf{r}_{com}(t) - \mathbf{r}_{com}(0)|^2 \rangle = 6D_c t \tag{5-3}$$

where $\mathbf{r}_{com} = 1/N_p \sum_{i=1}^{N_p} \mathbf{r}_i$ and N_p is the number of molecules in the pore.

Water clusters were expected to form in the hydrophobic inner-pores of the zeolites with small to moderate loading as found in our previous work (Han et al., 2015) and experimentally proved by in situ SAXS and in situ XRD (Ohba et al., 2005, Iiyama et al., 2006). In simulations, this phenomenon can be observed through direct visualisation of the water molecules within the framework, and quantitatively characterised by calculating the radial distribution function $g(r)$

$$g(r) = \frac{N_{sh}(r)}{V_{sh}(r)} \times \frac{1}{\rho} \tag{5-4}$$

where N_{sh} is the number of water oxygen atoms in a shell of radius between r and $r + dr$ and volume V_{sh}, centred on a particle of interest, and ρ is the average water number density in the system (i.e. calculated using the total volume of the simulation cell). This is most appropriate for the study of spherically symmetric systems where $g(r)$ reaches 1 when the particles are isotropically distributed. For the systems with 1-D pores that are considered here it is more useful to consider a function which is modified to account for the confinement $g(r)_{\text{1-D}\,pore}$

$$g(r)_{1-D\,pore} = g(r) \times \frac{V_{sh}(r)}{V_{ps}(r)} \times \frac{\rho}{\rho_p} \approx g(r) \times \frac{V_{sh}(r)}{2\pi r_p{}^2 dr} \times \frac{\rho}{\rho_p} \tag{5-5}$$

where V_{ps} is the potential water accessible volume of the pore shell between r and $r + dr$ (the portion of the spherical shell that is in the pore), ρ_p is given as the average particle number density of the whole pore and r_p is the pore radius. Here it is assumed that $V_{ps} \approx 2\pi r_p{}^2 dr$ will be reasonably accurate at larger r ($r > r_p$) and may overestimate $g(r)_{\text{1-D}\,pore}$ at $r \approx r_p$, however since the accessible volume of 1-D pore can only be estimated, this approximation is accepted. Therefore, $g(r)_{1\text{-}D\,pore}$ is expected to have a value of 1 at large r if the molecules are uniformly distributed in the pore. For the 3-D pores, we only calculate the usual distribution function given by equation (5-4).

5.3.3 Simulation procedure

Water molecules were loaded onto each zeolite structure and the energies were minimised. The volume of each system at 300 K and 1 atm was then determined using 1 ns simulations with a 1 fs time step in the isobaric-isothermal (NPT) ensemble with a Nosé–Hoover (NH) barostat and thermostat, and a relaxation time of 1 ps. After relaxation of each system, their properties were determined using thermostatted constant volume (NVT) simulations. A NH thermostat was used to fix the temperature at 300 K, and the properties were calculated over a 2 ns simulation with a time step of 1 fs. Twenty independent runs were performed on each system.

In most cases water molecules were added to the pores of the zeolites to give a densities of 0.39 g cm^{-3} in the accessible pore volume, which corresponds to the loading density of VET zeolite that was considered in our previous study (Han et al., 2015). For the MFI zeolite, this density is obtained with MFI13 (13 water molecules in 2 unit cells) and MFI80 (80 molecules in 12 unit cells). MFI with 16 water molecules in two unit cells (MFI16, 0.47 g cm^{-3}) was also simulated as a reference case to validate our force-field and methodology by comparison with previous work on MFI, since MFI16 at this density has been extensively studied in the past (Joshi et al., 2014, Bussai et al., 2002, Hughes et al., 2011). Table 5-2 gives information on the number of zeolite unit cells and the number of water molecules in the zeolites for each system simulated in the present work. A "System code" is also given in Table 5-2 to allow clear reference to the each of the systems considered in the paper.

Table 5-2 Information on initial setups of simulation

System code	Water density [a] / g cm^{-3}	No. of water molecules	No. of unit cells	Simulation cell size x Å × y Å × z Å
MFI16	0.47	16	1×1×2	20.090×19.738×26.284
MFI13	0.39	13	1×1×2	20.090×19.738×26.284
MFI80	0.39	80	2×2×3	40.180×39.476×39.426
LTA127	0.39	127	3×3×3	35.757×35.757×35.757
FAU411	0.39	411	2×2×2	48.690×48.690×48.690
VET24	0.39	96	2×2×28	26.203×26.203×139.109
TON15	0.39	117	2×2×21	28.210×35.684×110.376
CFI24	0.39	192	2×2×14	27.922×51.934×73.696

[a] *Water density in the accessible volume of the zeolite*

We applied the all-atom model potential described above, and used periodic boundary conditions in three dimensions. All algorithms and calculations employed in this study used the LAMMPS code (Plimpton, 1995, Shinoda et al., 2004, Martyna et al., 1994).

5.4 Results and discussion

5.4.1 Validation work on water diffusion within MFI

We firstly examined water transport in the MFI zeolite with simulation cells composed of 2 unit cells containing 16 water as a reference work, which we referred to as MFI16 system. We then compared these results to MFI13 and MFI80, i.e. 13 water molecules in 2 unit cells and 80 water molecules in 12 cells, respectively, which correspond to the same loading density (0.39 g cm^{-3}) applied to all other zeolites. Mean square displacement (MSD) calculations were used to determine self-diffusion coefficients given by equation (5-2), and their components in each direction. Fickian diffusion takes place when pores are big enough for the guest molecules to pass each other, and when guest-guest and host-guest collisions result in movement in three-dimensions (Gubbins et al., 2011). Anomalous diffusion can arise from confinement of the fluid (Nguyen and Bhatia, 2012). Single-file diffusion is an extreme case which can arise when 1-D pores become small enough to prevent molecules from passing each other (Felderhof, 2009, Alexander and Pincus, 1978). This, in conjunction with smooth pore may result in unusually high fluxes.

In our systems, Fickian diffusion was always observed due to the width of the pores and the simulation conditions. As shown in Figure 5-2, MFI has straight cylindrical channels lying along y-direction, and channels that zigzag along the *x*-direction. There are no open pores in the *z*-direction lying in the *xy* plane, however due to the connectivity of the pores (see Figure 5-2) diffusion in the *z*-direction can still occur. Therefore, water diffusion in the *z*-direction only has a contribution to the overall MSD at short timescales. The MSD in the y-direction is higher than that the *x*-direction. This tendency was observed in all MFI systems studied here irrespective of the water loading and simulation cell size, as indicated in Table 5-3.

Results for the reference case (MFI16) are similar those in the literature for each component of the self-diffusion coefficient, however we note that there is a large variation in published results for both experimental and computational studies. Global water self-diffusion coefficients of ~1.00 to 1.91 × 10^{-9} $\mathrm{m}^2\ \mathrm{s}^{-1}$ have been reported in experimental (Caro et al., 1986, Bussai et al., 2002) and recent computational studies (Arı et al., 2009, Hughes et al., 2011, Joshi et al., 2014). The MD calculated self-diffusion coefficients in the *x*-direction were ca. 0.69 – 2.60 × 10^{-9} m^2 s^{-1}, *y*-direction had a range of 1.24 – 6.50 × 10^{-9} m^2 s^{-1}, and the range in the *z*-direction is ~0.79 × 10^{-9} m^2 s^{-1} (Bussai et al., 2002, Arı et al., 2009, Hughes et al., 2011). These diffusion coefficients are comparable to our global D_s (0.88 ± 0.08 × 10^{-9} m^2 s^{-1}) and its components (D_{sx}: 0.93 ± 0.11 × 10^{-9} m^2 s^{-1}, D_{sy}: 1.51 ± 0.11 × 10^{-9} m^2 s^{-1}, D_{sz}: 0.20 ± 0.02 × 10^{-9} m^2 s^{-1}).

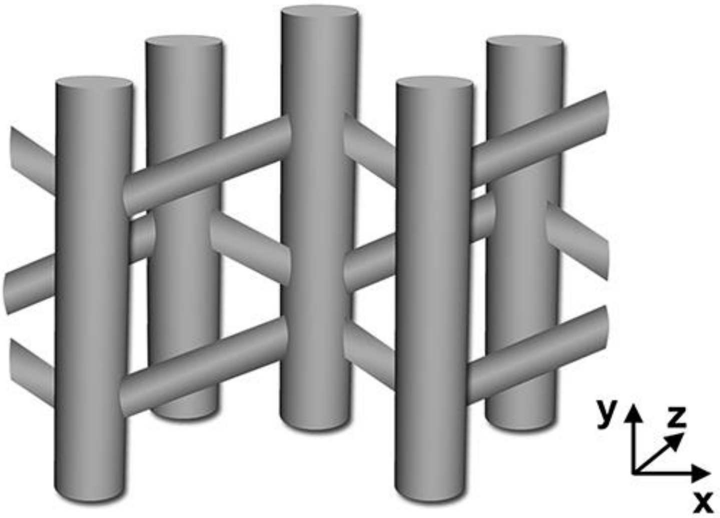

Figure 5-2 Schematic drawing of the channel system of MFI zeolite.

Table 5-3 Self-diffusion coefficients for water in MFI zeolite with different loadings and different simulation cell size [a]

	Water density [b] / g cm^{-3}	D_{sx} / 10^{-9} m^2 s^{-1}	D_{sy} / 10^{-9} m^2 s^{-1}	D_{sz} / 10^{-9} m^2 s^{-1}	D_s / 10^{-9} m^2 s^{-1}
MFI16 [c]	0.47	0.93 ± 0.11	1.51 ± 0.11	0.20 ± 0.02	0.88 ± 0.08
MFI13 [d]	0.39	1.31 ± 0.13	1.60 ± 0.12	0.23 ± 0.02	1.05 ± 0.09
MFI80 [e]	0.39	1.13 ± 0.05	1.36 ± 0.05	0.34 ± 0.01	0.94 ± 0.04

[a] *The error bars are the standard error of the mean for the diffusion coefficient calculated from 20 independent runs*

[b] *Water density in the accessible volume of the zeolite*

[c] *16 water molecules in 2 unit cells; MFI-type*

[d] *13 water molecules in 2 unit cells; MFI-type*

[e] *80 water molecules in 12 unit cells; MFI-type*

Measurements of the diffusion coefficients were also made for MFI13 (13 water molecules in a simulation cell consisting of 1×1×2 unit cells) and MFI80 (80 water molecules in the simulation cell) which has a similar loading to MFI13, but is extended six-fold (2×2×3 unit cells). As summarised in Table 5-3, these two cases share the same water loading (0.39 g cm^{-3}), however the larger system has slightly lower diffusion coefficients due to the possibility for formation of larger water clusters (Han et al., 2015). The fact that the diffusion coefficient only changes by a very small amount indicates that the system size is sufficient. The diffusion coefficients in MFI16 are slightly lower which is consistent with it having a slightly higher density (0.47 g cm^{-3}).

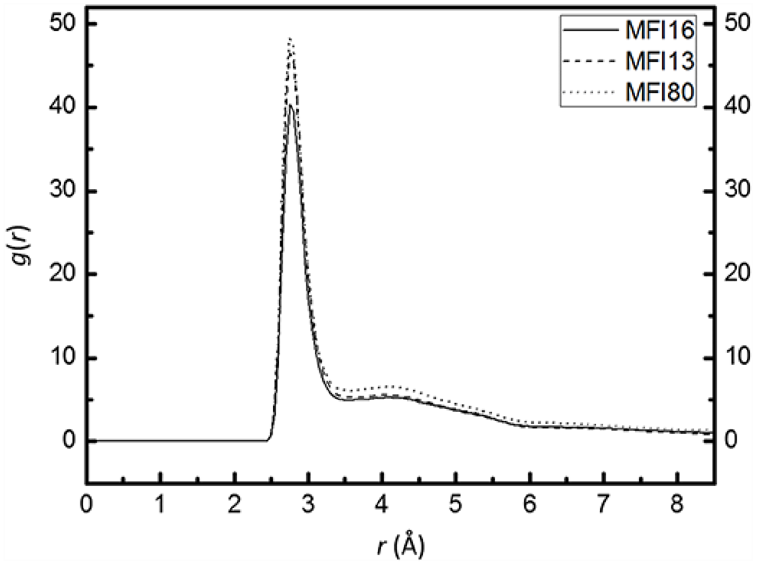

Figure 5-3 The radial distribution function, $g(r)$, for oxygen atoms of the water molecules in MFI with various loadings.

To assist in characterizing the structural properties of water confined in MFI, we calculated the radial distribution function (RDF). For the 3-D pore systems, $g(r)$ given by equation (5-4) was evaluated for the oxygen atoms of water, and the density in (5-4) for MFI16, MFI13 and MFI80 is 1.54×10^{-3} g cm^{-3}, 1.25×10^{-3} g cm^{-3} and 1.28×10^{-3} g cm^{-3}, respectively. As displayed in Figure 5-3, a sharp, high peak is observed at about 2.8 Å for MFI16, MFI13 and MFI80 and the general features are the same in all cases. This is similar to the results obtained previously (Hughes et al., 2011, Bussai et al., 2003). The positions of the characteristic peaks corresponded well with those obtained for the oxygen-oxygen $g(r)$ of liquid TIP4P-Ew (Horn et al., 2004, Hughes et al., 2011). The reduction in the height of the peaks in the RDF curve for MFI16 is consistent with the clusters of water molecules in all systems having the same density since calculation of $g(r)$ using equation (5-4) uses the density of the water in the system, which will be higher in the case of MFI16. In addition there is a cross-over in $g(r)$ for MFI13 and MFI16 suggesting that the water clusters might be a little larger in the higher density MFI16 case. We also note that the pore radius of MFI (ca. 2.6 Å) prevents formation of spherical water clusters because the first shell of a spherical cluster has a radius of about 3.4 Å.

The number of water molecules in the first shell was obtained by integrating N_{sh} over the first peak (to 3.4 Å). All three samples showed nearly identical numbers of water molecules present in this shell (3.4 − 3.6 molecules). These results therefore show that the structural and transport properties of MFI can be described using simulations and indicate that our selected force field and simulation parameters give results that are consistent with those published.

5.4.2 Properties of water in zeolites with 3-D pore channels

Similar studies were carried out on two widely used zeolites, LTA and FAU. Both frameworks have been of practical interest and possess 3-D pore channels. Nevertheless, little research has been carried out on water diffusivity and the structure of the water in these systems.

The LTA framework is built with alternate arrangements of double 4-rings (*d4r*) and sodalite (*sod*) cages, forming open structures with 4.1 Å-diameter pore openings and 11 Å-diameter cavities while FAU has alternate double 6-rings (*d6r*) and *sod* units, creating 7.4 Å-diameter pores and 12 Å-diameter cavities. Both zeolites were loaded with water molecules in their inner frameworks with the same density (0.39 g cm^{-3}) as MFI80 (corresponding to 127 and 411 molecules for LTA and FAU, respectively). As shown in Figures 5-4 and 5-5, water molecules tend to be within the cavities in both zeolites most of the time, although a few molecules occasionally hop to a neighbouring cavity. This implies that water prefers to form clusters at moderate density when confined, as shown in previous studies (Iiyama et al., 2006, Ohba et al., 2005, Ohba and Kaneko, 2009) and the cavity-trapped particles rarely diffuse out to other cavities due to the high energy barrier generated by the small opening between the cavities, and the need for the clusters to change shape or break up.

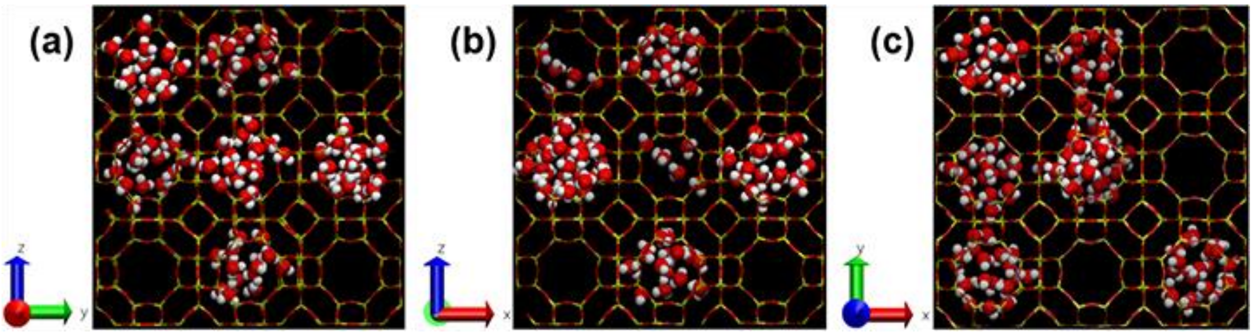

Figure 5-4 Snapshots from the simulation of water within the LTA-type zeolite (water represented by ball-and-sticks and zeolites by wires, oxygen coloured in red, hydrogen in white, and silicon in yellow): views along the (a) *x*-axis, (b) *y*-axis, and (c) *z*-axis.

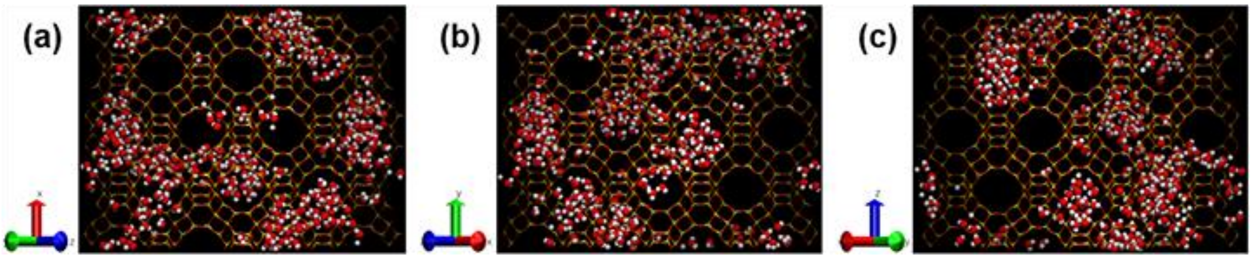

Figure 5-5 Snapshots from the simulation of water within FAU-type zeolite (water represented by ball-and-sticks and zeolites by wires, oxygen coloured in red, hydrogen in white, and silicon in yellow): views after rotation by 45° clockwise about the (a) *x*-axis, (b) *y*-axis, and (c) *z*-axis.

Consistent with these observations, water self-diffusivity in the cage-containing zeolites were noticeably lower than in the cylinder-containing zeolite, MFI. (see Table 5-4) Unlike in MFI, the pores lying along the *x*, *y* and *z* directions are identical so the *x*-, *y*-, and *z*-components of the diffusion coefficient are the same. For LTA, which has a narrower pore entrance, D_s was found to be about 5 times lower ($0.19 \pm 0.02 \times 10^{-9}$ m^2 s^{-1}) than in MFI for the given density, whereas FAU has a D_s that is more than double that of LTA. Although water molecules in FAU move to and from neighbouring cavities more freely than in LTA due to a wider opening (7.4 Å), the D_s ($0.43 \pm 0.01 \times 10^{-9}$ m^2 s^{-1}) is also lower than that in MFI. This suggests that the shape of the zeolite channel might be even more influential on water transport than it size for under these condition since D_s is higher for MFI than for FAU. Although MFI has smaller pores, they are cylindrical.

Table 5-4 Diffusion coefficients for water in the 3-D pore zeolites at the given water density [a]

	Water density [b] / g cm^{-3}		D_x / 10^{-9} m^2 s^{-1}	D_y / 10^{-9} m^2 s^{-1}	D_z / 10^{-9} m^2 s^{-1}	Diffusion coefficient / 10^{-9} m^2 s^{-1}
MFI80 [c]	0.39	D_s	1.13 ± 0.05	1.36 ± 0.05	0.34 ± 0.01	0.94 ± 0.04
		D_c	3.07 ± 0.46	3.58 ± 0.70	0.77 ± 0.08	2.47 ± 0.41
LTA127 [d]	0.39	D_s	0.20 ± 0.01	0.19 ± 0.01	0.19 ± 0.02	0.19 ± 0.02
		D_c	0.27 ± 0.06	0.26 ± 0.04	0.27 ± 0.05	0.27 ± 0.05
FAU411 [e]	0.39	D_s	0.44 ± 0.02	0.43 ± 0.01	0.43 ± 0.01	0.43 ± 0.01
		D_c	1.09 ± 0.19	1.04 ± 0.13	1.14 ± 0.15	1.09 ± 0.16

[a] *The error bars are the standard error of the mean for the diffusion coefficient calculated from 20 independent runs*

[b] *Water density in the accessible volume of the zeolite*

[c] *80 water molecules in 12 unit cells; MFI-type*

[d] *127 water molecules in 27 unit cells; LTA-type*

[e] *411 water molecules in 8 unit cells; FAU-type*

The values of D_c are also shown in Table 5-4. It is observed that D_c for MFI (cylindrical pore), is more than twice that of the zeolites with cages, i.e. LTA and FAU. This also indicates that the flux of water tends to depend on the geometry of the pore as well as the pore size since FAU has wider pores (opening: 7.4 Å, cavity: 11.0 Å in diameter) than MFI. FAU has a larger D_c (1.09×10^{-9} m^2 s^{-1}) than LTA (0.27×10^{-9} m^2 s^{-1}), which is consistent with its larger D_s. MFI has different directional collective diffusion coefficients due to the asymmetric alignment of pores in each direction. As shown in the self-diffusion for MFI, the *z*-component of the collective diffusivity has the lowest value (0.77×10^{-9} m^2 s^{-1}), and the global coefficient is 2.47×10^{-9} m^2 s^{-1} which is far higher than those obtained in LTA and FAU. The collective and self-diffusion coefficients become equal when the motions of the molecules can be considered independent. It can be seen that they are more similar in LTA than in MFI and FAU. In addition, the enhancement in LTA is not as much as that of MFI. From these trends, we conclude that the collective movement of water in framework channels is largely influenced by the geometry and size of pores, indicating a cylindrical structure and larger size may be more favourable for the collective motion.

For FAU, the orientation of the pores in the *xy* plane and the lattice vectors of the unit cell are not perpendicular to each other, but are at 45°. However, due to the symmetry of the unit cell, the components of the diffusion coefficient in the directions along the pores are equal to those along the *x*, *y*, *z* axes.

Figure 5-6 compares RDF for the water oxygen atoms in the 3-D pore zeolites. LTA and FAU show very similar peak positions, and a slightly more distinct peak at 4.2 Å (second hydration layer) than is observed in MFI where this feature appears as a shoulder to the first peak. This might be because in LTA and FAU there are cages that are large enough for water molecules to form 3-D clusters. The position of the highest peak at 2.8 Å in all cases implies there is a well-formed first shell, and is also in good agreement with the observed position of the first peak for bulk water (Horn et al., 2004). The differences in peak height is partly due to the differences in the proportion of the simulation cells that can be filled with water. Although the density of water in the pores is the same in all cases, the density used in equation (5-4) is the density of water in the simulation cell, so will be different in each case. Using data in Table 5-2, these densities are 0.038 g cm^{-3}, 0.083 g cm^{-3}, and 0.106 g cm^{-3} for MFI, LTA, and FAU, respectively. This fact also results in a large difference in peak heights between the bulk and confined water (Horn et al., 2004).

The number of water molecules within 3.4 Å of each other was determined to be 4.3 for FAU, 4.2 for LTA and 3.6 for MFI. This also suggests that zeolites with cages have a more favourable environment for formation of stable tetrahedral water clusters.

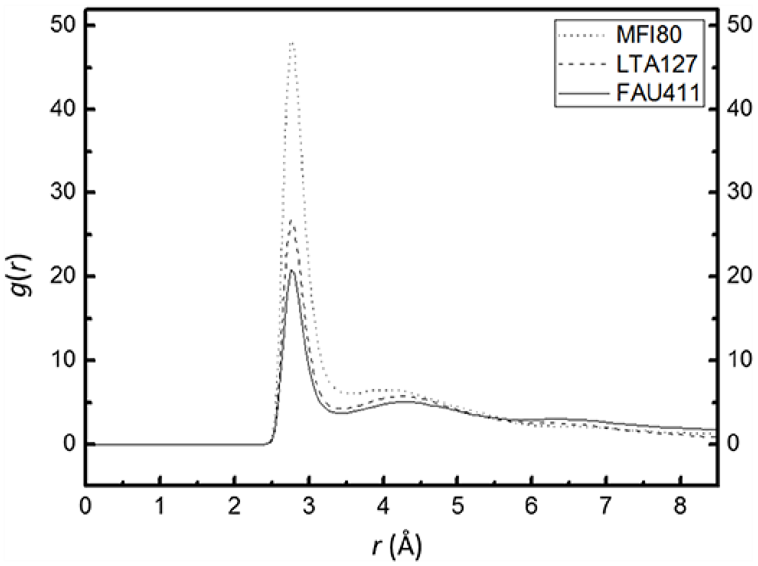

Figure 5-6 Radial distribution function, $g(r)$, for oxygen atoms of the water molecules in the 3-D pore zeolites with the same water density within the pore.

5.4.3 Properties of water in zeolites with 1-D pore channels

Several studies have previously considered zeolites with 1-D channels (Hughes et al., 2011, Han et al., 2015, Bushuev and Sastre, 2011), however in order to compare the results with those obtained for the 3-D pores, we have carried out additional calculations to obtain results with loadings of 0.39 g cm^{-3} in each case.

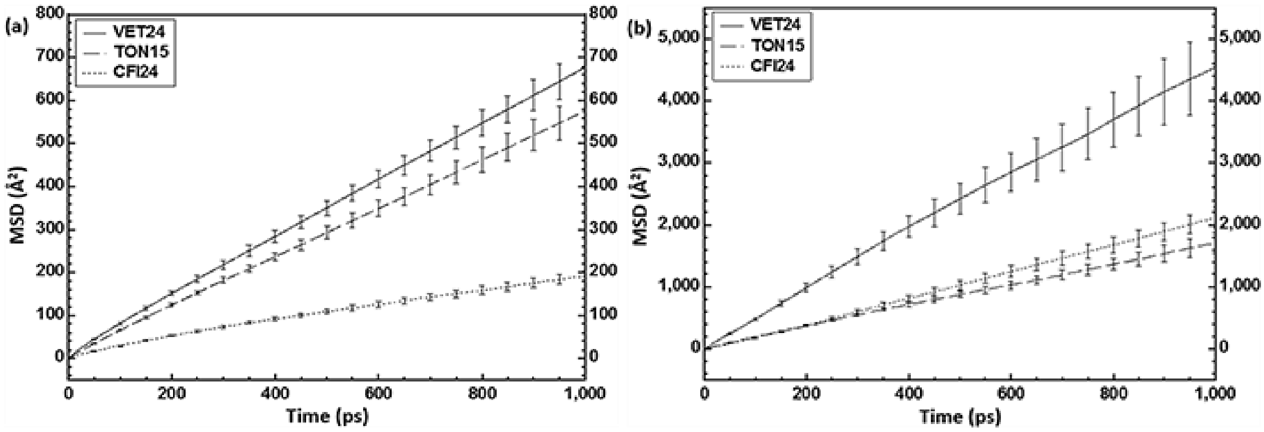

Figure 5-7 MSD of the (a) molecules of water and (b) centre-of-mass of the water in VET, TON, and CFI zeolites.

Figure 5-7 shows single molecule MSD and centre-of-mass MSD plots versus time obtained for VET, TON, and CFI zeolites. All MSD trajectories showed the Fickian diffusive behaviour. We note that, as expected by (Han et al., 2015), molecular displacement in directions other than the channel orientation makes little contribution to the MSD. The self- and collective diffusion coefficients determined using equations (5-2) and (5-3), respectively, and are presented in Table 5-5.

Table 5-5 Component of the diffusion coefficients in the pore direction for water in 1-D pore zeolites at the given water density [a]

	Effective diameter / Å	Water density [b] / g cm^{-3}	$D_{s,z}$ / 10^{-9} m^2 s^{-1}	$D_{c,z}$ / 10^{-9} m^2 s^{-1}
VET24 [c]	5.9	0.39	3.45 ± 0.22	23.36 ± 3.24
TON15 [d]	4.6 × 5.7	0.39	2.90 ± 0.21	8.61 ± 0.83
CFI24 [e]	7.2	0.39	1.02 ± 0.06	10.44 ± 0.83

[a] *The error bars are the standard error of the mean for the diffusion coefficient calculated from 20 independent runs*

[b] *Water density in the accessible volume of the zeolite*

[c] *24 water molecules per channel in a simulation cell of length 28 unit cells; VET-type zeolite*

[d] *15 water molecules per channel in a simulation cell of length 21 unit cells; TON-type zeolite*

[e] *24 water molecules per channel in a simulation cell of length 14 unit cells; CFI-type zeolite*

Comparing the results in Table 5-5 and those in Table 5-4, it can be seen that the self-diffusivities for water in the *z*-direction in the 1-D channels were up to 18-times higher than the largest component of the values in three-dimensional channels for the same loading density, and all the results for the 1-D channels considered were higher than any of the 3-D results. CFI and MFI had similar values for the maximal components of the self-diffusion coefficient, (approximately 1.0×10^{-9} m^2 s^{-1}) but the collective diffusion coefficient in the direction along the pore for CFI is around 3-times higher than the collective diffusion in the y-direction for MFI. The total collective diffusion coefficient (i.e. averaged over the three directions), is still larger in CFI than in MFI, although the corresponding self-diffusion coefficient is lower. This indicates that the shape and dimensionality of pores significantly influence the dynamics of water in the pores; the cylindrical, 1-D channels have the largest diffusion coefficients along the pores. The fact that MFI, with its cylindrical channels, had the highest D_s and D_c of the 3-D pore zeolites also supports that finding. Overall, the 1-D pores lead to enhanced water movement due to the one-directed and well-defined pathway and a relatively smooth potential energy surface along the pores. This smooth energy landscape of the inner pores leads to Fickian diffusion in the long term, after a short-term (ca. 10 ps) ballistic diffusion (Nguyen and Bhatia, 2012). Also, the confinement results in formation of water clusters, even at the low loadings, and thus water molecules diffuse like a part of the stable cluster on timescales that are large (>10 ps) compared to the vibrations of the molecules, in accordance with the previous reports (Iiyama et al., 2006, Ohba et al., 2005, Han et al., 2015, Nguyen and Bhatia, 2012).

The dynamics and structure of water clusters in a slit-pore are also influenced by the slit width (Ohba and Kaneko, 2009). For the given water density, VET was found to have the highest diffusion coefficient ($D_{c,z}$ = 23.36 × 10^{-9} m^2 s^{-1}), while TON had the lowest ($D_{c,z}$ = 8.61 × 10^{-9} m^2 s^{-1}). Although CFI has the largest pore (largest LCD and PLD) its collective diffusion is lower than that of VET, and higher than that of TON. This tendency may be due to the size and shape of the water cluster and the intermolecular interaction between zeolite-water and water-water. It is thought that with a 3 Å radius, the VET pore allows formation of small stable water clusters at low loading, however all water molecules have contact with the zeolite walls so the zeolite-water interaction has a dominant influence on the diffusion. However, CFI has bigger pores in which water molecules are able to form larger clusters in a specified area, and water-water interactions become more common. In TON, the smaller, elliptic pores resulted in formation of chains of single water molecules, so again the zeolite-water interaction dominates. Thus, despite the existence of the smaller pore in TON than in CFI, the collective diffusivities for TON and CFI are similar to each other. We propose that this is due to a balance between the pore size, cluster shape and dominant interaction potentials.

In comparison with the results obtained for the 3-D pore zeolites, the component of the collective diffusivity along the pore of TON was about 2.5-times higher than that of the largest component for MFI (3.58 × 10^{-9} m^2 s^{-1}) which has the largest diffusion coefficients of the 3-D candidates considered here. The value of $D_{c,z}$ for VET is more than one order of magnitude greater than the components of D_c for LTA, which had the lowest diffusion coefficient of the 3-D pore zeolites. Due to these findings, it is expected that zeolites with 1-D cylinder-type pores are very promising as high flux membranes since the cylindrical pore directs water droplets to flow in one-direction, if it is possible to orient them so that the pores are normal to the required direction of flow.

Figure 5-8 also demonstrates the different distributions of water clusters in the 1-D pore zeolites. Multiple ordered-structures of water occurred in a channel of VET, whereas in TON there are several single-file-like assemblies across a channel. The zeolite with the widest pore, CFI, resulted in formation of larger clusters containing more water molecules.

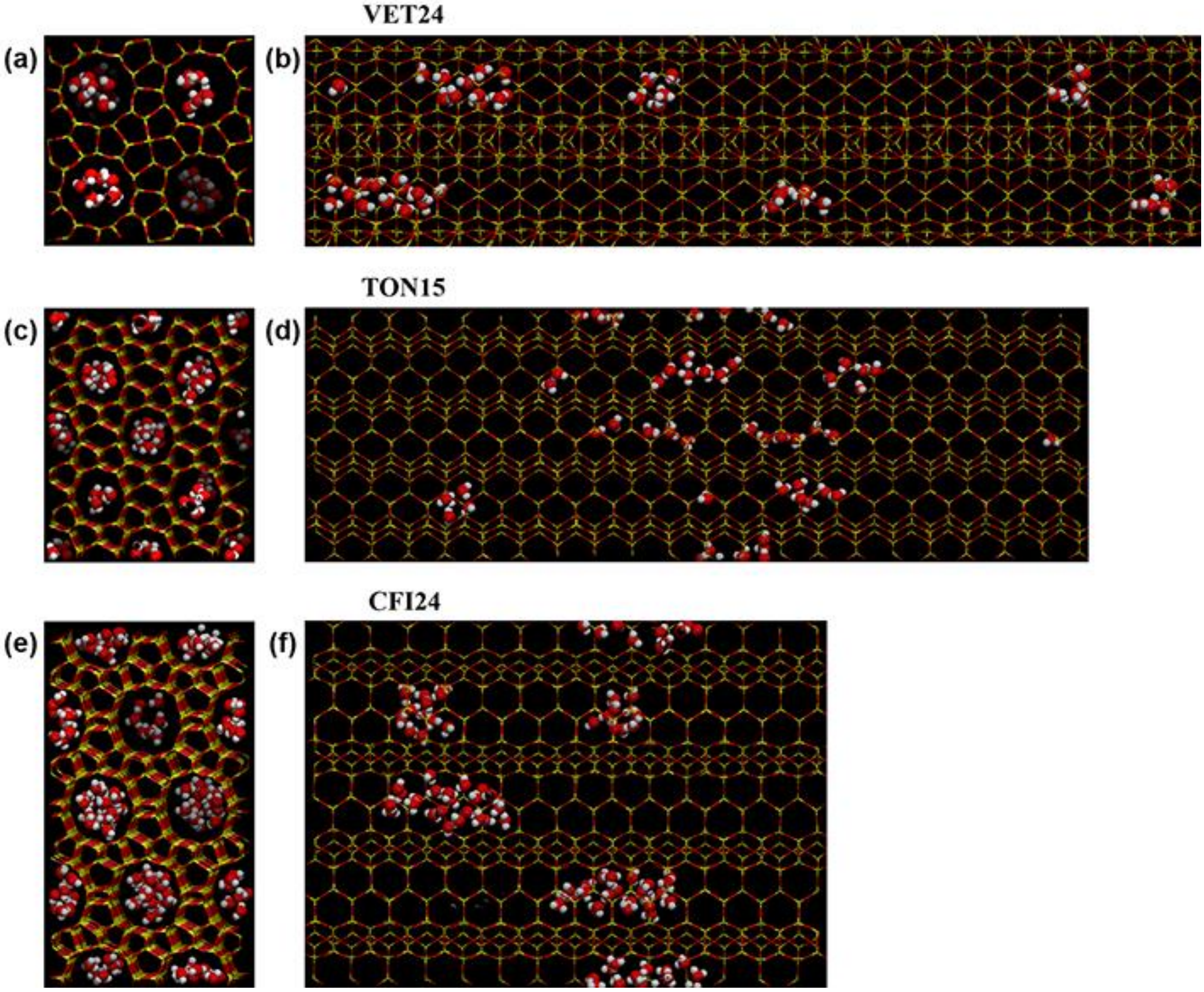

Figure 5-8 Snapshots: (a) top view of the pores along the *z*-axis and (b) side view of the pore channels along the *x*-axis taken from the VET24 simulation, (c) top view of the pores along the *z*-axis and (d) side view of the pore channels along the *x*-axis taken from the TON15 simulation, (e) top view of the pores along the *y*-axis and (f) the side view of the pore channels along the *x*-axis taken from the CFI24 simulation. All *x*-, *y*-, *z*-directions are in periodic boundary condition. (Water represented by ball-and-sticks and zeolites by wires, oxygen coloured in red, hydrogen in white, silicon in yellow, water molecules only in the front pores are shown in (b), (d), (f) for better visualisation)

To quantify the distribution of water confined in the 1-D pore zeolites, the normalised RDF, $g(r)_{\text{1-D } pore}$, given by equation (5-5) was calculated. In Figure 5-9, the RDF curves showed clearly different characteristics depending on the pore size and shape of the three 1-D pore zeolites. All three frameworks indicated the presence of a first hydration shell characterised by a sharp peak at 2.8 Å. However, the characteristics of the second peak differ. VET has a clear broad peak at around 4.3 Å for the second shell of the cluster indicative of tetrahedral bonding, then the peak significantly drops and becomes flat after 6 Å. TON has a shoulder to the first sharp peak, then the shoulder drops quite gradually and flattens out at 6 Å, suggesting a lack of tetrahedral structure in TON as also seen in Figure 5-8. CFI shows a second peak at around 4.6 Å which is slightly shifted to higher values of *r* and is broader than that of VET. The first and second peaks are also more similar in height, however we note that using the definition in (5-5), when *r* is smaller than the pore diameter the peak height is underestimated. The RDT suggests that in CFI, the water forms larger clusters than in VET and the water within the cluster behaves more like bulk water than in other 1-D pore zeolites.

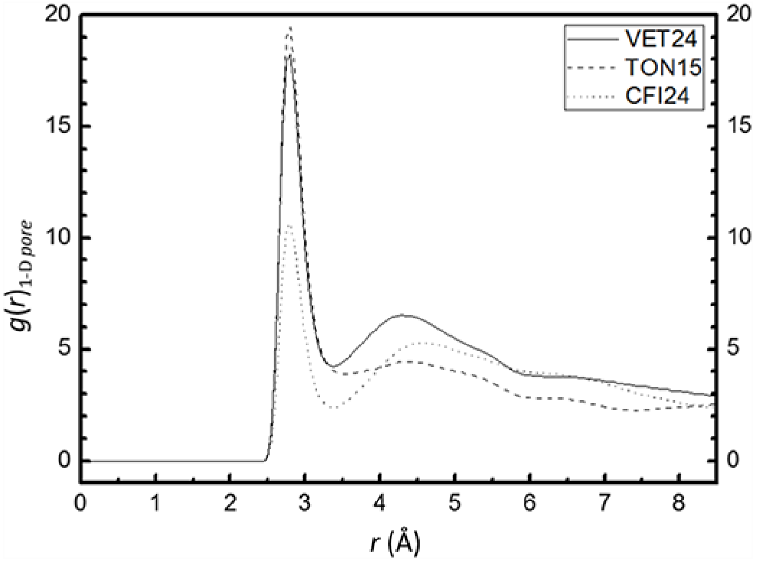

Figure 5-9 The normalised radial distribution function, $g(r)_{\text{1-D } pore}$, for oxygen atoms of the water molecules in the 1-D pore zeolites with the same water density.

5.5 Conclusions

In this work, diffusion coefficients and structural properties of water inside zeolites were studied using MD simulations. The methodology adopted for this study were validated by comparison with both computational and experimental data for water diffusion in MFI-type zeolite.

Zeolites with 3-D pore channels (MFI, LTA, and FAU) were investigated, and the water diffusion coefficients and the structure of water within them were determined. The water loading densities were chosen to be 0.39 g cm^{-3}. MFI was found to have a higher self-diffusion coefficient than LTA and FAU which seems to be associated with the MFI having straight cylindrical pore channels perpendicular to zigzag cylindrical channels, while the latter ones both have spherical-like cages where water molecules can be trapped. Self-diffusion coefficients were 0.94×10^{-9} m^2 s^{-1}, 0.19×10^{-9} m^2 s^{-1}, and 0.43×10^{-9} m^2 s^{-1} for MFI, LTA, and FAU, respectively. The ordering of structures of water in LTA and FAU displayed the first and second hydration shells more clearly than in MFI due to the cages in LTA and FAU which were sufficiently large to hold clusters and molecules.

The 1-D pore zeolites (VET, TON, and CFI) had components of the self-diffusion coefficients in the direction of the pore up to 18-times higher than the largest components of the self-diffusion coefficients determined for the 3-D pore zeolites. However, CFI, the larger pore, showed a comparable diffusion coefficient to MFI (ca. 1.0×10^{-9} m^2 s^{-1}). The collective diffusivity was also determined by measuring centre-of-mass MSDs for both 3-D and 1-D pore zeolites. The range of the component of the collective diffusion coefficients parallel to the pore was from 8.6×10^{-9} m^2 s^{-1} to 23.4×10^{-9} m^2 s^{-1} for 1-D pore zeolites. That is, the collective diffusion coefficient is around one order of magnitude larger than those of the 3-D pore zeolites (0.3×10^{-9} m^2 s^{-1} to 3.6×10^{-9} m^2 s^{-1}). The results obtained suggest that the hydrophobic cylindrically-shaped pore significantly enhances the water transport in one-direction. These indicates that the 1-D pore zeolites are very promising as high flux membranes, if manufacturing methods can be developed to produce large membranes with the pores parallel to the water flow. However, the enhancement in the diffusion coefficient is sufficiently large that even if the zeolites were randomly oriented, the 1-D pore zeolites could be preferable to the 3-D pore zeolites. We note that we have not taken entrance effects into account in this paper and that is currently under investigation.

The structure of water in 1-D pore zeolites varied depending on the size and shape of pores. VET with about 6 Å-diameter cylinders had clearer four-coordinate molecules in a pore than the smaller and elliptical pore in TON. The largest pores, which were considered in CFI, had water structures more typical of bulk water.

References

ALEXANDER, S. & PINCUS, P. 1978. Diffusion of labeled particles on one-dimensional chains. *Physical Review B,* 18**,** 2011-2012.

ALEXIADIS, A. & KASSINOS, S. 2008. Molecular Simulation of Water in Carbon Nanotubes. *Chemical Reviews,* 108**,** 5014-5034.

Arı, M. U., AHUNBAY, M. G., YURTSEVER, M. & ERDEM-ŞENATALAR, A. 2009. Molecular Dynamics Simulation of Water Diffusion in MFI-Type Zeolites. *Journal of Physical Chemistry B,* 113**,** 8073-8079.

BAERLOCHER, Ch. & MCCUSKER, L. B. 2015. *Database of Zeolite Structures* [Online]. http://www.iza-structure.org/databases/, IZA-SC. Available: http://www.iza-structure.org/databases/ [Accessed 15 Sep 2016].

BUSHUEV, Y. G. & SASTRE, G. 2011. Atomistic Simulation of Water Intrusion–Extrusion in ITQ-4 (IFR) and ZSM-22 (TON): The Role of Silanol Defects. *The Journal of Physical Chemistry C,* 115**,** 21942-21953.

BUSSAI, C., FRITZSCHE, S., HABERLANDT, R. & HANNONGBUA, S. 2003. Formation of Low-Density Water Clusters in the Silicalite-1 Cage: A Molecular Dynamics Study. *The Journal of Physical Chemistry B,* 107**,** 12444-12450.

BUSSAI, C., VASENKOV, S., LIU, H., BÖHLMANN, W., FRITZSCHE, S., HANNONGBUA, S., HABERLANDT, R. & KÄRGER, J. 2002. On the diffusion of water in silicalite-1: MD simulations using ab initio fitted potential and PFG NMR measurements. *Applied Catalysis A: General,* 232**,** 59-66.

CARO, J., HŎCEVAR, S., KÄRGER, J. & RIEKERT, L. 1986. Intracrystalline self-diffusion of H2O and CH4 in ZSM-5 zeolites. *Zeolites,* 6**,** 213-216.

COHEN-TANUGI, D. & GROSSMAN, J. C. 2012. Water Desalination across Nanoporous Graphene. *Nano Letters,* 12**,** 3602-3608.

COHEN-TANUGI, D. & GROSSMAN, J. C. 2014. Water permeability of nanoporous graphene at realistic pressures for reverse osmosis desalination. *The Journal of Chemical Physics,* 141**,** 074704.

CORRY, B. 2011. Water and ion transport through functionalised carbon nanotubes: implications for desalination technology. *Energy & Environmental Science,* 4**,** 751-759.

DE LEEUW, N. H. & PARKER, S. C. 1998. Molecular-dynamics simulation of MgO surfaces in liquid water using a shell-model potential for water. *Physical Review B,* 58**,** 13901-13908.

DEMONTIS, P., GULÍN-GONZÁLEZ, J., JOBIC, H., MASIA, M., SALE, R. & SUFFRITTI, G. B. 2008. Dynamical Properties of Confined Water Nanoclusters: Simulation Study of Hydrated Zeolite NaA: Structural and Vibrational Properties. *ACS Nano,* 2**,** 1603-1614.

DING, M., GHOUFI, A. & SZYMCZYK, A. 2014a. Molecular simulations of polyamide reverse osmosis membranes. *Desalination,* 343**,** 48-53.

DING, M., SZYMCZYK, A., GOUJON, F., SOLDERA, A. & GHOUFI, A. 2014b. Structure and dynamics of water confined in a polyamide reverse-osmosis membrane: A molecular-simulation study. *Journal of Membrane Science,* 458**,** 236-244.

DONG, J., XU, Z., YANG, S., MURAD, S. & HINKLE, K. R. 2015. Zeolite membranes for ion separations from aqueous solutions. *Current Opinion in Chemical Engineering,* 8**,** 15-20.

DROBEK, M., YACOU, C., MOTUZAS, J., JULBE, A., DING, L. & DINIZ DA COSTA, J. C. 2012. Long term pervaporation desalination of tubular MFI zeolite membranes. *Journal of Membrane Science,* 415–416**,** 816-823.

FALK, K., COASNE, B., PELLENQ, R., ULM, F.-J. & BOCQUET, L. 2015. Subcontinuum mass transport of condensed hydrocarbons in nanoporous media. *Nature Communications,* 6**,** 6949.

FELDERHOF, B. U. 2009. Fluctuation theory of single-file diffusion. *The Journal of Chemical Physics,* 131**,** 064504.

FIRST, E. L., GOUNARIS, C. E., WEI, J. & FLOUDAS, C. A. 2011. Computational characterization of zeolite porous networks: an automated approach. *Physical Chemistry Chemical Physics,* 13**,** 17339-17358.

FREYHARDT, C. C., LOBO, R. F., KHODABANDEH, S., LEWIS, J. E., TSAPATSIS, M., YOSHIKAWA, M., CAMBLOR, M. A., PAN, M., HELMKAMP, M. M., ZONES, S. I. & DAVIS, M. E. 1996. VPI-8: A High-Silica Molecular Sieve with a Novel "Pinwheel" Building Unit and Its Implications for the Synthesis of Extra-Large Pore Molecular Sieves. *Journal of the American Chemical Society,* 118**,** 7299-7310.

GAI, J.-G., GONG, X.-L., WANG, W.-W., ZHANG, X. & KANG, W.-L. 2014. An ultrafast water transport forward osmosis membrane: porous graphene. *Journal of Materials Chemistry A,* 2**,** 4023-4028.

GUBBINS, K. E., LIU, Y.-C., MOORE, J. D. & PALMER, J. C. 2011. The role of molecular modeling in confined systems: impact and prospects. *Physical Chemistry Chemical Physics,* 13**,** 58-85.

HAN, K. N., BERNARDI, S., WANG, L. & SEARLES, D. J. 2015. Water diffusion in zeolite membranes: Molecular dynamics studies on effects of water loading and thermostat. *Journal of Membrane Science,* 495**,** 322-333.

HOCKNEY, R. W. & EASTWOOD, J. W. 1988b. Particle-Particle-Particle-Mesh (P3M) Algorithms. *Computer simulation using particles.* CRC Press.

HOLT, J. K., PARK, H. G., WANG, Y. M., STADERMANN, M., ARTYUKHIN, A. B., GRIGOROPOULOS, C. P., NOY, A. & BAKAJIN, O. 2006. Fast mass transport through sub-2-nanometer carbon nanotubes. *Science,* 312**,** 1034-1037.

HORN, H. W., SWOPE, W. C. & PITERA, J. W. 2005. Characterization of the TIP4P-Ew water model: vapor pressure and boiling point. *Journal of Chemical Physics,* 123**,** 194504.

HORN, H. W., SWOPE, W. C., PITERA, J. W., MADURA, J. D., DICK, T. J., HURA, G. L. & HEAD-GORDON, T. 2004. Development of an improved four-site water model for biomolecular simulations: TIP4P-Ew. *Journal of Chemical Physics,* 120**,** 9665-9678.

HUGHES, Z. E., CARRINGTON, L. A., RAITERI, P. & GALE, J. D. 2011. A Computational Investigation into the Suitability of Purely Siliceous Zeolites as Reverse Osmosis Membranes. *The Journal of Physical Chemistry C,* 115**,** 4063-4075.

HUGHES, Z. E. & GALE, J. D. 2010. A computational investigation of the properties of a reverse osmosis membrane. *Journal of Materials Chemistry,* 20**,** 7788-7799.

HUGHES, Z. E. & GALE, J. D. 2012. Molecular dynamics simulations of the interactions of potential foulant molecules and a reverse osmosis membrane. *Journal of Materials Chemistry,* 22**,** 175-184.

IIYAMA, T., ARAGAKI, R., URUSHIBARA, T. & OZEKI, S. 2006. Direct Determination of the Intermolecular Structure of the Adsorbed Phase Using *in situ* X-Ray Diffraction and Reverse Monte Carlo Methods. *Adsorption Science & Technology,* 24**,** 815-821.

JOBIC, H., KÄRGER, J. & BÉE, M. 1999. Simultaneous Measurement of Self- and Transport Diffusivities in Zeolites. *Physical Review Letters,* 82**,** 4260-4263.

JOSHI, K. L., PSOFOGIANNAKIS, G., VAN DUIN, A. C. T. & RAMAN, S. 2014. Reactive molecular simulations of protonation of water clusters and depletion of acidity in H-ZSM-5 zeolite. *Physical Chemistry Chemical Physics,* 16**,** 18433-18441.

KAPTEIJN, F., BAKKER, W. J. W., ZHENG, G., POPPE, J. & MOULIJN, J. A. 1995. Permeation and separation of light hydrocarbons through a silicalite-1 membrane: Application of the generalized Maxwell-Stefan equations. *The Chemical Engineering Journal and the Biochemical Engineering Journal,* 57**,** 145-153.

KAZEMIMOGHADAM, M. 2010. New nanopore zeolite membranes for water treatment. *Desalination,* 251**,** 176-180.

LIN, J. & MURAD, S. 2001. A computer simulation study of the separation of aqueous solutions using thin zeolite membranes. *Molecular Physics,* 99**,** 1175-1181.

LIU, Y. & CHEN, X. 2013. High permeability and salt rejection reverse osmosis by a zeolite nano-membrane. *Physical Chemistry Chemical Physics,* 15**,** 6817-6824.

MARTYNA, G. J., TOBIAS, D. J. & KLEIN, M. L. 1994. Constant pressure molecular dynamics algorithms. *The Journal of Chemical Physics,* 101**,** 4177-4189.

MURAD, S. & LIN, J. 2001. Using Thin Zeolite Membranes and External Electric Fields To Separate Supercritical Aqueous Electrolyte Solutions. *Industrial & Engineering Chemistry Research,* 41**,** 1076-1083.

NGUYEN, T. X. & BHATIA, S. K. 2012. Some Anomalies in the Self-Diffusion of Water in Disordered Carbons. *The Journal of Physical Chemistry C,* 116**,** 3667-3676.

OHBA, T. & KANEKO, K. 2009. Initial filling mechanism of predominant water adsorption on hydrophobic slit-shaped carbon nanopores. *Journal of Physics: Conference Series,* 177**,** 012001.

OHBA, T., KANOH, H. & KANEKO, K. 2005. Water cluster growth in hydrophobic solid nanospaces. *Chemistry - A European Journal,* 11**,** 4890-4894.

PLIMPTON, S. J. 1995. Fast Parallel Algorithms for Short-Range Molecular Dynamics. *Journal of Computational Physics,* 117**,** 1-19.RIMER, J. D. 2012. Zeolite compositions and methods for tailoring zeolite crystal habits with growth modifiers. *US20120202006 A1*.

RIMER, J. D., KUMAR, M., LI, R., LUPULESCU, A. I. & OLEKSIAK, M. D. 2014. Tailoring the physicochemical properties of zeolite catalysts. *Catalysis Science & Technology,* 4**,** 3762-3771.

RYCKAERT, J.-P., CICCOTTI, G. & BERENDSEN, H. J. C. 1977. Numerical integration of the cartesian equations of motion of a system with constraints: molecular dynamics of n-alkanes. *Journal of Computational Physics,* 23**,** 327-341.

SANDERS, M. J., LESLIE, M. & CATLOW, C. R. A. 1984. Interatomic potentials for SiO2. *Journal of the Chemical Society, Chemical Communications*, 1271-1273.

SHINODA, W., SHIGA, M. & MIKAMI, M. 2004. Rapid estimation of elastic constants by molecular dynamics simulation under constant stress. *Physical Review B,* 69, 134103.

SMITH, W. F. & HASHEMI, J. 2009. *Foundations of Materials Science and Engineering,* London, UK, McGraw-Hill.

WANG, L., DUMONT, R. S. & DICKSON, J. M. 2013. Nonequilibrium molecular dynamics simulation of pressure-driven water transport through modified CNT membranes. *Journal of Chemical Physics,* 138.

WENTEN, I. G. & KHOIRUDDIN 2016. Reverse osmosis applications: Prospect and challenges. *Desalination,* 391, 112-125.

ZHU, B., DOHERTY, C. M., HU, X. R., HILL, A. J., ZOU, L. D., LIN, Y. S. & DUKE, M. 2013. Designing hierarchical porous features of ZSM-5 zeolites via Si/Al ratio and their dynamic behavior in seawater ion complexes. *Microporous and Mesoporous Materials,* 173, 78-85.

Chapter 6 Potential of Mean Force for Understanding Water and Ion Transport across Zeolite Membranes

6.1 Background

In previous chapters (see Chapter 4 and 5), we have studied water transport and structure within different geometries of zeolite. Thus, it has been shown how the size and shape of zeolite pores influence the motion of the confined water molecules. These results have given some important criteria to select zeolites with a favourable inner geometry for fast water diffusion. However, from a practical viewpoint, it is important to consider the effects of the pore entrance and its functional groups on water/ion transport, since it is necessary to determine if these molecules and ions are likely to enter the pores from the bulk solution. This chapter outlines several previous works relevant to our purpose, theoretical concepts behind the method, and our results and discussion on water/ion transport through zeolite membranes.

MD simulations have considered water and/or ion transport in nanochannels of various materials for application as desalination membranes. Corry examined carbon nanotubes (CNTs) as the membranes by studying water and ions passing through CNT pores of different size ranging from 1.6 to 3.8 Å in effective radius (Corry, 2008). In order to evaluate the barrier for water and ions entering pores in a series of CNTs studied (i.e. (5,5), (6,6), (7,7), and (8,8)), he calculated the potential of mean force (PMF) for a representative particle, either water or ions, which was drawn from bulk solution into the centre of the pore along a trajectory path. It was shown that there is no large energy barrier to water permeation in all CNTs considered except the CNT with smallest pore (5,5) that requires 3.3 kJ mol^{-1}. In contrast, sodium ion transport showed significant differences in the energy barrier ranging from ca. 2.1 to 96.2 kJ mol^{-1} for the widest to the narrowest pore. In later work, Cory extended his studies on use of CNTs for desalination (Corry, 2011). The membranes were composed of a bundle of (8,8) CNTs with four different functional groups added to their top rim. PMF results showed Na^+ entrance to the pores requires far higher energy when there are cationic functional groups at CNT pore mouth (i.e. functionalised with four NH_3^+) than for the pristine CNT, while Cl^- entering anionically-functionalised pores (i.e. functionalised with eight COO^- or four COO^-) required slightly higher energy than for the pristine CNT. CNT functionalised with –OH groups resulted in lower water permeation, but higher Na^+ ion flux under a hydrostatic pressure when functionalised with four –OH groups compared to the non-functionalised pores. This was explained by the electrostatic attraction that was introduced between the groups and water, while the functional groups assisted Na^+ penetration. However, both water and sodium ion fluxes were suppressed with increasing the number of –OH groups at the pore entrance, which was proposed to be due mainly to the increased steric hindrance. Another CNT study was performed by Beu who investigated a series of CNTs with wider pores than those studied by Corry for potential membrane technology (Beu, 2010). The CNTs examined were the (8,8) to (12,12) CNTs, ranging from 3.8 to 6.5 Å in effective radius. Unlike the membranes mentioned earlier, single-channel membranes were employed here with two graphene layers positioned on each pore entrance, and these were immersed in NaCl and NaI aqueous solutions. In the work, PMF profiles for water and salt ions transport were calculated from the average position probabilities $\langle P(\mathbf{r})\rangle$ of each component of the solutions in (8,8) and (10,10) CNTs, showing that Cl^- and I^- faced relatively high energy barriers around 21 kJ mol^{-1} to enter the (8,8) pore compared to 13 kJ mol^{-1} for Na^+ whereas all the ions experienced similar energy barriers around 8.4 kJ mol^{-1} to enter the (10,10) pore of 5.1 Å. Therefore, it is clear from these studies that pore size, pore functional group, and ion type are critical influencers of water and ion permeation through CNTs.

More recently, Richards *et al*. systematically studied anions crossing idealised model pores, defined by Lennard-Jones (LJ) interactions, with effective radius sizes from 2.5 to 6.5 Å in consideration of the transport mechanism of the anions dissolved in drinking water (Richards et al., 2012a, Richards et al., 2012b). They showed free energy profiles of each ion (F^-, Cl^-, NO_2^-, NO_3^-) passing through one-dimensional pores as functions of pore size and ion type by calculating the PMF. Since these ions are surrounded by water molecules in aqueous solution (hydration), energy barriers were examined for each ion in three pore size regimes: Regime 1 is the range of pore sizes where the ion can be inserted with the full first hydration shell; Regime 2 considers pore sizes between the naked ion size and the hydrated ion size; Regime 3 is the pore size smaller than the size of the bare ion. It was found that the free energy barrier for each ion entering the pores drops with increasing the effective pore size. In particular, the energy barrier declined significantly when the ion transport occurs in Regime 1 relative to in Regime 2 for fluoride and chloride, whereas in Regime 2 relative to in Regime 3 for nitrate and nitrite. This can be explained by the fact that partial dehydration occurring in Regime 2 requires higher energy for F^- and Cl^- than for NO_3^- and NO_2^- because F^- and Cl^- ions are bound more tightly to their neighbouring waters. This phenomenon was also confirmed by consideration of PMF calculations for a given pore of radius 3.3 Å. All the ions studied belong to Regime 2 (partial dehydration occurring) in this pore, and it was found that the free energy barriers were 114.6, 89.1, 46.4, and 27.2 kJ mol^{-1} for F^-, Cl^-, NO_2^-, and NO_3^-, respectively. This work gives us atomic-level insight into the dynamical and structural mechanism for the entrance of anions and the surrounding water molecules when into the pores of various size.

Despite the possibility that zeolites could be use as membranes for separation and purification technology, relatively little work has been done on these materials, and only a few types of zeolite have been considered in depth (MFI, LTA, and FAU). Transport of water and dissolved salt into zeolites of various types has been rarely explored. Hughes *et al.* employed a free energy perturbation (FEP) method (Chipot and Pohorille, 2007), to calculate the free energy difference (Hughes et al., 2011). They evaluated the free energy difference for states of hydrated/dehydrated ions, zeolite-trapped/non-trapped bare ions, and hydrated ions inside/outside zeolites. This calculation uses a staging method in which a series of successive states are built between the two states. For example, the free energy of ion dehydration is computed by stripping the surrounding water from the ion of interest by gradually reducing the ion-water interactions, resulting in the full hydration to nothing. Through this process, the study showed Cl^- ions are very unlikely to penetrate the zeolite membrane from bulk solution, while it is relatively likely for Na^+ ions to enter it, according to the FEP result.

The FEP method is an efficient approach for determining the free energy difference ΔA for discrete states of interest. For continuous systems like membranes with bulk solutions in and around them, another approach for computing ΔA, the PMF method, allows profiles using an approximation technique when a particle of interest passes through the membrane from bulk solution.

For this reason, in this chapter a systematic study will be carried out to investigate water and salt ions passing across various zeolite membranes with different pore geometries by means of PMF calculations. By doing this, we are able to discuss differences in free energy profiles between different pore sizes, shapes, and orientations as well as between 3-D pores and 1-D pores of zeolites broadly. Conclusions on the suitability of membranes for desalination will be made from consideration of the dynamical properties of the confined water studied in the previous chapters and energy barriers for entrance of water/ions to the membrane.

6.2 Algorithms and methods

6.2.1 Potential of mean force

To obtain the free energy profiles, we use potential of mean force (PMF) calculations in which we consider a particle permeating along a reaction coordinate passing across from bulk solution through the membrane pores. As mentioned earlier in Chapter 3, the PMF concerns the relative probability that part of the system is fixed at a particular configuration $\boldsymbol{\xi}_1$ and a reference point $\boldsymbol{\xi}_0$ (Roux, 1995). The PMF can be defined by

$$A(\boldsymbol{\xi}_1) = A(\boldsymbol{\xi}_0) - k_B T \ln \frac{P(\boldsymbol{\xi}_1)}{P(\boldsymbol{\xi}_0)} \tag{6-1}$$

where $A(\boldsymbol{\xi}_1)$ is the PMF for the system at the fixed configuration, $\boldsymbol{\xi}_0$ is the reference point, and the probability density is given by $P(\boldsymbol{\xi}_1) = \int e^{-H(\mathbf{r},\mathbf{p})/k_B T}\,\delta(\boldsymbol{\xi} - \boldsymbol{\xi}_1)\, d\mathbf{r}d\mathbf{p} / \int e^{-H(\mathbf{r},\mathbf{p})/k_B T}\, d\mathbf{r}d\mathbf{p}$ where $H(\mathbf{r},\mathbf{p})$ is the total energy of the system as a function of coordinates and momentums of particles (Roux, 1995). k_B is the Boltzmann constant and $\delta(\boldsymbol{\xi} - \boldsymbol{\xi}_1)$ is the Dirac delta function (Arfken et al., 2013). It is generally difficult to measure the PMF directly if some configurations are rarely observed. To obtain a high sampling for some particular configuration of interest, a biasing force is often applied to the system for the required configuration.

In this study, we fix one particle (i.e. water or ion) on the reaction coordinate by using a harmonic potential (U_h) with a large spring constant, which is called the stiff spring method. The reaction coordinate here is defined in the *z*-direction through the centre of one pore of the zeolite membrane, $\boldsymbol{\lambda}$ quantifies the displacement of the particle from the centre of the pore. A point far from the zeolite membrane in the bulk solution ($\boldsymbol{\lambda}_0$) is chosen as the reference point for the 1-particle PMF, thus $A(\boldsymbol{\lambda}_0) = 0$, and the PMF is now approximated by

$$A(\boldsymbol{\lambda}) = -k_B T \ln \int e^{\frac{-[H(\mathbf{r},\mathbf{p}) + U_h(\boldsymbol{\xi},\boldsymbol{\lambda})]}{k_B T}}\, d\mathbf{r}d\mathbf{p}. \tag{6-2}$$

Since in a desalination application, solution molecules are transferred by a trans-membrane pressure gradient, we are interested in exploring the PMF along the reaction coordinate which is perpendicular to the membrane surface. We fix the distance between the centre-of-mass of the membrane and the molecule of interest using the harmonic potentials. Due to symmetric contributions, constraints in *x*- and *y*-directions are zero, and the 1-D PMF can be obtained by integrating over all configurations of the molecule at each specified position $\boldsymbol{\lambda}$ along the 1-D coordinate:

$$\frac{\partial A(\boldsymbol{\lambda})}{\partial \boldsymbol{\lambda}} = -k_B T \frac{\int -\frac{1}{k_B T}\left(\frac{\partial U_h(\boldsymbol{\xi},\boldsymbol{\lambda})}{\partial \boldsymbol{\lambda}}\right) e^{\frac{-[H(\mathbf{r},\mathbf{p})+U_h(\boldsymbol{\xi},\boldsymbol{\lambda})]}{k_B T}} d\mathbf{r}d\mathbf{p}d\boldsymbol{\xi}}{\int e^{\frac{-[H(\mathbf{r},\mathbf{p})+U_h(\boldsymbol{\xi},\boldsymbol{\lambda})]}{k_B T}} d\mathbf{r}d\mathbf{p}d\boldsymbol{\xi}} = \langle \frac{\partial U_h(\boldsymbol{\lambda})}{\partial \boldsymbol{\lambda}} \rangle_{\boldsymbol{\lambda}} \tag{6-3}$$

where $\langle \frac{\partial U_h(\boldsymbol{\lambda})}{\partial \boldsymbol{\lambda}} \rangle_{\boldsymbol{\lambda}}$ is the average $\frac{\partial U_h(\boldsymbol{\lambda})}{\partial \boldsymbol{\lambda}}$ when the stiff spring force is applied to the system of the molecule of interest at $\boldsymbol{\lambda}$. Therefore, the PMF is also given by.

$$A_{\boldsymbol{\lambda}_0 \rightarrow \boldsymbol{\lambda}_1} = \int_{\boldsymbol{\lambda}_0}^{\boldsymbol{\lambda}_1} \langle \frac{\partial U_h(\boldsymbol{\lambda})}{\partial \boldsymbol{\lambda}} \rangle_{\boldsymbol{\lambda}} \, d\boldsymbol{\lambda} \tag{6-4}$$

The free energy profile is now determined by the integration of minus the average forces which are given from the system of the molecule tightly bound at each of the equally spaced positions between $\boldsymbol{\lambda}_0$ and $\boldsymbol{\lambda}_1$ along the reaction coordinate (Hermans and Lentz, 2014). To perform PMF calculations in our MD simulations, we used the harmonic potential with spring force constant of 2.168 eV Å^{-2} (corresponding to 209 kJ mol^{-1} Å^{-2}) to fix the centre-of-mass of a water molecule or an ion for the required configuration in a specified point ($d\boldsymbol{\lambda}$ = 1 Å) along the coordinate. To make a high sampling for the desired configuration under a thermodynamical equilibrium, such large spring constant (i.e. 2.168 eV Å^{-2}, 50 kcal mol^{-1} Å^{-2}) was chosen and strong enough to hold the particle on the desired position with surrounding equilibrium since the particle deviated from the intended position with the lower spring constant. Otherwise, it would take a very long time and be hard to have the high sampling for each configuration along the coordinate.

This approach was used to examine the free energy barrier at points along the reaction coordinate, therefore we can evaluate how thermodynamically favourable movement of the particle (i.e. water or ion) through bulk water, an interface between water and a membrane, and the inner membrane is.

6.2.2 Force fields: Potential parameters

As in the previous chapters of the thesis, the intramolecular potentials of silica zeolites were defined by the Buckingham pair function and the O-Si-O harmonic function parameterised originally by Sanders *et al*., then modified by Hughes *et al*. (Sanders et al., 1984, Hughes et al., 2011). The zeolite-water intermolecular potentials and water potentials were also the same as those selected for the studies in Chapter 4 and 5 (see sections 4.3.3 and 5.3.1). In addition to the force fields used for zeolite bulk system, in this chapter additional potentials need to be taken into account for membrane interaction with the solution. Sodium chloride (NaCl) is the main source of the salt in seawater and brackish water. This is easily dissociated into ions that exist in aqueous solution. Thus, the interaction of the ions with water and the membrane need to be defined. Moreover, in reality the actual silica structure has hydroxyl groups on its surface in which the hydroxyl functionalisation takes place due to defects of the zeolite surface exposed to aqueous environment (Baram and Parker, 1996, Makimura et al., 2010). The bare Si element is four-coordinated and O is two-coordinated. Defects in the silica structure due to cleaving lead to unsaturated Si and O sites which must be saturated with –OH and –H groups, respectively. In this simulation, it was assumed that all zeolite frameworks of interest are ideally structured without inner defects, but outer surfaces of the membrane, after being cleaved to be placed in water, are fully hydroxylated on their uncoordinated sites.

Interatomic potentials of the salt ions were parameterised by the force field based on interactions with TIP4P-Ew water model. This was developed by Joung and Cheatham who modified the AMBER parameters (Joung and Cheatham, 2008, Joung and Cheatham, 2009). The potentials for hydroxylated zeolites were adopted from the studies on SiO_2 nanostructures in aqueous environment in order to obtain the interactions with the aqueous solution (i.e. bulk water and NaCl ions) (Cruz-Chu et al., 2006, de Lara et al., 2015). These potentials for the ions and the hydroxylated zeolites were described by Lennard-Jones (LJ) function (see equation 4-9 in Chapter 4). The Lorentz-Berthelot (LB) mixing rules (Allen and Tildesley, 1987) are applied to combine the LJ potential parameters for determining the interatomic interactions in this complex system. The LB rules are simply defined as: $\varepsilon_{ij} = \sqrt{\varepsilon_{ii}\varepsilon_{jj}}$; $\sigma_{ij} = (\sigma_{ii} + \sigma_{jj})/2$.

Potentials for the hydroxyl groups, functionalising the membrane surfaces, are defined by the force field developed for –OH groups on various oxides (mainly in SiO_2) (Baram and Parker, 1996). The force field used the Morse potential function to describe the bonding between O and H in the hydroxide group:

$$U_{bond}(r_{ij}) = D\left[e^{-2\beta(r_{ij}-r_o)} - 2e^{-\beta(r_{ij}-r_o)}\right] \tag{6-5}$$

where D and β are the parameter constants, and r_0 is the equilibrium distance between O and H in the hydroxyl group. These parameters were originally defined by Saul *et al*. (Saul et al., 1985), then adjusted by Baram and Parker for the oxides (Baram and Parker, 1996).

6.2.3 Zeolite membrane construction and simulation procedure

Crystal structures like zeolites may have many different surface morphologies depending on the direction of crystal growth or crystal cleavage (Greń et al., 2010). To find out the most stable surface (the lowest surface energy), the static lattice energy minimisation is employed to construct zeolite membranes with stable surfaces. The zeolite simulation cells for this test must be built with zero dipole moment by the two region method (Tasker, 1979, Rai, 2012). Two regions of the bulk zeolite are initially constructed with two dimensional periodic condition for the plane of the zeolite surface, leaving the perpendicular direction to the surface non-periodic. A half-sized cell of this bulk is then built in the same way, leaving the cleaved surface of interest non-periodic. The following illustration gives a schematic idea for this approach.

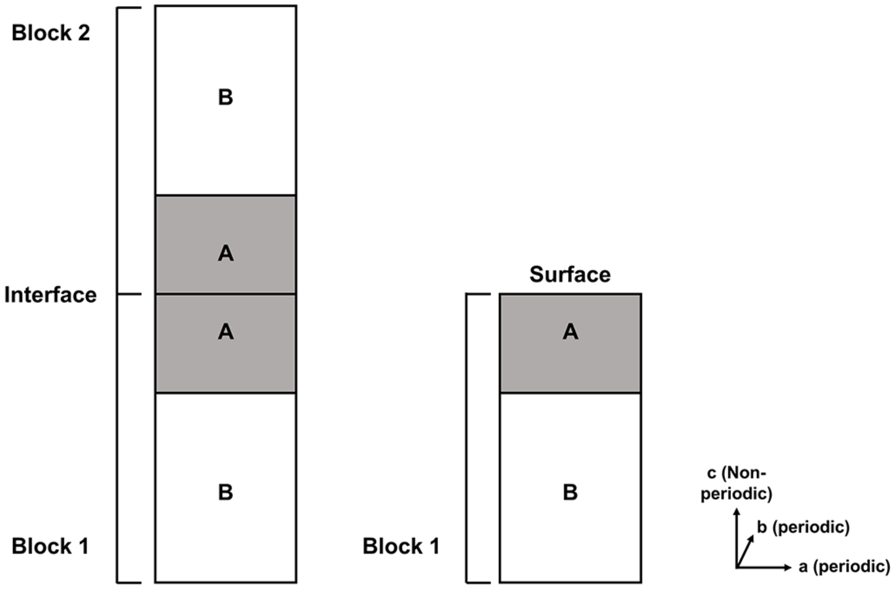

Figure 6-1 A schematic drawing of the two region method for interfaces in the two-block cell (left picture) and surfaces in the single-block cell (right picture). The bulk blocks in *a* and *b* directions are periodic, and in *c* direction are non-periodic.

The single-block cell has the cleaved surface while the two-block cell represents the bulk zeolite. The atoms in region A are explicitly relaxed, but those in region B are kept frozen to their equilibrium position during the minimisation process. The interatomic potentials used for this process are same as those adopted for describing the interactions in the bulk silica zeolite (Hughes et al., 2011).

Through this static lattice minimisation, the surface energy of each cleaved face is evaluated by

$$\gamma = \frac{U_{cs} - \frac{1}{2}U_b}{A} \tag{6-6}$$

where γ is the surface energy, U_{cs} represents the energy of the zeolite block with cleaved surface, and U_b is the energy of the two-block bulk zeolite, and A is the surface area. Since the atoms in region B are held fixed, the interaction energy of all the atoms in region B of the bulk zeolite with all other atoms in region B of the cleaved zeolite is cancelled out in the surface energy calculation (Greń et al., 2010, Rai, 2012). Therefore, the surface energy implies the energy per unit area required to cleave the surface relative to the energy per unit area for the bulk composed of the same number of atoms. The lower surface energy is expected to have a more stable surface.

To construct zeolite membranes, two characteristic types of zeolite framework are selected from the zeolites studied in Chapter 5, in order to study water and ion transport through. LTA has 3-D pores composed of 4.1 Å diameter pore openings that are connected by cavities with diameters of about 11 Å. Depending on facets to be cleaved, this zeolite may exhibit various surface morphologies, resulting in different energy barriers to the molecule of interest. The other zeolite type is VET that has well-defined 1-D cylindrical pores of 5.9 Å diameter. For LTA, we use 27 unit cells (3 × 3 × 3 in *x*, *y*, *z*-coordinates) as an initial cell, and then cleave both sides of *xy* plane to form the most stable surfaces according to the static lattice minimisation process, followed by introduce –OH and –H groups to all the dangling sites of 3-coordinated Si and 1-coordinated O, respectively. For VET, 90 unit cells (3 × 3 × 10) are used as an initial cell, then cleaved and –OH functionalised in the same way without minimisation process, given that VET has only one possible stable surface due to its simple periodic geometry and the fact that the surface of silica is more stable when surface silicon atoms are singly –OH coordinated than those with silicon atoms geminally coordinated (Baram and Parker, 1996, Greń et al., 2010).

Both sides of the membrane surfaces are now filled with water molecules and NaCl ions in a ratio of 809 to 9 (equivalent to 35 g/L, w/v of NaCl/water). This mimics seawater reservoirs around the membrane. The simulation cells we employ for LTA and VET membranes will be shown in the results and discussion section of this chapter.

Energy minimisation is carried out for all the simulated systems before the systems are equilibrated at 300 K and 1 atm using 250 ps simulations with a 0.5 fs time step in NPT ensemble coupled with a Nosé–Hoover (NH) barostat and thermostat, and a relaxation time of 0.5 ps. The PMF profiles for the particle of interest (i.e. a water molecule or an ion) are determined using the stiff spring method while NVT ensemble is applied to the membrane together with NPT to the bulk solution. The target particle at each position, which is equally spaced along the reaction coordinate, is fixed for 250 ps with a 1 fs time step each for an equilibration and production. 20 independent runs were performed for each target particle for each membrane system.

We apply the all-atom model potential described earlier, and use periodic boundary conditions in three dimensions of the simulation system. As in the previous studies of Chapter 4 and 5, long ranged Coulombic interactions are treated by the PPPM Ewald sum (Hockney and Eastwood, 1988b). All algorithms and calculations employed for the study use the LAMMPS code (Shinoda et al., 2004, Martyna et al., 1994).

6.3 Results and discussion

6.3.1 Static lattice energy minimisation

To investigate the stability of possible surfaces of a LTA membrane, energy minimisation simulations have been carried out in this study. The structure of LTA consists of truncated octahedral cages (*sod* cages, also called *β*-cages) and double 4-rings (*d4r*) which are bridges between the *sod* cages. This array of cages and rings makes large cavities which is called *α*-cages. According to previous studies on the surface stability of LTA (Sugiyama et al., 1999, Wakihara et al., 2005, Greń et al., 2010), the single 4-ring (*s4r*)-cleaved surface (see Figure 6-2 (a)) and *d4r*-cleaved surfaces (see Figure 6-2 (b), (c)) were found to be stable. The *s4r* surface refers to one where the surface is constructed from the complete *sod* cages, resulting in *s4r*-terminated pore openings (with *d4r* cleaved in half). The LTA surfaces can be formed with pore openings at the end of the *d4r* (see Figure 6-2 (b)) or the face of *d4r* (see Figure 6-2 (c)). These surfaces are referred to as *d4r*-e and *d4r*-f, respectively. The previous simulation study showed that the *s4r* surface is the most stable according to a static minimisation calculation (Greń et al., 2010), while the *d4r* surfaces were shown to be the most stable surfaces using experimental work (Sugiyama et al., 1999, Wakihara et al., 2005). Thus, we set up 2-block bulk materials with the different surfaces (i.e. *s4r*, *d4r*-e, *d4r*-f), and compare them with their 1-block counterparts using the minimisation method described earlier.

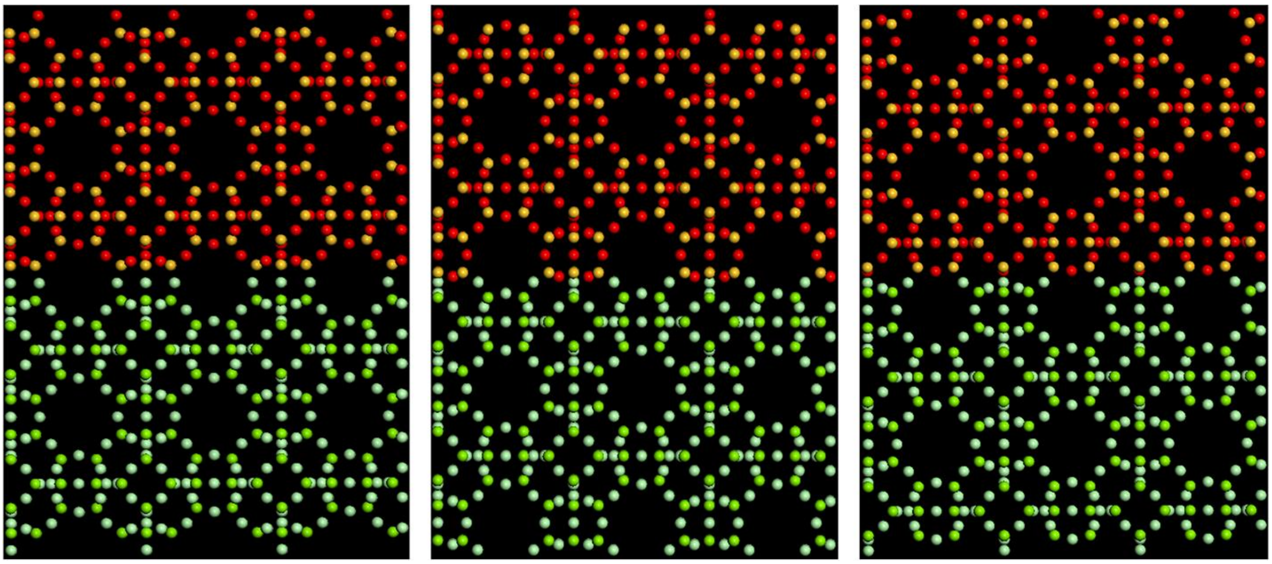

(a) (b) (c)

Figure 6-2 Configurations of 2-block bulk with (a) *s4r* surface, (b) *d4r*-e surface, and (c) *d4r*-f surface. Each image is shown as viewed from above the *xz* plane. The *x*- and *y*-axis are periodic, but the *z*-axis is non-periodic. The bottom layers represent Block 1 and the upper layers represent Block 2. Block 1 can be replicated to build a single-block cell with the cleaved surface. Oxygen atoms are red or light-green coloured and silicon atoms are yellow or green coloured.

Simulations were performed by allowing halves of each block to relax (an upper half of Block 1 and bottom half of Block 2), and holding the other halves fixed at 300 K using a NH-thermostatted NVT ensemble. The surface energies (γ) obtained, according to equation (6-6), are 2.57 J m^{-2}, 2.60 J m^{-2}, and 2.61 J m^{-2} for *s4r*, *d4r*-e, and *d4r*-f, respectively. These values are higher than the literature data (Greń et al., 2010), which are 0.136 J m^{-2}, 0.152 J m^{-2}, and 0.152 J m^{-2} for *s4r*, *d4r*-e, and *d4r*-f, respectively. This may be due to the fact that we carried out these tests at 300 K. This method is often performed at 0 K to prevent the vibrational motions of the block (Rai, 2012), and it is presumed that the literature values were obtained from 0 K simulations. Nevertheless, the trend in our results is consistent with those in the published work.

6.3.2 Potential of mean force

To investigate energy barriers for a molecule penetration into the membrane pores and the free energy changes over a whole trajectory of the molecule passing across the membrane, we chose the potential of mean force (PMF) calculations using the stiff spring method. Unlike the free energy perturbation (FEP) approach (Chipot and Pohorille, 2007), which calculates a series of discrete states where the molecule of interest possibly experiences, the method we described earlier in section 6.2.1 allows study of the continuous states of the molecule passing through zeolite membranes.

Initially, zeolite membrane models were built for the free energy calculations. Two membranes were constructed using LTA (a 3-D pore type) with *s4r* or *d4r*-e surfaces functionalised with –OH groups. Another membrane was constructed using VET, 1-D cylindrical pore type, with the one possible stable surface. Due to the simple periodic geometry of the VET, there is only one type of surface can be the most stable, given that the fact that the surface of silica is more stable when surface silicon atoms are singly –OH coordinated than those with silicon atoms geminally coordinated (Baram and Parker, 1996, Greń et al., 2010). The hydroxyl-functionalised surfaces are shown in Figure 6.3.

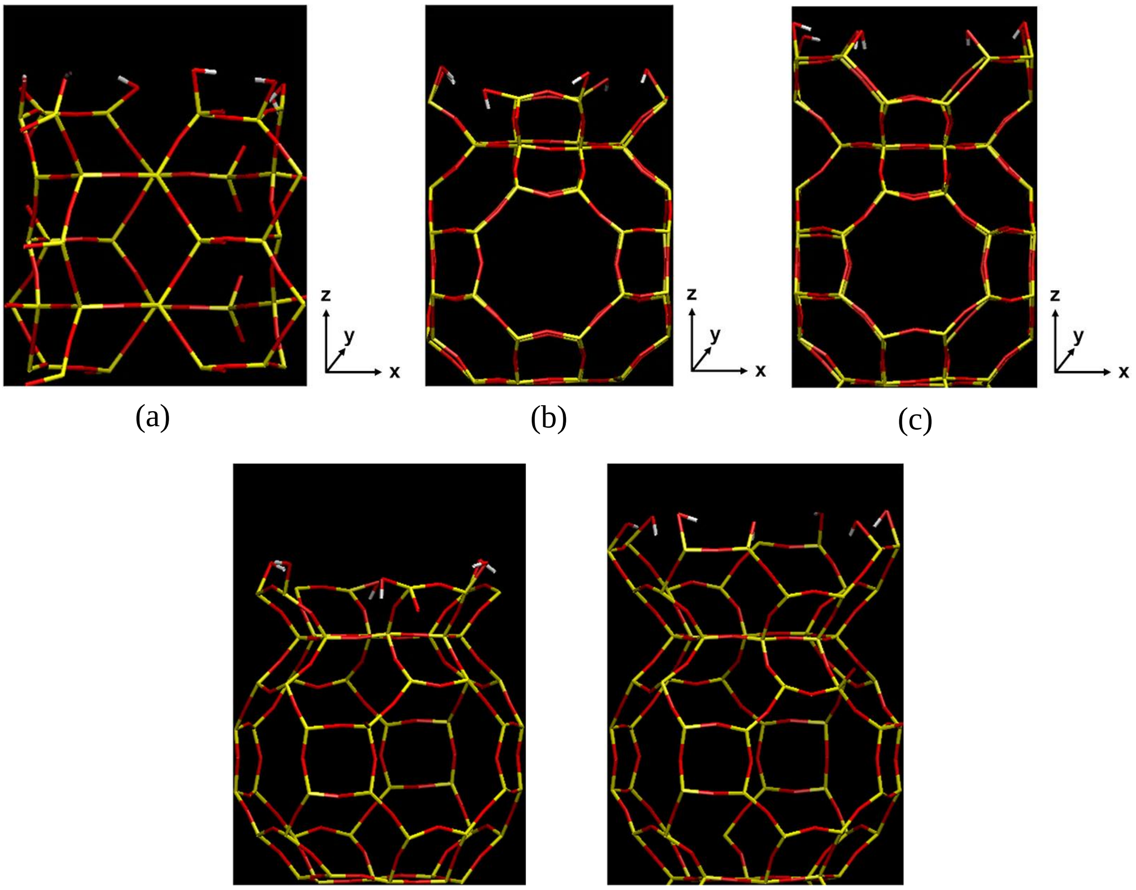

(a) (b) (c)

(d) (e)

Figure 6-3 Molecular structures of repeating unit of (a) VET, (b) LTA with a *d4r*-e surface, and (c) LTA with *s4r* surface. (d) LTA-*d4r*-e and (e) LTA-*s4r* are viewed from the *xz* plane rotated by 30° along the *z*-axis. Silicon atoms are represented as yellow lines, oxygen atoms as red lines and hydrogen atoms as white lines, respectively.

After the addition of –OH groups to the unsaturated surface atoms, simulation cells for each membrane with bulk solution were set up as shown in Figure 6-4.

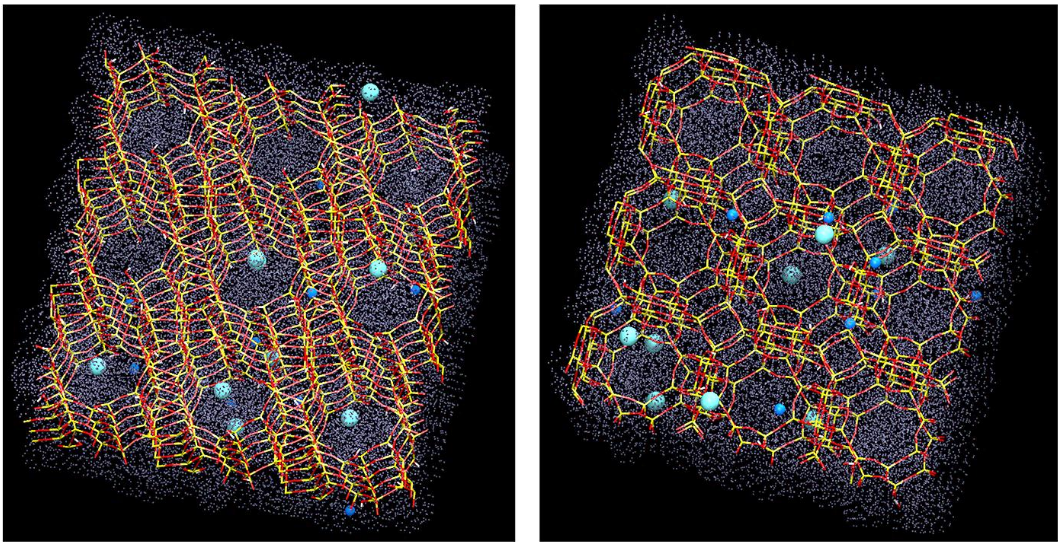
(a) (b)

Figure 6-4 Simulation systems: (a) VET membrane and (b) LTA-*d4r*-e membrane. The zeolite membranes are shown as the same way as in Figure 6.3. Bulk water layers are placed on both top and bottom sides of the membranes, which are represented as transparent white-dotted layers. The light blue-coloured particles (larger) represent chloride ions and the blue particles (smaller) are sodium ions. All the directions of the simulation cells are periodic. A simulation cell for LTA-*s4r* membrane was built as for the VET and LTA-*d4r*-e membranes.

The PMF calculations for all the particles of interest (i.e. water molecule, Na^+ or Cl^- ion) passing through the LTA membrane with each surface were carried out in order to investigate the effect of surface morphology on energy barriers to their entrance and the free energy changes over their full trajectories through the pores. Since all the pores were symmetric in the *z*-direction, we were able to effectively measure the PMF by sampling the trajectory points of data in a symmetrised way.

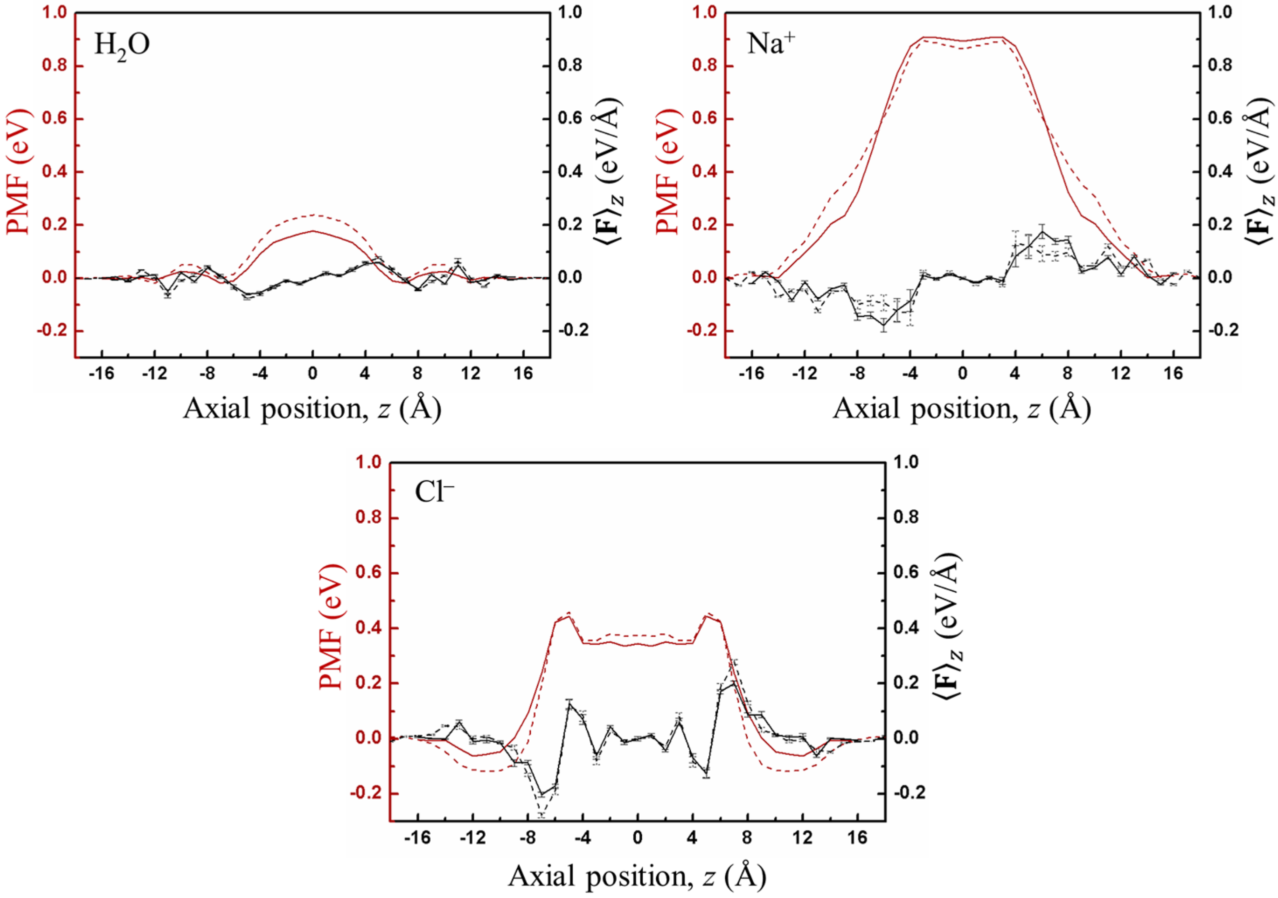

Figure 6-5 PMF (red) and the mean force (black) curves for transport of water and ions. The solid curves are PMF (red) and the mean force (black) for each particle passing through LTA-*d4r*-e membrane and the dashed curves are those for LTA-*s4r* membrane. The mean force was defined by $\langle -\frac{\partial U_h(z)}{\partial z} \rangle_z$ at each position, and sampled in a symmetrised way. The error bar indicates the standard error of the symmetrised sampling at each position.

As shown in Figures 6-3 and 6-4, both LTA membranes have large cages with 8-ring pores as the main entrance for molecular transport. This narrow pore of 4.1 Å diameter is expected to provide a high energy barrier to passage of large molecules. Due to the different terminations of LTA, however the LTA-*d4r*-e has an approximately 4 Å long partial pore before the diameter reaches it minimum size, whereas and the LTA-*s4r* has a 6.5 Å-long pore before it reaches the narrow region (8-ring).

The energy barriers to water or ion entrance and the free energy changes over each regime of the trajectory through LTA-*d4r*-e are qualitatively similar to those obtained from LTA-*s4r* membrane, as shown in Figure 6-5. This is attributed to the same geometry and length of the inner pore which was positioned in a range from about -10 Å to 10 Å. Thus, the qualitative trends in the PMF profiles for each particle of interest in this regime are almost identical to each other.

Chloride ion encounters a high energy barrier of 0.45 eV (43.42 kJ mol^{-1}) to movement into the two LTA membranes from the bulk solution. Hence, it seems unlikely to happen due to the size exclusion effect since the diameter of hydrated Cl^{-} is about 7.6 Å (Richards et al., 2012a). Compared to the Na^{+} barrier, the lower energy barrier for the Cl^{-} entrance can be explained by the fact that the kinetic diameter of the solvated Cl^{-} is smaller, and the Cl^{-} is relatively loosely bound to its solvating water molecules compared to Na^{+} (Hummer et al., 1996, Mancinelli et al., 2007). This can be inferred from the fact that the free energy of Na^{+} solvation is lower than that of Cl^{-} (Hummer et al., 1996), also the water molecules solvating around Na^{+} are more ordered and less influenced by neighbouring environment such as ion concentration than those in the Cl^{-} hydration shell (Mancinelli et al., 2007). This could make it easier to rearrange the water molecules in the hydration shell of Cl^{-} and stabilise the central Cl^{-} by replacing it hydrating water molecules with the surface hydroxyl groups when the Cl^{-} approaches in the vicinity of the pore. But, the energy barrier is still high for the penetration to the centre of the membrane.

In the Cl^{-} PMF curves, wells of 0.06 eV (5.79 kJ mol^{-1}) and 0.11 eV (10.61 kJ mol^{-1}) for the LTA-*d4r*-e and LTA-*s4r* membranes, respectively, appear in the range of -14 Å $< z < -9$ Å and 9 Å $< z <$ 14 Å. They are sufficient for the Cl^{-} to be likely to be trapped in this region at room temperature. This behaviour can also be explained by the properties of Cl^{-} hydration described in the previous paragraph since the chloride ion may be stabilised by the hydroxyl groups functionalised on the surfaces of either LTA-*d4r*-e or LTA-*s4r* membrane. Furthermore, positioning of the Cl^{-} at the pore entrance seems to be more favourable when it stays around the half-cleaved cage pore (LTA-*s4r*) due to the morphology of the pore being able to embrace the hydration shell together with the surface functional groups.

There is some quantitative difference in the PMF for water in the range of -12 Å to -7 Å (and 7 Å to 12 Å). The LTA-*s4r* shows the slightly higher energy barrier (ca. 0.05 eV, 4.82 kJ mol^{-1}) than for the LTA-*d4r*-e (0.025 eV 2.41 kJ mol^{-1}), in these ranges. These energy barriers against water transport from the bulk range ($z < -12$ Å or $z > 12$ Å) can be explained by the geometry of pore vicinity. As mentioned earlier, the LTA-*d4r*-e has the partial pore due to the *d4r* termination, while the LTA-*s4r* has the slightly longer pore due to the half-cleaved cage termination (see Figure 6-3). Hence, this morphological difference results in different energy barriers for the water to overcome. The water entrance to the centre of the α-cages in a range of -7 Å $< z <$ 7 Å will face a higher energy barrier which is about 0.20 eV (19.30 kJ mol^{-1}) when it goes from the pore opening in either LTA-*d4r*-e or LTA-*s4r* membrane. Since the free energy is based on the probability distribution of the molecule of interest (see theories in section 6.2.1), water is less likely to be in the narrow pore

(8-ring, 4.1 Å diameter) than in the bulk, thus energy will be required to transport a water molecule into the pore, even though the effective diameter of a water molecule is smaller (2.75 Å (Zhang and Xu, 1995)) than the pore opening. The high energy barrier seems to be partly attributed to the stabilised Cl^{-} around the pore since it has to be removed for the water molecule to enter the pore. In addition, the hydroxyl functional groups around the surface may enhance the electrostatic attraction to water, which may contribute the high energy barrier. This behaviour can be compared with water entrance to an unfunctionalised pore with similar diameter (e.g. (6,6) CNT with 4.7 Å pore diameter) showing the energy barrier of 1.67 kJ mol^{-1} (Corry, 2008). Nevertheless, the energy barrier for water penetration into the functionalised LTA pore is expected to be overcome due to the high pressure applied in a real RO system (Kumakiri et al., 2000).

The PMF curve for sodium ion transport through either LTA-*d4r*-e or LTA-*s4r* membrane shows that it is highly unlikely for the ion to enter the pore. The sodium ion will experience extremely high energy barrier of about 0.90 eV (86.84 kJ mol^{-1}) in order to approach the centre of the pore in either of the LTA membranes. This seems to stem from the significantly larger diameter of the hydrated Na^{+} (8 Å (Li et al., 2004)) than the narrow inner pore of 4.1 Å. To some extent, this value is comparable to that of sodium ion passage through the (6,6) CNT mentioned earlier because its PMF indicates 69.04 kJ mol^{-1} (Corry, 2008), considering that the CNT pore is slightly larger (4.7 Å). The broader curve appearing in the figure implies that the free energy begins to change when the hydrated Na^{+} becomes close to the extended pore made by the *s4r* termination since the *s4r*-terminated zeolite has the longer pore opening than one with *d4r*-e termination.

Now, we see the free energy profiles for transport of each particle of interest through the VET membrane. These profiles are shown in Figure 6-6.

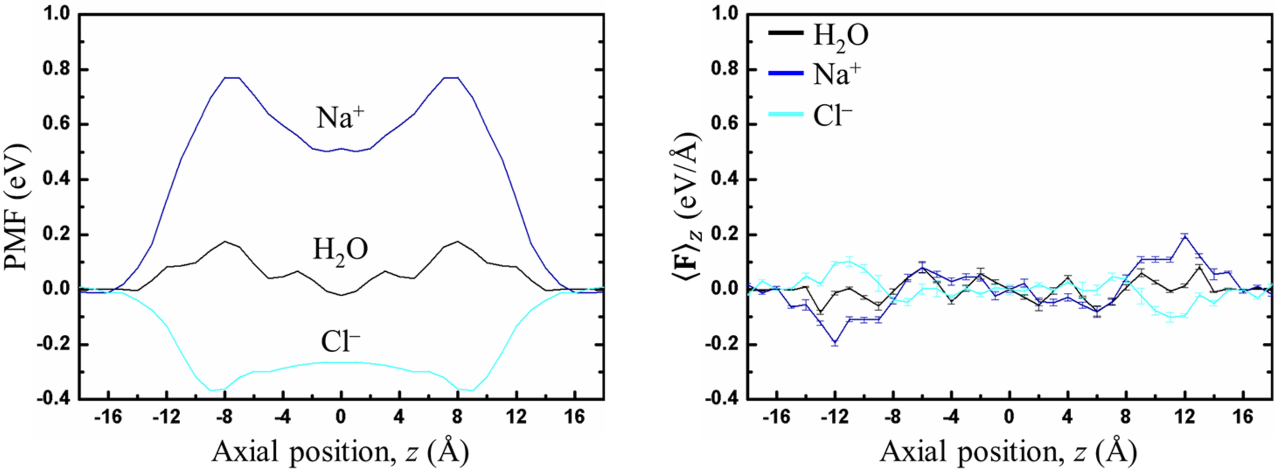

Figure 6-6 PMF and the mean force curves for transport of water (black curve), sodium ion (blue curve), and chloride ion (light-blue curve) across the VET membrane.

The VET membrane we built with the most stable surface has well-defined cylindrical pores with the kinetic diameter of 5.9 Å (see Figure 6-3(a)). This size is expected to be sufficiently large for the water passage, and to effectively block the ion passage.

However, the free energy profile for the chloride ion shows the unusual and unexpected trend as we assumed that the effective diameter of Cl^- is large enough (7.6 Å) to be blocked by the VET pore (5.9 Å). The stabilisation of Cl^- seems to happen just in and out of the pore as the free energy continues to drop until at -9 Å (remember that the pore range is -12 Å $< z <$ 12 Å). The deep well indicates that the Cl^- will be trapped in the pore entrances. This may be explained by the combination effect of the VET pore size and the surface functional groups. The VET pore is relatively large compared to the pore opening in the LTA membranes, thus the size of pore may accommodate the hydrated Cl^- if the hydrating molecules are rearranged. In addition, the surface hydroxyl groups may assist the stabilisation of the Cl^-. The molecular configurations around pores in the VET membrane are shown in Figure 6-7 which provides evidence to support this effect.

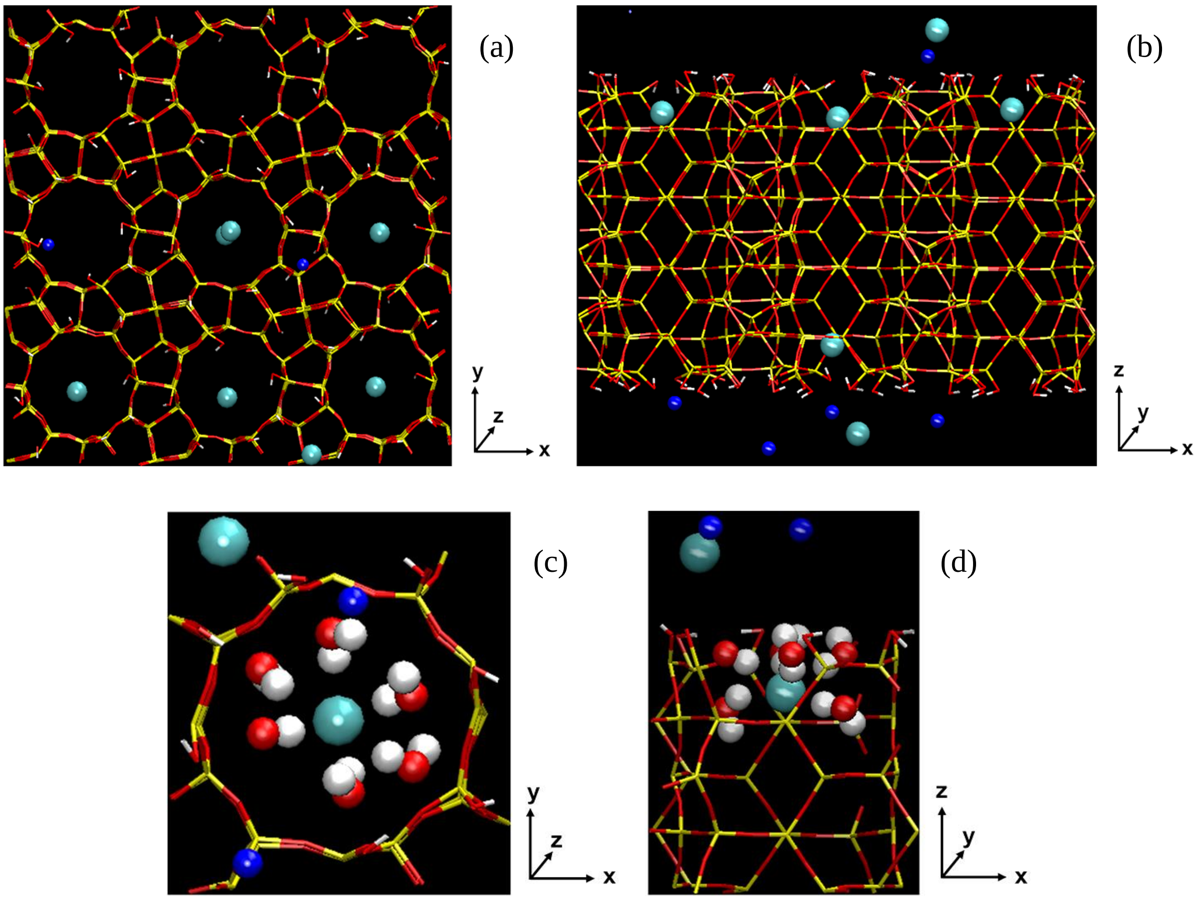

Figure 6-7 Images of molecular configurations: (a) the VET membrane, Na+, and Cl– ions shown from the top view of the plane of the membrane; (b) the side view of the membrane and ions; (c) the zoom-in image of the top view of the membrane pore, ions, and neighbouring water molecules around Cl–; (d) the side view of the same configuration as (c). Water layers are removed in (a) and (b), and the rest of water molecules except the water molecules of interest is removed in (c) and (d) for the clear visualisation. The same representation and colouring methods for each atom are applied as Figure 6-4.

As shown in Figure 6-7, the chloride ions tend to sit on the entrance of the pore along with their neighbouring water molecules. This is a characteristic behaviour happening on the functionalised VET membrane, which is very different from that of the counter ion, Na$^+$.

In the PMF plot in Figure 6-6, the position of the pore channel is the range of -12 Å < z < 12 Å, hence the extra region can be regarded as the range of the bulk water (z < -12 Å and z > 12 Å). As expected, water penetration into the pore is more likely than in the LTA membranes because the maximum energy barrier is 0.17 eV (16.40 kJ mol^{-1}) even though the energy value is much higher than the comparable data (1.67 – 7.50 kJ mol^{-1}) in the literature reported about (7,7), (8,8), and (10,10) CNTs (Corry, 2008, Beu, 2010). This high energy barrier is mainly due to the stabilised Cl$^-$

on the pore since it has to be removed for the water molecule to enter the pore. Also, given that those literature values didn't consider the effect of pore functional groups, our value may be partly explained by the fact that the surface hydroxyl groups can make an additional contribution to the energy barrier. Further study needs to be carried out on this effect. Compared to the LTA membranes studied above, the VET membrane studied here is more favourable for water entering pores due to the wider kinetic pore than those of the LTA membranes.

Another characteristic change in the free energy for the water transport is shown in the middle of the VET channel (-6 Å $< z <$ 6 Å). In this region the PMF is very low, and even becomes slightly negative. This suggests that the water molecule is placed in almost frictionless environment due to the non-polar well-defined cylindrical pore which gives a smoother potential energy surface along the inner wall than the cage-type wall (see discussion made earlier in sections 4.4.1 and 5.4.3). The smooth landscapes are also shown in the CNT studies since CNTs have non-polar smooth cylindrical pores (Beu, 2010, Corry, 2011). This may suggest that our VET membrane has a high water flux once the water overcome the pore entrance barrier if the membrane can effectively block Cl^- ions.

The sodium ion entering the pore faces very high energy barrier of 0.77 eV (74.29 kJ mol^{-1}). The value is a bit lower than the case (86.84 kJ mol^{-1}) in the LTA membrane, but the amount entering can be considered negligible. This means that the transport of the hydrated Na^+ is heavily dependent on the size exclusion effect when the transport takes place at the narrower path than the effective diameter of Na^+. However the free energy drop in the middle of the pore indicates that once the ion has entered the pore, it is likely to stay there.

The PMF results still suggest partial potential for the VET as desalination membrane in term of the low free energy for water passage within the pore and the high energy barrier to sodium ion entrance. To deeply understand this behaviour of Cl^- in the pore vicinity and to find the way to effectively reject the ion, further work needs to be carried out to investigate the effect of various NaCl concentrations and surface functional groups on the behavioural properties on the chloride ion since the water molecules hydrating the Cl^- are less ordered and more affected by the environment (Mancinelli et al., 2007). Moreover, the same system with larger MD simulation cells also needs to be studied since the simulation system size would affect these results as the larger number of repeating units could result in more statistically-reliable data and the larger/longer system could produce a different energy landscape compared to its smaller/shorter counterpart, especially for heterogeneous systems.

6.4 Conclusions

In this chapter, we employed the potential of mean force approach to investigate the free energy changes and energy barriers for transport of water, sodium ion, and chloride ion through the expected pathway of a pressure-driven membrane system.

LTA and VET types of zeolite were selected as potential membrane materials, and they were tested for the identification of the most likely surface facets. LTA had three possible surfaces with the highest stability identified by the static lattice energy minimisation method: *s4r*, *d4r*-e, and *d4r*-f surfaces. However, VET had only one most stable surface as we avoided the unstable two-uncoordinated silicon atoms which may be geminally coordinated by hydroxyl groups.

To construct a membrane system, only *s4r* and *d4r*-e surfaces were chosen as the LTA membrane surfaces because the surface geometries of these two types are very different, while the surface of the VET membrane was built with a single OH coordinated to the singly-unsaturated Si atoms.

The PMF profiles of the passage of water, Na^+, and Cl^- through LTA suggested it had potential for use as a desalination membrane as it had a lower energy barrier to water transport than to ion transport. Two surface morphologies of LTA membrane provided different levels of thermodynamic stability for water molecules and ions in vicinity of the pore surface. Hence, slightly different energy barriers were generated, however in general similar trends in the free energy appeared in both types. The chloride ion was energetically more stable in just outside pores of LTA. This is believed that the surface hydroxyl groups made the ion stable by replacing its solvating water molecules, then coordinating the ion and that the presence of the chloride ion would have increased the barrier for entrance of the water on average. This means that on pores that did not have a chloride ion at the entrance, passage of water would be expected to be easier. This hypothesis deserves study in future work.

The VET membrane showed the lower energy barriers to water and Na^+ entrance compared to either of the LTA membranes. This would seem to provide promise for higher water flux, however the chloride ion is tightly held at the pore entrance and therefore would tend to block the passage of water more in this case than it does in LTA. The energy barrier to Na^+ transport into the pore seems high enough even though it is lower than those of the LTA membranes. The chloride ion was unusually stable when it stayed around the pore, and the barrier to entrance to the pore was lower than the barrier for its remove from the pore entrance to the bulk. This seems to be attributed to the combination effect of the surface hydroxyl groups and the VET pore size which seems to be large enough to accommodate the hydrated Cl^-.

To obtain more intuitive data for permeability of each particle of interest, the permeability test must be carried out under pressure gradient in order to evaluate the flux performance. We have left this topic as our room for future work.

References

ALLEN, M. P. & TILDESLEY, D. J. 1987. *Computer Simulation of Liquids,* New York, Oxford University Press, Oxford.

ARFKEN, G. B., WEBER, H. J. & HARRIS, F. E. 2013. Chapter 23 - Probability and Statistics. *Mathematical Methods for Physicists.* 7th ed. Boston: Academic Press.

BARAM, P. S. & PARKER, S. C. 1996. Atomistic simulation of hydroxide ions in inorganic solids. *Philosophical Magazine Part B,* 73**,** 49-58.

BEU, T. A. 2010. Molecular dynamics simulations of ion transport through carbon nanotubes. I. Influence of geometry, ion specificity, and many-body interactions. *Journal of Chemical Physics,* 132.

CHIPOT, C. & POHORILLE, A. 2007. Calculating Free Energy Differences Using Perturbation Theory. *In:* CHIPOT, C. & POHORILLE, A. (eds.) *Free Energy Calculations.* Springer Berlin Heidelberg.

CORRY, B. 2008. Designing carbon nanotube membranes for efficient water desalination. *Journal of Physical Chemistry B,* 112**,** 1427-1434.

CORRY, B. 2011. Water and ion transport through functionalised carbon nanotubes: implications for desalination technology. *Energy & Environmental Science,* 4**,** 751-759.

CRUZ-CHU, E. R., AKSIMENTIEV, A. & SCHULTEN, K. 2006. Water−Silica Force Field for Simulating Nanodevices. *The Journal of Physical Chemistry B,* 110**,** 21497-21508.

DE LARA, L. S., RIGO, V. A., MICHELON, M. F., METIN, C. O., NGUYEN, Q. P. & MIRANDA, C. R. 2015. Molecular dynamics studies of aqueous silica nanoparticle dispersions: salt effects on the double layer formation. *Journal of Physics: Condensed Matter,* 27**,** 325101.

GREŃ, W., PARKER, S. C., SLATER, B. & LEWIS, D. W. 2010. Structure of Zeolite A (LTA) Surfaces and the Zeolite A/Water Interface. *The Journal of Physical Chemistry C,* 114**,** 9739-9747.

HERMANS, J. & LENTZ, B. 2014. Appendix D - Methods to compute a potential of mean force. *Equilibria and Kinetics of Biological Macromolecules.* 1st ed.: Wiley & Sons, Inc. John.

HOCKNEY, R. W. & EASTWOOD, J. W. 1988. Particle-Particle-Particle-Mesh (P3M) Algorithms. *Computer simulation using particles.* CRC Press.

HUGHES, Z. E., CARRINGTON, L. A., RAITERI, P. & GALE, J. D. 2011. A Computational Investigation into the Suitability of Purely Siliceous Zeolites as Reverse Osmosis Membranes. *The Journal of Physical Chemistry C,* 115**,** 4063-4075.

HUMMER, G., PRATT, L. R. & GARCÍA, A. E. 1996. Free energy of ionic hydration. *The Journal of Physical Chemistry,* 100**,** 1206-1215.

JOUNG, I. S. & CHEATHAM, T. E. 2008. Determination of alkali and halide monovalent ion parameters for use in explicitly solvated biomolecular simulations. *Journal of Physical Chemistry B,* 112**,** 9020-9041.

JOUNG, I. S. & CHEATHAM, T. E. 2009. Molecular Dynamics Simulations of the Dynamic and Energetic Properties of Alkali and Halide Ions Using Water-Model-Specific Ion Parameters. *Journal of Physical Chemistry B,* 113**,** 13279-13290.

KUMAKIRI, I., TSURU, T., NAKAO, S.-I. & KIMURA, S. 2000. Reverse osmosis performance at high pressure with high water recovery. *Journal of Chemical Engineering of Japan,* 33**,** 414-419.

LI, L. X., DONG, J. H., NENOFF, T. M. & LEE, R. 2004. Desalination by reverse osmosis using MFI zeolite membranes. *Journal of Membrane Science,* 243**,** 401-404.

MAKIMURA, D., METIN, C., KABASHIMA, T., MATSUOKA, T., NGUYEN, Q. P. & MIRANDA, C. R. 2010. Combined modeling and experimental studies of hydroxylated silica nanoparticles. *Journal of Materials Science,* 45**,** 5084-5088.

MANCINELLI, R., BOTTI, A., BRUNI, F., RICCI, M. A. & SOPER, A. K. 2007. Hydration of sodium, potassium, and chloride ions in solution and the concept of structure maker/breaker. *The Journal of Physical Chemistry B,* 111**,** 13570-13577.

MARTYNA, G. J., TOBIAS, D. J. & KLEIN, M. L. 1994. Constant pressure molecular dynamics algorithms. *The Journal of Chemical Physics,* 101**,** 4177-4189.

RAI, B. 2012. *Molecular modeling for the design of novel performance chemicals and materials*, CRC Press.

RICHARDS, L. A., SCHAEFER, A. I., RICHARDS, B. S. & CORRY, B. 2012a. The Importance of Dehydration in Determining Ion Transport in Narrow Pores. *Small,* 8**,** 1701-1709.

RICHARDS, L. A., SCHAEFER, A. I., RICHARDS, B. S. & CORRY, B. 2012b. Quantifying barriers to monovalent anion transport in narrow non-polar pores. *Physical Chemistry Chemical Physics,* 14**,** 11633-11638.

ROUX, B. 1995. The calculation of the potential of mean force using computer simulations. *Computer Physics Communications,* 91**,** 275-282.

SANDERS, M. J., LESLIE, M. & CATLOW, C. R. A. 1984. Interatomic potentials for SiO2. *Journal of the Chemical Society, Chemical Communications***,** 1271-1273.

SAUL, P., CATLOW, C. R. A. & KENDRICK, J. 1985. Theoretical studies of protons in sodium hydroxide. *Philosophical Magazine Part B,* 51**,** 107-117.

SHINODA, W., SHIGA, M. & MIKAMI, M. 2004. Rapid estimation of elastic constants by molecular dynamics simulation under constant stress. *Physical Review B,* 69**,** 134103.

SUGIYAMA, S., YAMAMOTO, S., MATSUOKA, O., NOZOYE, H., YU, J., ZHU, G., QIU, S. & TERASAKI, O. 1999. AFM observation of double 4-rings on zeolite LTA crystals surface. *Microporous and Mesoporous Materials,* 28**,** 1-7.

TASKER, P. W. 1979. The surface energies, surface tensions and surface structure of the alkali halide crystals. *Philosophical Magazine A,* 39**,** 119-136.

WAKIHARA, T., SASAKI, Y., KATO, H., IKUHARA, Y. & OKUBO, T. 2005. Investigation of the surface structure of zeolite A. *Physical Chemistry Chemical Physics,* 7**,** 3416-3418.

ZHANG, Y. & XU, Z. 1995. Atomic radii of noble gas elements in condensed phases. *American Mineralogist,* 80**,** 670-675.

Chapter 7 Conclusions and Future Directions

7.1 Conclusions

In this thesis, we mainly considered dynamical and structural properties of water in various geometries of nanoporous zeolites. In addition, the feasibility of using some of the zeolite types as desalination membranes was evaluated. To achieve understanding to these issues, we employed molecular dynamics (MD) simulations that enabled us to closely look at the behaviour and stability of the molecular system, which is difficult to be achieved using macroscopic-scale experiments.

To study the transport properties of the fluid in the nanopores, self-diffusion coefficients were measured for the water since computing the diffusivity can provide data to assist in understanding the molecular mobility of the fluid. Furthermore, collective diffusion coefficients were calculated. It was found that the fluid molecules formed clusters and moved collectively in the pores as also reported in some other literature (Iiyama et al., 2006, Ohba and Kaneko, 2009, Demontis et al., 2008). The collective diffusivity results provide a bridge between the molecular scale motion and the macroscopic water flux since the value can be used to determine flux if the system has a concentration gradient.

In our preliminary MD simulations, we tested which force fields, algorithms, and simulation system sizes are most appropriate. This is crucial to ensure that the results obtained are meaningful and use of inappropriate parameters may sometimes affect the flow of molecules critically (Bernardi et al., 2010, Krishnan et al., 2013, Thomas and Corry, 2014). Thus, to obtain reliable data for the behavioural properties of water, we tested our molecular systems by validating the force field we selected with various algorithms integrating the equations of motion (see theories in sections 3.1 and 4.3.2) and sizes of simulations cell.

The zeolite model we used for this validation work were all silica VET-type zeolites which contain one-dimensional (1-D) cylindrical pores. These zeolites were selected due to our expectation that the non-polar 1-D cylindrical pores may have a relatively low friction in the inner pores as shown in even more extreme cases in studies on carbon nanotubes which reported ultrafast water transport due to their smooth and non-polar inner walls (Holt et al., 2006, Wang et al., 2013). Self-diffusion coefficients were measured for water molecules in the VET framework with two different water loading densities (6 or 32 molecules/pore), showing a good agreement with those of the study (Hughes et al., 2011) which adopted the same force field originally developed and established for silica-water interaction (Sanders et al., 1984). Interestingly, our results could be reproduced using six different thermodynamic ensembles: NVE; NVT; NVT-w (thermostatting to water only); NVT-z (thermostatting to zeolite only); NPH; NPT, showing consistent results to each other as well as the published study in the NPT ensemble. Hence, it was found that our system built with the force field is insensitive to the way in which the system is thermostatted and/or barostatted. Another interesting finding of our study was that the water molecules at the low density in the VET form water clusters. We measured the collective diffusivity by evaluating the centre-of-mass motion of the water clusters in each pore, and the results suggested that the individual water molecule in the cluster also diffuse collectively like the cluster because the collective diffusion coefficient per molecule showed a similar value to the self-diffusion counterpart at the low loading.

For the high water loading density, we found that the water in the VET had a self-diffusion coefficient that was similar to the bulk value suggesting that the flow was bulk-like, although the water density was two-time higher than that of bulk water. This may indicate that fast water transport takes place through the VET pore even when the pore is filled full of water. The per-molecule collective diffusivity was also measured at the high loading, which gave a rate that was 4 times lower than its self-diffusion coefficient unlike the lower loading case. This indicates that the movement of the single water molecule in the pore is not like the averaged motion of the fluid at the high loading.

The structural properties of water were characterised by the radial distribution function (RDF) which indicates the probability of finding another water molecule at any distance from a reference water molecule. The RDF results supported the water dynamics indicated by the diffusivity calculations, indicating that water molecules were mostly locally distributed around the centred water at the low loading. This implies that water clusters were formed and moved collectively in most of time due to the low water density under the highly-confined pore. At higher loading, the distribution becomes more uniform, like in bulk water except the higher probability around the reference water was higher due to the nano-confinement.

Although the values we obtained for the water self-diffusivity were similar to those observed in previous work for both the high and low loading cases, for the low water loading there are some deviations from the mean value obtained from both of our work and the previous work. We believed this was due to the effect of the size of the simulation cell we used. Thus, we extended the VET pore channel by 2-, 3-, and 4-times while keeping the water density constant, and found that the value was converging to an about 2-times lower rate than the original value, and confirming that both our original results and the published results had not converged to the large system limit. In addition, the collective diffusivity per molecule was no longer the same as the self-diffusivity in the extended pore. Nevertheless, the self-diffusivity of water in this pore was over one higher order of magnitude rate than those of the conventional polyamide desalination membranes (Hughes and Gale, 2012, Ding et al., 2014).

At our second phase of study, we broadened our selection of zeolites. Zeolites with three-dimensional pore structures were adopted first for investigation. They were MFI-, LTA-, and FAU-type zeolites. All of them have been extensively studied as catalysts, ion exchangers, absorbents, and desalination membranes. However, only little work has been carried out to obtain a molecular insight into water dynamics and ion selectivity in these materials for application to membranes except the MFI zeolite. Due to many experimental and theoretical data available for MFI, we studied this for our validation work on the stability of the zeolite framework, diffusion coefficients and structural properties of water in the framework.

The self-diffusion coefficients, obtained for the MFI with the force field used in our first study, were comparable to those of the literatures in terms of both the 3-D averaged value and the value of each dimensional component. Also, the structure of water in the framework showed good agreement with those in the literature.

To compare water diffusivities of MFI with those of the other types, a simulation cell with 12 unit cells in each direction was considered so that we could be confident that the size of the cell did not affect the behaviour of the water. Then, the water loading density was adjusted to be the same density used before for the VET. Two other 3-D zeolite frameworks were set up to be sufficiently large, then the same water density was loaded. Water in MFI was found to have a higher self-diffusivity than water in LTA and FAU which seems to be associated with the fact that MFI has straight cylindrical pores perpendicular to zigzag cylindrical pores, while the latter ones both have spherical-like cages where water molecules can be trapped. However, the water diffusivity in FAU was double that of water in LTA, which seems to be attributed to the larger pore openings between the cages in FAU than those in LTA even though the size of the cages in FAU and LTA are fairly similar to each other.

Considering the RDF results, the structure of water in LTA and FAU indicated the existence of the first and second hydration shells more clearly than in MFI due to the existence of the cages in LTA and FAU which were sufficiently large to hold clusters of molecules.

As well as the VET framework, two more zeolites with 1-D cylindrical pores were investigated because the 1-D cylindrical pores led to fast water transport. The TON-type zeolite has slightly elliptical pores with similar diameter to that of VET, and the CFI-type has well-defined cylindrical pores with 1.2-times larger diameter than those of VET.

These 1-D pore zeolites had components of the self-diffusion coefficients in the direction of the pore up to 18-times higher than the largest components of the self-diffusion coefficients obtained for the 3-D pore zeolites. One interesting finding was that the CFI, the largest 1-D pore studied, showed a comparable diffusion coefficient to that of 3-D averaged global diffusion of the MFI. This means that the mobility of the individual water molecule is similar in CFI and MFI, which may be due to the larger number of water molecules fitting in a cluster in CFI than in MFI. Hence, the individual mobility may be more influenced by the water-water interaction than the water-zeolite interaction. But, the collective diffusion coefficient in the direction along the pore for CFI was around 3-times higher than the collective diffusion in the direction of the fastest diffusion for MFI. Even the global collective diffusion coefficient (i.e. averaged over the three directions) was still larger in CFI than in MFI. This indicates that the mobility of the whole cluster in CFI is still higher than that in MFI, which seems to arise from the fact that the well-defined pathway and a relatively smooth potential energy surface along the pore enhance the dynamics of the cluster.

The structure of water in 1-D pore zeolites varied in the size and shape of pores. VET with about 6 Å-diameter cylinders had more four-coordinate molecules in the pore than the elliptical pore in TON. The largest pore, which were considered in CFI, had water structures more like typical bulk water.

From this study, an understanding of water behaviour in nanopores was obtained. It was found that the shape and dimensionality of pores significantly influence the dynamics of water in the pores and the 1-D cylindrical channels had the largest diffusion coefficients along the pores. Further evidence to prove this finding is that the cylindrical channels in MFI had the highest self-diffusivity and collective diffusivity of the 3-D pore zeolites. These indicates that the zeolites with 1-D cylindrical pores may be promising as high flux membranes, if manufacturing methods can be developed to produce large membranes with those cylindrical pores parallel to the water flow.

These studies of diffusional and structural properties of water in various zeolite frameworks gave a deep insight into the effects of the water loading density, pore size and dimensionality on the water behaviour. However, from a practical viewpoint, it is important to consider the effects of the pore entrance and its functional groups on water/ion transport, since it is necessary to determine if these molecules and ions are likely to enter the pores from the bulk solution.

Among the 1-D and 3-D pore zeolites we studied, LTA and VET zeolites were selected as potential membrane materials for further study regarding pore entrance effects. LTA has 3-D pore structures with characteristic cages, but have the narrow pore openings, while VET has well-defined 1-D cylindrical pores, and showed great potential in terms of water flux. The *s4r* and *d4r*-e surfaces were chosen to be the LTA membrane surfaces because the surface geometries of these two types are very different but both are thermodynamical stable, the most stable surface of the VET membrane was built. In all cases a single OH was coordinated to the singly-unsaturated Si atoms formed from cleaving the material.

We employed PMF calculations to measure the thermodynamical stability of the continuous state when the molecule or ion passes through the membrane. The PMF profiles of the passage of water, Na^+, and Cl^- through LTA suggested it had potential for use as a desalination membrane as it had a lower energy barrier to water transport than to ion transport. Two LTA surface morphologies provided different levels of thermodynamic stability for water molecules and ions in vicinity of the pore surface. Hence, slightly different energy barriers were generated, however in general similar trends in the free energy appeared in both types. This indicates that the pore size plays the more key role than the pore morphology in terms of the entrance barrier in this case.

Some interesting findings of this measurement is that Cl^- was energetically more stable when it was situated just outside pores of LTA even though the large energy barrier was generated when it penetrated the pore. It is believed that the surface hydroxyl groups made the ion stable by replacing its solvating water molecules, then coordinating the ion. Hence, this behaviour may affect the water passage, the energy barrier of water transport may be overestimated compared to no Cl^- on the pore. This effect will be more discussed in our future work.

The VET membrane showed the lower energy barriers to water and Na^+ entrance compared to either of the LTA membranes. This may be a promising aspect for higher water flux, however the chloride ion was unusually stable and was tightly held at the pore entrance. Therefore, it could block the passage of water more than it did in LTA. This may be due to the combination effect of the surface hydroxyl groups and the VET pore size which seems to be large enough to accommodate the hydrated Cl^-. The energy barrier to Na^+ transport into the pore was high enough even though it was lower than those of the LTA membranes.

To extend our study in future, relationships between the stability of the chloride ion and the membrane pore size or the surface functional group must be addressed. Also, to obtain more intuitive data for permeability of each particle of interest, the pressure-driven permeability test should be done to evaluate the membrane flux performance.

7.2 Future Directions

As noted earlier, MD results obtained from various simulation cell sizes may differ, especially the time-evolution of the systems and the probability density. In the case of the LTA membrane, the membrane consists of β-cages and *d4r*-rings which are bridges between the β-cages. Thus, if we use the LTA membrane with long pore channels (LTA membrane extended in the direction of the channel), the effect of the change of the inner pore geometry on particle transport will be evaluated. This implies that the effect of inner pore walls on the particle transport as well as the effect of pore entrance can be clearly shown. Therefore, our zeolite membrane systems can be extended for the free energy calculations by extending the water layers and/or the zeolite membrane channels.

The pore size and surface functional groups, –OH groups, may significantly affect the stability of ion entrance to the pore as shown in our free energy study. To clarify these effects, zeolite membranes with 1-D cylindrical pores with the narrower size (e.g. TON-type) can be investigated, and/or studies of zeolite membrane surfaces with various functional groups (e.g. –COOH, –NH_2) would be of particular research interest since these functional groups as well as –OH groups have been experimentally shown to functionalise the silica surface through chemical modifications (Cash et al., 2012, de Oliveira et al., 2016). By modifying the surface groups, the effect of different surface chemistries on the free energy change for transport of each particle can be studied.

To obtain more practical results for the membrane performance, water and ion flux must be measured under a pressure gradient which mimics the real RO system. In MD simulations, the pressure gradient can be made using various approaches, such as use of movable atomic pistons or applying forces to part of water layers (Liu and Chen, 2013, Thomas and Corry, 2016, Heiranian et al., 2015).

$AlPO_4$-5 is one of aluminophosphate zeolites and AFI-type which has well-defined 1-D cylindrical pores (Bordat et al., 2007, Coulomb et al., 2013). The pure silica of the same type also exists and is called SSZ-24 (Demontis et al., 2012). Hence, our study may extend to different chemical components on the same framework geometry as the silica. By studying water diffusional and structural properties, and free energy change of each transport through those as well as water/ion fluxes, we will be able to gain some understanding to the effect of different chemistries of zeolites on water behaviour and membrane performance. All of these comprehensive studies are expected to broaden the area of zeolite materials as desalination membranes.

References

BERNARDI, S., TODD, B. D. & SEARLES, D. J. 2010. Thermostating highly confined fluids. *The Journal of Chemical Physics,* 132, 244706.

BORDAT, P., KIRSTEIN, J., LABEGUERIE, P., MERAWA, M. & BROWN, R. 2007. Structure and dynamics of AlPO4-5 and other aluminophosphates: Classical molecular dynamics and ab initio calculations. *Journal of Physical Chemistry C,* 111, 10972-10981.

CASH, B. M., WANG, L. & BENICEWICZ, B. C. 2012. The preparation and characterization of carboxylic acid-coated silica nanoparticles. *Journal of Polymer Science Part A: Polymer Chemistry,* 50, 2533-2540.

CORRY, B. 2008. Designing carbon nanotube membranes for efficient water desalination. *Journal of Physical Chemistry B*, 112, 1427-1434.

COULOMB, J.-P., FLOQUET, N., MARTIN, C. & ANDRÉ, G. 2013. Structural and dynamics properties of methane confined phase in AlPO4-5 model aluminophosphate: An illustrative example of quasi-(1D) phase transition. *Microporous and Mesoporous Materials,* 171, 82-86.

DE OLIVEIRA, L. F., BOUCHMELLA, K., GONÇALVES, K. D. A., BETTINI, J., KOBARG, J. & CARDOSO, M. B. 2016. Functionalized Silica Nanoparticles As an Alternative Platform for Targeted Drug-Delivery of Water Insoluble Drugs. *Langmuir,* 32, 3217-3225.

DEMONTIS, P., GULÍN-GONZÁLEZ, J., JOBIC, H., MASIA, M., SALE, R. & SUFFRITTI, G. B. 2008. Dynamical Properties of Confined Water Nanoclusters: Simulation Study of Hydrated Zeolite NaA: Structural and Vibrational Properties. *ACS Nano,* 2, 1603-1614.

DEMONTIS, P., GULÍN-GONZÁLEZ, J. & SUFFRITTI, G. B. 2012. Water Adsorbed in AlPO$_4$-5 and SSZ-24 Studied by Molecular Dynamics Simulation. *The Journal of Physical Chemistry C,* 116, 11100-11109.

DING, M., GHOUFI, A. & SZYMCZYK, A. 2014. Molecular simulations of polyamide reverse osmosis membranes. *Desalination,* 343, 48-53.

HEIRANIAN, M., FARIMANI, A. B. & ALURU, N. R. 2015. Water desalination with a single-layer MoS2 nanopore. *Nature Communications,* 6, 8616.

HOLT, J. K., PARK, H. G., WANG, Y. M., STADERMANN, M., ARTYUKHIN, A. B., GRIGOROPOULOS, C. P., NOY, A. & BAKAJIN, O. 2006. Fast mass transport through sub-2-nanometer carbon nanotubes. *Science,* 312, 1034-1037.

HUGHES, Z. E., CARRINGTON, L. A., RAITERI, P. & GALE, J. D. 2011. A Computational Investigation into the Suitability of Purely Siliceous Zeolites as Reverse Osmosis Membranes. *The Journal of Physical Chemistry C,* 115**,** 4063-4075.

HUGHES, Z. E. & GALE, J. D. 2012. Molecular dynamics simulations of the interactions of potential foulant molecules and a reverse osmosis membrane. *Journal of Materials Chemistry,* 22**,** 175-184.

IIYAMA, T., ARAGAKI, R., URUSHIBARA, T. & OZEKI, S. 2006. Direct Determination of the Intermolecular Structure of the Adsorbed Phase Using *in situ* X-Ray Diffraction and Reverse Monte Carlo Methods. *Adsorption Science & Technology,* 24**,** 815-821.

KRISHNAN, T. V. S., BABU, J. S. & SATHIAN, S. P. 2013. A molecular dynamics study on the effect of thermostat selection on the physical behavior of water molecules inside single walled carbon nanotubes. *Journal of Molecular Liquids,* 188**,** 42-48.

LIU, Y. & CHEN, X. 2013. High permeability and salt rejection reverse osmosis by a zeolite nano-membrane. *Physical Chemistry Chemical Physics,* 15**,** 6817-6824.

OHBA, T. & KANEKO, K. 2009. Initial filling mechanism of predominant water adsorption on hydrophobic slit-shaped carbon nanopores. *Journal of Physics: Conference Series,* 177**,** 012001.

SANDERS, M. J., LESLIE, M. & CATLOW, C. R. A. 1984. Interatomic potentials for SiO2. *Journal of the Chemical Society, Chemical Communications***,** 1271-1273.

THOMAS, M. & CORRY, B. 2014. Thermostat choice significantly influences water flow rates in molecular dynamics studies of carbon nanotubes. *Microfluidics and Nanofluidics***,** 1-7.

THOMAS, M. & CORRY, B. 2016. A computational assessment of the permeability and salt rejection of carbon nanotube membranes and their application to water desalination. *Philosophical Transactions of the Royal Society A: Mathematical, Physical and Engineering Sciences,* 374.

WANG, L., DUMONT, R. S. & DICKSON, J. M. 2013. Nonequilibrium molecular dynamics simulation of pressure-driven water transport through modified CNT membranes. *Journal of Chemical Physics,* 138**,** 124701.